Title

Clinical Translation of Dynamic Optical Contrast Imaging for Label-Free Tissue Identification and Surgical Navigation in Head and Neck Oncology

Author

Pellionisz, Peter

Publication Date

2020

Peer reviewed|Thesis/dissertation

UNIVERSITY OF CALIFORNIA

Los Angeles

Clinical Translation of Dynamic Optical Contrast Imaging for Label-Free Tissue Identification and Surgical Navigation in Head and Neck Oncology

A dissertation submitted in partial satisfaction

of the requirements for the degree

Doctor of Philosophy in Bioengineering

by

Peter Pellionisz

2020

ABSTRACT OF THE DISSERTATION

Clinical Translation of Dynamic Optical Contrast Imaging for Label-Free Tissue Identification and Surgical Navigation in Head and Neck Oncology

by

Peter Pellionisz

Doctor of Philosophy in Biomedical Engineering

University of California, Los Angeles, 2020

Professor Maie A. St. John, Co-Chair

Professor Michael A. Teitell, Co-Chair

There exists a pressing medical need for non-invasive optical tools to help surgeons intraoperatively identify tissue and determine precise tumor margins. The primary curative treatment for Head and Neck Cancer often includes complete surgical resection of the tumor, which may lead to severe loss of function, disfigurement, and poor quality of life for these patients. The goal of this dissertation is to form the foundation for successful clinical translation of Dynamic Optical Contrast Imaging (DOCI) as a label-free technique that can produce contrast from relative measurement of time-resolved tissue autofluorescence. The tool generates contrast through relative measurements of autofluorescence decay (lifetime) from tissue and thus does not require dye or injection of contrast agents. Furthermore, as opposed to intensity based approaches, these

measurements depend on the intrinsic properties of tissue and provide a robust signal insensitive to inhomogeneous illumination and irregular tissue contours.

Results include the first clinical use of DOCI to produce relative lifetime tissue maps at an unprecedented six-by-six cm field of view revealing unique spectral features for individual states of disease before tissue biopsy. Through pilot study, a new clinical application for Mohs micrographic surgery is presented. Clinical obstacles were addressed and a new system was tested with ex vivo specimens and validated with histopathology. An improved method for imaging is presented enabling up to a 40% increase in signal-to-noise and a 100% increase in system dynamic range. In addition, a method and system is presented for spectral control of intraoperative illumination that may circumvent the need to turn off the lights during optical imaging. Finally, system measurements were validated and standardized with two-photon microscopy and reference dye for future multi-site clinical trial.

Although currently DOCI values are only an approximation to the complex nature of heterogenous fluorescence lifetime decay, the method permits generation of meaningful contrast between neoplastic and surrounding normal tissue that may aid clinicians and lead to improved patient outcomes. The results regarding clinical performance of Dynamic Optical Contrast Imaging should be considered as preliminary and not be used for medical diagnosis or treatment before appropriate regulatory and medical approval.

The dissertation of Peter Pellionisz is approved.

Erik P. Dutson

Oscar M. Stafsudd

Dino Di Carlo

Maie A. St. John, Committee Co-Chair

Michael A. Teitell, Committee Co-Chair

University of California, Los Angeles

2020

This dissertation is dedicated to the first teacher I ever had, my grandmother.

TABLE OF CONTENTS

LIST OF FIGURES

LIST OF TABLES

LIST OF ACRONYMS

AF	Autofluorescence
BCC	Basal Cell Carcinoma
CASIT	Center for Advanced Surgical and Interventional Technology
CT	Computed Tomography
DOCI	Dynamic Optical Contrast Imaging
DSLR	Digital Single Reflex Lens
FOV	Field Of View
H&E	Hematoxilin and Eosin
HFUS	High-Frequency Ultrasound
HNSCC	Head And Neck Squamous Cell Carcinoma
iCCD	Intensified Charge Coupled Device
LED	Light Emitting Diode
MM	Malignant Melanoma
MRI	Magnetic Resonance Imaging
OCT	Optical Coherence Tomography
OSCC	Oral Squamous Cell Carcinoma
PAT	Photoacoustic Tomography
PET	Positron Emission Tomography
RLD	Rapid Lifetime Determination
ROI	Region Of Interest
SCC	Squamous Cell Carcinoma
SNR	Signal To Noise Ratio
US	Ultrasound

ACKNOWLEDGEMENTS

Thank you Mom for both personally and professionally guiding me along my path to become a physician-scientist. Thank you for blessing me with so many gifts, for serving as my role model, and for reminding me each day how I can influence the lives of others for the better. This PhD is as much your achievement as mine.

Thank you Dad for granting me a love for physics and machines. I am thankful to have had the opportunity to further develop these skills that you provided me at an early age.

I would like to thank Dr. Warren Grundfest for granting me the opportunity to be a part of this research. While he is no longer with us, his drive to innovate and develop new medical devices will continue through his students.

Thank you Dr. Maie St. John for not only mentoring me in both Head and Neck Surgery and Bioengineering, but also for serving as a substitute mother in times of need. From a surgical mission trip to Guatemala, presenting at the Head and Neck Surgery conference in New Orleans, to attending the first international conference on parathyroid imaging in Geneva, staying by your side has taken me around the world.

Thank you Dr. Oscar Stafsudd for rejoining the lab and saving me from failure. I am so grateful to you for your help.

Thank you Dr. Erik Dutson for showing me that surgeons know how to have a good time. Your leadership, humor, and personality have always made my days brighter and more exciting.

Thank you Dr. Michael Teitell for working all day and night in your role as the chair of the Comprehensive Cancer Center yet still making time to serve on my committee. I am very thankful to have the opportunity to learn from the very best in the field, both from your teaching and by the example show.

Thank you Dr. Dino Di Carlo for supporting my work and progress in the MD-PhD program.

Thank you Dr. Carlos Portera for granting me the opportunity develop two-photon microscopes in your lab, and for showing me that there is no better place to be than the UCLA MSTP program. I am incredibly grateful for your guidance, mentorship, and kind help throughout my journey in this program.

Thank you Dr. Katsushi Arisaka, for opening my eyes to the wonderful world of microscopy. I am very grateful to learn from a world-expert like yourself.

Thank you Maani Archang and Anya Afasizheva for your valuable friendship and support, as well as to just about the entire student body of the medical scientist program:)

I would like to thank all current members of Dr. St. John's lab (Dr. Yong Hu, Dr. Yazeed and Shan Huang) for the constructive talks, ideas, help of all sorts, mentorship, guidance, and collaboration across all projects, designs, manuscripts, presentations, and publications. Peter Yu helped develop the LED driving circuit. Yong Hu helped develop, construct, and improve the improved DOCI system with the liquid light cable, the GUI, the dye experiment for standardizing the system. Shan Huang helped a great deal with Matlab when I did not know the best way forward. Shijun Sung and Ameet Braganza contributed to the design and construction of a prototype 4D endoscope mount. Thank you Neha Bajwa and Karam Badran for your help in reviewing Image Guidance in Otolaryngology for an upcoming textbook chapter, and your comments, suggestions, and input into my background chapter. Parts of Chapter 2 are modified and adapted from the published and in press book chapters referenced below.

Pellionisz PA, Levy S, Liang J, Namiri N, Cheng H, Hu Y, Badran K, Messadi D, Taylor Z, St. John M, Grundfest W. Emerging Technology for Screening of Oral Cancer. In: "Translational Research: Recent Progress and Future Directions", Ed. By Chiappelli. Nova. 2018. ISBN: 978-1-53614-598-4

Bajwa N, Pellionisz PA, Badran K, Grundfest W, St. John M. Optical Image-Guided Surgery in Otolaryngology. In: "Image-Guided Therapy, Surgery, and Drug Delivery: From Benchtop to Clinic", Ed. By Keyvan & Liapi. Taylor & Francis Group. 2018. (In Press)

Individual experiments and partial results from Chapters 4, 5, and 6 have been published in the following publications:

Pellionisz PA, Badran KW, Grundfest WS, St John MA. Detection of surgical margins in oral cavity cancer: the role of dynamic optical contrast imaging. Curr Opin Otolaryngol Head Neck Surg. 2018 Apr;26(2):102-107. PMID: 29517537

Pellionisz P, Badran K, Lin Y, Mallen-St.Claire J, Schaue D, Elashoff DA, et al. A Modular Polymer Platform that Delivers Recombinant Cytokines and Cisplatin Allows for De-Escalation of Radiation Therapy in an Animal Model of Head and Neck Squamous Cell Carcinoma. International Journal of Radiation Oncology*Biology*Physics. 2018 Apr;100(5):1369.

Pellionisz PA, Cheng H, Pantoja JL, Grundfest W, St. John MA, editors. Development of Relative Lifetime Imaging System for Intraoperative Parathyroid Identification. Biophotonics Congress: Optics in the Life Sciences Congress 2019 (BODA,BRAIN,NTM,OMA,OMP); 2019 2019/04/14; Tucson, Arizona: Optical Society of America.

Pellionisz PA, Hu Y, Moon A, Rangwalla K, Pensa J, John MAS, editors. Ratiometric autofluorescence lifetime imaging system standardization and application for head and neck cancer. Optics in Health Care and Biomedical Optics IX; 2019 2019/11/20/: International Society for Optics and Photonics.

Pellionisz PA, Levy S, Liang J, Namiri N, Cheng H, Hu Y, Badran K, Messadi D, Taylor Z, St. John M, Grundfest W. Emerging Technology for Screening of Oral Cancer. In: “Translational Research: Recent Progress and Future Directions”, Ed. By Chiappelli. Nova. 2018. ISBN: 978-1-53614-598-4

Chapters 7 and 8 are modified versions of submitted patents where I am an inventor.

I am very grateful to all past members of the lab that have helped me or worked on this project in any form. Thank you Zach Taylor and Harrison Cheng for your huge work throughout the early development and realization of this project. Thank you, Khuzaima Rungwalla, Nikan Namiri, Greg Suematsu, Jeff Liang, Sabrina Levy, Amanda Miller, Andy Moon, Kera Kwan, Albert Han, Harrison Cheng, Joe Pantoya, Roxana Moayer, Karam Badran, Asael Papour, Adria Sherman, Laith Muhdad, and Jake Pensa. I apologize if I there is anyone I have missed, please be assured that if so, it was by accident and not on purpose.

Two-photon fluorescence lifetime microscopy and analysis was performed at the Advanced Light Microscopy/Spectroscopy Laboratory and the Leica Microsystems Center of Excellence at the California NanoSystems Institute at UCLA with funding support from the NIH Shared Instrumentation Grant S10OD025017 and NSF Major Research Instrumentation grant CHE-0722519.

Funding for the completion of this work was provided by the National Institute of Health (NIH) (1R01CA205051-01A1, 1R01CA220663-01A1); UCLA Medical Scientist Training Program (UCLA-MSTP) (T32-GM008042), and John Bent merit award for development of powered surgical devices from the Department of Bioengineering at the University of California at Los Angeles.

CURRICULUM VITAE

EDUCATION

University of California, Los Angeles, CA **2017 - Present**
Expected Doctorate of Philosophy, Bioengineering
Concentration: Non-Invasive Medical Imaging

David Geffen School of Medicine at University of California, Los Angeles, CA **2015 - Present**
Expected Doctorate of Medicine

University of California, Los Angeles, CA **2014**
Bachelor of Science, Molecular, Cell, and Developmental Biology
Concentration: Bessel Beam and Light Sheet Microscopy for In-Vivo Neural Imaging

EXPERIENCE

Center for Advanced Surgical and Interventional Technologies (CASIT), UCLA, Dept. of Biomedical Engineering and Surgery **June 2016 - Present**
Graduate Student Researcher, PhD Candidate

- Development, prototype, and clinical translation of Dynamic Optical Contrast Imaging as a tool for tissue identification and surgical guidance using relative measurement of autofluorescence lifetime.
- Performed first feasibility studies of Dynamic Optical Contrast Imaging for application in Mohs micrographic surgery.
- Produced first *in vivo* evidence demonstrating feasibility of Dynamic Optical Contrast Imaging as a clinical diagnostic tool for early and accurate detection of squamous cell carcinoma and neoplastic precursor lesions.
- Invented new imaging method for dynamic optical contrast imaging for 40% improvement in signal to noise and double the dynamic range. This work resulted in a provisional patent application in which I am listed as a co-inventor.
- Invented selective spectral emission surgical lighting system. This work resulted in a provisional patent application in which I am listed as a co-inventor.
- Led *in vivo* validation studies of Dynamic Optical Contrast Imaging for HNSCC tumor boundary detection.
- Authored and was awarded NIH funding ($99,116) for an R01 supplemental application to correlate gender specific autofluorescence lifetime differences for both patient screening and surgical resection.
- Co-Authored and was awarded funding ($299,000) for Phase I clinical trial of DOCI.
- Development and pre-clinical testing, and clinical translation of time-multiplexed ultrasound device enabling deep tissue elasticity measurements. Published in Yale Journal of Biology and Medicine.
- Development, prototype, and pre-clinical testing of near-infrared spectroscopy device for early detection of necrotizing enterocolitis in newborns.
- Pre-clinical testing and clinical translation of drug-eluting polymer. Published safe human use of polymer and possible decrease in dose of radiotherapy following tumor resection in Journal of Otolaryngology – Head and Neck Surgery.
- Investigation of superior cervical ganglia mediated cerebral vasospasm post subarachnoid hemorrhage. Performed cadaveric dissection, electrophysiology, and microinjection of retrograde neuronal tracers.

Carlos Portera-Caillau, UCLA, Department of Neurology **Jun 2014 - Jun 2015**
Graduate Research Associate

- Developed and built resonant scanning (8kHz) two-photon microscope for in vivo brain imaging through rodent cranial windows. This system was used to acquire all the data for a subsequent work published in Nature Neuroscience.
- Constructed prototype of frequency multiplexed two-photon fluorescent microscope using acousto-optic deflectors.

Katsushi Arisaka, UCLA, Department of Physics **Jan 2012 - Jun 2014**
Senior Research Associate

- Co-Authored and was awarded $642,000 NSF grant for 3D Bessel Beam Imaging System.
- Developed and constructed Bessel-beam fluorescence microscope for deep (~5cm) tissue imaging.
- Development, construction, and testing of selective plane illumination fluorescence microscope and facility at California Nanosystems Institute, then validated the system through rapid (200Hz) imaging of calcium ion flux in the beating hearts of Zebrafish.

JOURNAL ARTICLES

Pantoja JL, Chang K, **Pellionisz PA**, Woo K, Farley SM. Paneled Saphenous Vein Grafts Compared to Internal Jugular Vein Grafts in Venous Reconstruction after Pancreaticoduodenectomy. Ann Vasc Surg. 2019 Nov 8. S0890-5096(19)30966-5. PMID: 31712190

Dai Y, Abiri A, Pensa J, Liu S, Paydar O, Sohn H, Sun S, **Pellionisz PA**, Pensa C, Dutson EP, Grundfest WS, Candler RN. Biaxial sensing suture breakage warning system for robotic surgery. Biomed Microdevices. 2019 Jan 10;21(1):10. PMID: 30631976

Pellionisz PA, Namiri NK, Suematsu G, Hu Y, Braganza A, Rangwalla K, Denson DJ, Badran K, Francis NC, Maccabi A, Saddik G, Taylor Z, St John MA, Grundfest WS. Vibroacoustographic System for Tumor Identification. Yale J Biol Med. 2018 Sep 21;91(3):215-223. PMID: 30258308

Pellionisz PA, Badran KW, Grundfest WS, St John MA. Detection of surgical margins in oral cavity cancer: the role of dynamic optical contrast imaging. Curr Opin Otolaryngol Head Neck Surg. 2018 Apr;26(2):102-107. PMID: 29517537

Pellionisz PA, Lin Y, Mallen-St Clair J, Luo J, Suwarnasarn A, Schaue D, Elashoff DA, Palma-Diaz F, Dubinett SM, Sharma S, Wu B, St John MA. Use of a Novel Polymer in an Animal Model of Head and Neck Squamous Cell Carcinoma. Otolaryngol Head Neck Surg. 2018 Jan;158(1):110-117. PMID: 28895464

Barkhordarian A, **Pellionisz P**, Dousti M, Lam V, Gleason L, Dousti M, Moura J, Chiappelli F. Assessment of risk of bias in translational science. J Transl Med. 2013 Aug 8;11:184. PMID: 23927081

de Resende MF, Vieira S, Chinen LT, Chiappelli F, da Fonseca FP, Guimarães GC, Soares FA, Neves I, Pagotty S, **Pellionisz PA**, Barkhordarian A, Brant X, Rocha RM. Prognostication of prostate cancer based on TOP2A protein and gene assessment: TOP2A in prostate cancer. J Transl Med. 2013 Feb 11;11:36. PMID: 23398928

CONFERENCE PROCEEDINGS

Badran K, **Pellionisz P**, Han A, Heineman T, Saggi S, Goel AN, Sharma S, Dubinett S, John M. Immunomodulation in Novel Cancer Therapies: The Role of CC-motif Chemokine Ligand 21 and Programmed Cell Death Protein 1. International Journal of Radiation Oncology*Biology*Physics. 2018;100:1371-2

Pellionisz P, Badran K, Lin Y, Mallen-St.Claire J, Schaue D, Elashoff DA, et al. A Modular Polymer Platform that Delivers Recombinant Cytokines and Cisplatin Allows for De-Escalation of Radiation Therapy in an Animal Model of Head and Neck Squamous Cell Carcinoma. International Journal of Radiation Oncology*Biology*Physics. 2018 Apr;100(5):1369.

Pellionisz PA, Cheng H, Pantoja JL, Grundfest W, St. John MA, editors. Development of Relative Lifetime Imaging System for Intraoperative Parathyroid Identification. Biophotonics Congress: Optics in the Life Sciences Congress 2019 (BODA,BRAIN,NTM,OMA,OMP); 2019 2019/04/14; Tucson, Arizona: Optical Society of America.

Pellionisz PA, Hu Y, Moon A, Rangwalla K, Pensa J, John MAS, editors. Ratiometric autofluorescence lifetime imaging system standardization and application for head and neck cancer. Optics in Health Care and Biomedical Optics IX; 2019 2019/11/20/: International Society for Optics and Photonics.

Cheng H, Xie Y, **Pellionisz P**, Pearigen A, Rangwalla K, Stafsudd O, Taylor Z, John MS, Grundfest W, editors. Dynamic optical contrast imaging (DOCI): system theory for rapid, wide-field, multispectral optical imaging using fluorescence lifetime contrast mechanism. Medical Imaging 2019: Image-Guided Procedures, Robotic Interventions, and Modeling; 2019 2019/03/08/: International Society for Optics and Photonics.

BOOK CHAPTERS

Pellionisz PA, Levy S, Liang J, Namiri N, Cheng H, Hu Y, Badran K, Messadi D, Taylor Z, St. John M, Grundfest W. Emerging Technology for Screening of Oral Cancer. In: "Translational Research: Recent Progress and Future Directions", Ed. By Chiappelli. Nova. 2018. ISBN: 978-1-53614-598-4

Bajwa N, **Pellionisz PA**, Badran K, Grundfest W, St. John M. Optical Image-Guided Surgery in Otolaryngology. In: "Image-Guided Therapy, Surgery, and Drug Delivery: From Benchtop to Clinic", Ed. By Keyvan & Liapi. Taylor & Francis Group. 2018. (In Press)

Pellionisz AJ, Graham R, **Pellionisz PA**, Perez JC. Recursive Genome Function Of The Cerebellum: Geometric Unification Of Neuroscience And Genomics. In: "Handbook of the Cerebellum and Cerebellar Disorders". Ed. By Manto, Gruol, Schmahmann, Koibuchi, and Rossi. Springer. 2013; 1381-1423. ISBN- 978-9400713321

CHAPTER 1: **INTRODUCTION**

1.1 Goal

The long-term goal of academic medical research is the clinical translation of scientific discoveries(1). This thesis concerns the clinical translation of dynamic optical contrast imaging method and system for label-free tissue identification and surgical navigation in head and neck oncology.

1.2 Motivation

Improvements in the differentiation between tumor and surrounding normal tissue would represent a considerable advancement towards improving clinical decision making (i.e. biopsy selection), and thus decrease the amount of invasive biopsies performed. Extending into the operating room, surgeons rely on their natural senses of sight and physical touch to localize the contours of a tumor followed by limited frozen section biopsy to establish “clean margins” (2–4). Consequently, the determination of tumor margins by palpation and visual inspection has led to recurrence rates of 25-50% (5,6). These challenges substantiate both a clinical need for improved screening and a related surgical need for intraoperative guidance.

1.3 Aims

Hypothesis: Dynamic optical contrast imaging reveals statistically significant and pathology-specific image contrast, at surgically relevant fields of view, in near real-time, and without dye or exogenous labels ***in vivo***.

Aim 1: Generate evidence of in vivo clinical utility and application of DOCI to produce statistically significant contrast without dye or labels and at surgically relevant field of view.

1.1 Acquire DOCI and visual images of patients (N = 62) undergoing surgery for HNC and oral biopsies in clinic.

1.2 Demarcate and annotate suspect areas identified with DOCI and visual inspection.

1.3 Analyze DOCI images for statistically significant contrast and unique relative lifetime features in ROIs corresponding to histologically distinct tissue regions.

Aim 2: Identify and mitigate clinical obstacles by optimizing system and methods for larger, multi-site clinical trial.

2.1 Identify obstacles to clinical use of the system. then optimize system and method and verify with ex-vivo SCC specimens.

2.2 Validate measurements against both reference fluorescent dye and state-of-the-art multi-million dollar commercial two-photon fluorescent lifetime imaging system.

1.4 Overview Of Chapters

Th material comprising this dissertation have been divided into 9 Chapters with supplementary figures located in Appendix A. CHAPTER 1 presents the motivation and aims. CHAPTER 2 reviews relevant background concerning the medical need, the latest tools for label-free imaging at high resolution, the engineering background for fluorescence and autofluorescence imaging, and the technical basis and clinical applications of fluorescence lifetime imaging. CHAPTER 3 presents the technique of Dynamic Optical Contrast Imaging. CHAPTER 4 details the first clinical trial of the DOCI system. CHAPTER 5, the optimization of the system and testing with ex vivo HNSCC specimens. CHAPTER 6 presents results from validation with ex vivo parathyroid tissue, as well as standardization with both reference dye and a commercial two-photon microscope.

Two new methods improving the imaging technique are described in CHAPTER 7 and CHAPTER 8. Finally, the conclusions and future directions are found in CHAPTER 9. This work was made possible by the collaborative efforts of the departments of Head and Neck Surgery and Bioengineering at the University of California at Los Angeles.

CHAPTER 2: **BACKGROUND**

2.1 Head And Neck Squamous Cell Carcinoma And Radical Resection

2.1.1 Introduction

Surgical resection remains the mainstay of curative treatment for many, if not most, cancers of the head and neck (7,8). A key challenge that continues to burden oncologic surgeons is adequately distinguishing tumor boundaries from adjacent normal tissues, and consequently, obtaining tumor-free margins. Not surprisingly, the key question on most patients' minds is, "how do you know if you have removed it all?" The answer thus far has usually been some form of "we cannot be sure," due to the absence of a test or scan that can reliably confirm negative margins with 100% accuracy. What has been demonstrated with significant certainty is that residual tumor tissue left behind after oncologic surgery (i.e. positive margins) leads to recurrent disease and adversely affects patient prognosis and clinical outcomes (9,10). Negative margins are paramount in order to maximize survival, reduce recurrences, and improve the quality of life for patients undergoing oncologic surgery, Head and neck squamous cell carcinomas (HNSCC) have some of the highest rates of disease recurrence and lowest survival rates of salvage surgery (15-20%). These challenges substantiate both a clinical need for improved screening and a related surgical need for intraoperative guidance (11–13).

2.1.2 Oral Cancer Background

A significant clinical need in head and neck oncology exists regarding effective early diagnosis and treatment of oral cancer. Oral Cancer is the sixth most common cancer worldwide and the prognosis for patients with OSCC is largely determined by the stage of disease at clinical presentation (14–17). Patients diagnosed with advanced OSCC have shorter survival times (5-year mortality, 85%, 75%, 47%, and 35% among patients diagnosed as having distant, regional,

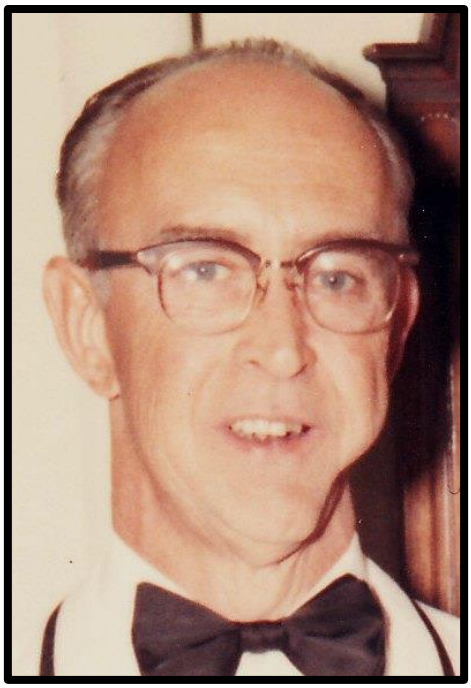

Figure 2-1: Head and neck cancers can distort the face and affect basic abilities to eat, drink, and swallow.
John Bent; An engineer and inventor, had half of his left mandible surgically removed due to complications associated with radiation therapy for OSCC. The other half of his mandible was removed soon afterwards. Today, a scholarship exists in his name at the Department of Biomedical Engineering at UCLA for the development of powered surgical instruments. Permission granted from the Bent family.

local, and *in situ* cancer, respectively) and are more expensive to treat, with the average cost for treating an advanced oral cancer often exceeding $200,000 (18–20). Importantly, the primary management of OSCC relies on the complete surgical resection of the tumor and these surgeries often lead to severe loss of function, disfigurement, and poor quality of life (Figure 2-1). Despite medical advances in the management of OSCC, the global incidence, morbidity, and mortality associated with this disease remain relatively unchanged in the past three decades (20–23). One of the major factors accounting for these dismal reports is that over 60% of OSCC cases are detected at a late stage (III or IV), when diagnostic evaluation, treatment, and management of complications and recurrences are often lengthy, complex, and burdened by poor outcomes (22–

24). The primary prevention of the disease involves reducing exposure to tobacco, alcohol, betel nuts, and likely protecting against HPV infection through immunization (25–27).

2.1.3 Aim Of Screening And Treatment

Screening is a secondary prevention with the aim of early detection when the disease is more amenable to treatment. The prognostic implications of diagnosis and treatment of early intra-epithelial stages of OSCC carcinogenesis have already shown to be highly significant due to the high survival rates (~80%) of patients diagnosed with early stage OSCC (28). Thus, the early screening of oral lesions and identification of pre-cancerous change has the potential to minimize the progression of these lesions to frank carcinoma. Improvements in early detection would allow for timely lesion excision in order to maximize patient survival while minimizing patient impairment and deformity.

Notably, screening (i.e., detection) and case-finding (i.e., diagnosis) have been mistakenly used interchangeably in epidemiological studies designed to detect pre-cancerous oral lesions in the patient population (29). Screening should always be evaluated with respect to sensitivity, specificity, and predictive values. Such analysis requires that the test outcome from a sample of subjects be compared to the results of an appropriate gold standard (i.e. diagnosis as confirmed by histology of the biopsy) on the same population (29).

The sensitivity of biopsy of lesions that appear higher risk is uncharacterized, as false negative rates (the probability of missing a lesion) cannot be determined unless the entire anatomic site (e.g. entire tongue) is submitted for histologic sectioning following tissue biopsy informed by clinical indication (30–32). Similarly, current specificity rates are unknown, as true negative rates (probability of correct rejection) are not accurately tested and false positive rates (probability of false presence) are not always tabulated at the time of biopsy. For this reason, the reported

sensitivity and specificity of the following OSCC screening techniques vary significantly and may not easily be compared.

Once detected, OSCC is treated with surgical removal of the tumor, radiation therapy, or a combination of both. To maximize treatment efficacy, the tumor must be removed in its entirety. If residual tumor is suspected due to positive margins, bone invasion or lymph node involvement, adjuvant radiotherapy is often also performed.

In addition to maximizing the benefits of surgery by removing as much of the tumor as possible, it is also important to minimize harm and avoid disfiguring the patient. This is particularly significant because primary surgical treatment of OSCC, while associated with good survival outcomes (especially in the early stages), may still cause significant functional disability (e.g., impairments in speech, swallowing, and taste deficits) which can be detrimental to the patient's quality of life (33,34). In order to minimize the symptoms of these side effects and monitor for cancer recurrence, it is important that patients are followed-up consistently post-surgery to screen for recurrent disease. The frequencies of these follow-ups are greatest (once every 1-3 months) during the first few years post-surgery (35), since 80-90% of tumor recurrences occur during the first 2-4 years post-treatment (35–37); after five years of disease-free survival, surveillance frequency can be reduced to once every year.

One of the most important features to evaluate in these follow-ups is the presence of new, abnormal masses. Palpation and examination on physical exam, along with certain symptoms from the patient history (such as hoarseness, dysphagia, otitis media, etc.), can indicate the presence of a mass; however, endoscopy and imaging are generally the two most common methods for the initial detection of tumor recurrence (38). Since laryngoscopy is quick and minimally invasive, it is indicated in most patients for the monitoring of potential tumor

recurrences. Imaging is indicated at least once in the first six months to establish a post-treatment "baseline" reference point; beyond this, imaging should be performed every 3-12 months for the first 2-3 years (35). PET/CT is the preferred imaging modality for tumor recurrence monitoring due to its high sensitivity (39); however, due to the potential harmful effects of radiation due to CT, imaging frequency should be limited, especially in younger patients. As with the initial cancer diagnosis, any lesions or masses detected via physical exam, endoscopy or imaging must be biopsied to confirm the diagnosis of recurrence.

2.1.4 Current Standard Of Oral Cancer Screening

The existing standard of OSCC screening is conventional oral examination (COE) that can be followed by biopsy (9). The clinician is limited in the visual identification of precancerous and early-stage OSCC lesions with COE due to the difficulty of differentiating harmful from similar appearing benign lesions. Due to the lack of a definitive protocol for oral cancer screening, many physicians frequently do not screen for oral cancer; a survey in 2002 found that less than 15% of primary care physicians screened for oral cancer during the initial patient visit (40). Infrequent screenings can be problematic, because pre-cancerous oral lesions are often asymptomatic, vary greatly in their clinical appearance, and often lack clinical characteristics and biomarkers associated with advanced OSCC (i.e., ulceration, induration, and bleeding) (41–43). Improvements in the differentiation between tumor and surrounding normal tissue would represent a considerable advancement towards improving clinical decision making (i.e. biopsy selection), and thus decrease the amount of invasive biopsies performed.

Figure 2-2: Conventional oral examination for head and neck cancer consists of visual inspection and palpation.
Permission requested from Saunders Elsevier, Schwartz, M. H., 2014. Textbook of Physical Diagnosis: History and Examination

Extending into the operating room, surgeons rely on their natural senses of sight and physical touch to localize the contours of a tumor followed by limited frozen section biopsy to establish “clean margins” (2–4). Consequently, the determination of tumor margins by palpation and visual inspection has led to recurrence rates of 25-50% (5,6). These challenges substantiate both a clinical need for improved screening and a related surgical need for intraoperative guidance to localize tumor margins.

2.1.5 Current Standard Of Surgical Margin Assessment

Preoperative imaging techniques (e.g., X-ray, magnetic resonance imaging (MRI), computed tomography (CT), and positron emissions tomography (PET)) have left a meaningful impact on cancer patient care by facilitating early detection, accurate staging, and preoperative planning and treatment (44–47). For the surgeon, however, a major challenge remains clinically translating these images to the operating theater since conventional imaging modalities are neither real-time nor tumor-specific. Additionally, high costs, complex infrastructures, and inaccessibility to surgical fields of view (FOV) are all major drawbacks to their intraoperative surgical use (45,48).

Frozen section, a pathological laboratory procedure used to perform rapid microscopic analysis of biological specimens, is used most often in oncologic surgery to provide guidance for intraoperative margin assessment. After a tumor is presumed to be removed in its entirety, the surrounding tissues are sampled by frozen section to ensure no microscopic disease is left behind. Although histopathologic assessment has a reported specificity of >95%, approximately 19% of patients with histologically negative margins experience treatment failure (48). Many of these patients must undergo a second, re-excision, operation to remove additional tissue, raising concerns about the sensitivity of frozen sections (49). In addition, intraoperative histological assessment extends the time of operation, relies on the quantity of samples harvested from the wound bed and their degree of sampling, and averages as much as $3,123 per patient, with a cost-benefit ratio of 20:1 (50).

Apart from preoperative imaging and frozen tissue section, operating surgeons are essentially limited to two tools - visual inspection and palpation – to select and execute critical decisions that determine the clinical outcome of a tumor resection. Visual and palpable cues, although informative, are highly subjective and are often insufficient for distinguishing malignant and normal tissue types, leading to incomplete resections or unnecessary removal of healthy tissue. Additionally, dependence on white light limits the visual contrast available to surgeons to a narrow range in the colorimetric spectrum. This lack of pathology-specific tissue contrast may in large part explain the suboptimal survival rates in oncologic surgery. Because the primary treatment for most tumors is complete resection, and because positive margins are associated with increased local recurrence and poor patient prognosis, advanced visualization methods that can pinpoint neoplastic tissue and differentiate it from sensitive, healthy tissues are urgently needed (51,52). Specifically, real-time improvement in the intraoperative differentiation between different tissue types would represent a considerable advancement towards improving surgical decision

making (i.e. biopsy selection), and thus, surgical outcomes. Introduction of real-time imaging technologies into the operating theatre has the greatest potential to reduce negative outcomes linked to salvage surgery by guiding the complete resection of tumors at the initial operation (53).

2.1.6 Optical Imaging: A Step Closer to Disease Mapping

Optical imaging technologies offer a feasible solution for real-time, intraoperative guidance of tumor resection and *ex vivo* margin analysis in the head and neck. A good barometer of growing interest in the field is the number of recent publications in the scientific literature: during the past 20 years, particularly in the last decade, the volume of publications on intraoperative optical imaging has nearly doubled (54). Given that 80% to 90% of all cancers originate in epithelial tissue and that the oral cavity is particularly accessible, many studies have evaluated the potential of these technologies to serve as alternate or adjunct tools to traditional techniques employed in intraoperative head and neck tumor assessment (53,55–60).

The central aim of optical imaging is to develop cost-effective technologies that will offer surgeons immediate, real-time margin information that is consistent with the histological diagnosis. In optical imaging of head and neck cancers, the properties of light are exploited to non-invasively probe image alterations in the morphological or biochemical characteristics of tumor tissue. In the domain of optical imaging techniques, contrast can be generated from either intrinsic properties of the tissue or the addition of fluorescent agents to target specific disease biomarkers (53,61). Enhancing the visual differences between diseased and healthy tissue by using optical properties could potentially offer surgeons real-time structure and disease mapping, leading to more complete resections, reduced surgical durations, and decreased morbidity.

The key advantage of optical imaging is that it can be rapidly translated from investigational research to clinical testing. These systems are clinically attractive for their reasonable cost, high

sensitivity, objectivity, speed, flexibility, and ease of use – all key criteria for intraoperative image-guided surgery (**Table 1**) (56). Noninvasive optical imaging techniques that augment tissue contrast and enable surgeons to make histologic evaluations *in vivo*, preceding the gold standard of tissue biopsy, may potentially reduce the risk of unnecessary biopsies; delineate clinical margins for tumor resection; provide guidance for the site of biopsy ; permit real-time re-excision; and optimize or monitor treatment (**Table 2**) (56). Hand-held versions of such intraoperative imaging systems may also ultimately be used by surgeons to make definitive histologic diagnoses in the clinic, obviating the need for general anesthesia. Although there are intrinsic limitations to optical-based technologies, the unprecedented practical and technical surgical possibilities afforded by these real-time imaging systems make them promising tools for head and neck tumor delineation during intraoperative surgical procedures (56,59,62). If surgeons can localize tumors or avoid critical tissues more easily and accurately with optical image-guided surgery than without this technique, operative time could be significantly reduced, thereby improving the patient's overall outcome and risks of morbidity. The long-term potential on patient benefits in management and survival, as well as costs saved in healthcare expenditures, would be resounding.

Table 1: Characteristics of an ideal optical imaging system

- Real-time
- Amenable to both hand-held and endoscopic devices
- High sensitivity
- High specificity
- Independent of operator
- Can be used in the outpatient clinic
- Can be used in the operating theatre
- Easy to use
- Cheap and cost-effective instrumentation

Adapted from (56).

Table 2: Advantages of an optical detection system

- Real-time

- Guide to effective diagnosis
- Guide to effective sampling
- Guide to optimal biopsy without removal of excess tissue
- Guide to treatment during and after operation
- Potential to guide other methods of treatment

Adapted from (56).

2.1.7 Emerging Biophotonic Tools For Non-Invasive Screening Of OSCC

In addition to the traditional imaging modalities described above, recent developments in biomedical optics have resulted in increased clinical attention and significant development for the non-invasive detection, screening, and delineation of OSCC. These modalities utilize a variety of optical techniques, including autofluorescence (VELscope and Identafi), chemiluminescence (Vizilite), and optical coherence tomography (OCT). Each technique possesses advantages, though none have yet to demonstrate significant improvements over COE consistently over clinical trials. The most prominent of optical imaging technologies to identify malignant tissue in oral cavity were characterized and presented in Table 3.

Table 3: Commercialized optical imaging devices for screening of oral cancer.

Product	*Velscope*	*Identafi*	*ViziLite*	*VivoSight*
Optical Mechanism	Autofluorescence	Autofluorescence	Blue-white light illumination	Light back-scattering
Advantages	Easy to use, does not require dimmed light	Three LEDs Targeting multiple fluorophore wavelengths	Enhances acuity and brightness of leukoplakia lesions	High spatial resolution
Disadvantages	Difficult to distinguish between low and high risk lesions	Small field of view, low specificity	Requires dye or acetic acid solution, low specificity	Small field of view

Mechanism of optical image contrast, advantages, and disadvantages for Velscope, Identafi, ViziLite, and VivoSight imaging devices are presented **(63–66)**.

VELscope is an FDA-approved device to image oral mucosal tissue based on autofluorescence intensity of tissue. The device capitalizes on the decreased autofluorescence (i.e., darker region) of abnormal tissue to differentiate among the green emission of healthy tissue. The device is relatively easy to use, boasts a high battery life, and does not require the room lights to be

dimmed. The Velscope, however, does suffers from a low sensitivity and specificity, nearly half that of a standard biopsy; this is characteristic for the majority of commercialized intensity-based autofluorescent technologies. The device emits blue light within the 400 and 460 nm range, resulting in excitation of endogenous fluorophores that have been used to visualize neoplasm margins and tissue abnormalities (67–69).

Identafi uses three different excitation wavelengths, LED white, violet (405 nm), and green-amber (545 nm), to intraorally examine tissue using intensity-based autofluorescence and tissue reflectance. The white light enables highly resolved images of oral mucosal lesions, whereas violet light highlights normal mucosa. The green light reveals underlying vasculature as it matches peak wavelength of hemoglobin. This device was the first intraoral device to enter the market with the ability to evaluate oral lesions using tissue reflectance. Despite its novelty, the violet LED has been shown to offer poor sensitivity for oral epithelial dysplasia, whereas the white and green LEDs offer no new information relative to COE (65).

Vizilite uses a replaceable chemiluminescent light source to illuminate oral mucosa with a blue-white light with average wavelength between 490 - 510 nm. The technology takes advantage of the different reflectance and absorbance of mucosal tissue when in an inflammatory or abnormally metabolic state due to increased nuclear and mitochondrial content (70,71). Normal tissue absorbs the chemo-luminescence and is visibly dark, whereas dysplastic cells are more reflective and appear white. The high contrast margins are due in large to a necessary pre-rinse of suspect tissue with acetic acid solution. Other methods also use Toluidine blue to obtain the sensitivity and specificity paralleling that of COE (71). A vast amount of published clinical studies, however, have deemed Vizilite as insufficient compared to clinical evaluation due to low specificity. The accuracy of Vizlite, however, is also highly variable considering oral dysplasia, as well as the amount of dye administered to tissue (70).

OCT takes cross-sectional images of tissue using the backscattering of light. The technique boasts a resolution in the micrometer range and the technique benefits from high imaging speed. Although OCT is limited to a small field of view, its sensitivity and specificity in detecting abnormalities, particularly leukoplakia and erythroplakia, are both high (roughly 90% and 75%, respectively) (72). Few OCT devices have been commercialized for oral cavity screening due to the limited field of view, concerns regarding endoscope integration, and difficulties in the realization of a hand-held, flexible device. Recently, non-commercialized devices have attempted to mitigate these problems, (e.g., a novel wide field OCT system (64)), and have succeeded with *in vivo* imaging of the oral cavity. A commercialized device that has been utilized in *ex vivo* oral cavity testing is from Michelson Diagnostics, which demonstrates potential in application for *in vivo* use. The company's VivoSight device is clinically used for diagnostic skin therapy and may undergo future design modifications for implementation in the oral cavity. OCT has also been applied to elastography, named Optical Coherence Elastography (OCE), through which images are generated after mechanically perturbing tissue, and has been demonstrated in application to breast cancer. Recent mathematical models to obtain the elastic modulus and potentially quantify the backscattering contrast mechanism is an area of active research (73,74).

2.1.8 Image-Guided Surgery

Sections 2.2 – 2.4 focus on the current status of optical image-guided technologies that have been evaluated for non-invasive tissue identification and intraoperative navigation in head and neck oncologic surgery. Most reports have focused on optical imaging systems that use intrinsic fluorescence or contrast agents to diagnose lesions intraoperatively in patients presenting with OSCC (53,56–58). As a result, the field of fluorescence-guided surgery has grown substantially, and clinical trials are currently underway to evaluate this technology in multiple tumor types. The advantages and limitations of the most common fluorescence imaging techniques, including

autofluorescence imaging, near-infrared fluorescence imaging, and fluorescence lifetime imaging microscopy, will be discussed.

2.2 Melanoma, Mohs Surgery, And Detection Of Micrometastases

2.2.1 Introduction

In 2019 about 7,230 deaths from melanoma occurred with the vast majority attributable to head and neck cutaneous malignant melanoma (HNCMM) (75–77). The standard treatment for primary HNCMM is surgical; The procedure includes wide local excision (WLE) with a safety margin of uninvolved adjacent tissue and often sentinel lymph node biopsy to determine tumor stage (78). About 70-90% of head and neck melanomas occur on the face, and these cases pose a challenge due to limits on the size of surgical margins due to cosmetic deformity, functional impairment, and damage to important nearby anatomic structures (79–81). The conventional means of spot biopsy following tumor resection also suffers significant sampling limitations that leaves the possibility of clinically occult local metastases or residual tumor (81). Altogether, these factors likely contribute to the historically increased rates of treatment failure due to locoregional melanoma recurrence in the head and neck when compared to the recurrence rates at other sites of the body (82–87).

The state of the art treatment (i.e., in the year 2020) for skin cancer resection with a high risk of recurrence and when tissue conservation is essential was actually developed by Dr. Mohs in the 1930s (88,89). Mohs micrographic surgery is performed by removing a thin margin of tissue circumferentially around and deep to the clinical margins of a skin tumor. Immediately following excision the specimen is frozen and sectioned in a cryostat microtome. The freezing and sectioning takes about 15 to 30 minutes. During this time the patient sits in the waiting room with a lightly packaged wound. The dermatopathologist then examines the tissue margins of the frozen sections under a microscope and the process is repeated until the tumor has negative histologic

margins (90). This procedure is expensive, requires a highly specialized surgeon, and is a procedure that is effective if the cancer is diagnosed in an early stage.

Regarding recurrence, multivariate analysis revealed significantly better overall survival for patients with a recurrence being local/in-transit or nodal, asymptomatic, or resectable (91–93). The current methods of surveillance of clinical examination and patient skin self-examination, however, are dated and imperfect for the earliest possible detection of local recurrences or in-transit metastases. This is because subcutaneous or lymph node metastases from melanoma may not be palpable because of their small size, their distance from the skin surface, or their location in an area of fibrosis due to previous surgery or irradiation (94).

Following surgery for HNCMM there is also significant variability in both the frequency of patient follow-up and the appropriate imaging studies for routine surveillance (95). Expert guidelines recommend a combination of ultrasound (US), computed tomography (CT), and positron-emission tomography (PET) for high-risk patients and whole-body screening of metastases but these imaging modalities do not have sufficient resolution to detect micrometastasis and PET/CT are prohibitively expensive for routine surveillance (96). Reports indicate that 70% of first recurrences of primary melanoma are locoregional, and PET/CT also does not evaluate the regional area very well (97,98).

2.2.2 Emerging Biophotonic Tools For Non-Invasive Surveillance Of Melanoma Micrometastases

Next generation emerging imaging techniques may enhance the existing methods for identifying microsatellites and in-situ recurrence in melanoma. Microsatellites are small groups of tumor cells that may occur adjacent to the main lesion in the surrounding tissue (99). In-situ recurrence refers to a "field effect," and applies only to tumors with a radial growth phase (superficial spreading,

lentigo maligna, and acral lentiginous melanoma). Preferable methods for routine surveillance should be safe, cost-effective, and clinically accurate. Therefore, techniques were considered that are noninvasive, do not emit harmful ionizing radiation or use exogenous contrast, image over 1 mm into tissue (in order visualize the epidermis and dermis) and have higher than 1 mm lateral resolution (for detection of micrometastases). Concerning the latest technology in non-invasive imaging, the merits and limitations of high-frequency ultrasound (HFUS), high-resolution optical coherence tomography (HROCT), and photoacoustic imaging (PAI) are presented with respect to their resolution limits for the targeted surveillance for locoregional recurrence following melanoma resection in the head and neck. Significant clinical applications and future directions are also discussed for each imaging technology.

2.2.2.1 High Resolution Optical Coherence Tomography (HR-OCT)

Contrast Mechanism

OCT generates image contrast that reveals the morphology of tissue microstructure based on differences in the index of refraction of specific tissues (100). A benefit of this technique is that the OCT probe does not need to be in contact with tissue since the measurement is based on backscattered light. In addition, OCT can acquire cross-sectional and 3D images with higher precision (compared to ultrasound) when quantifying tissue structures. In OCT, the spectral bandwidth of the light source and the specifications of the optical system define the axial and lateral resolution, while the imaging depth depends on light scattering and water absorption.(101) The light reflectivity of different tissue components (melanin and cell membranes) provides contrast in the images, and these findings do correlate with histopathology (101,102).

Clinical Utility

Clinical use of OCT is rarely reported for diagnosis of melanoma because conventional OCT does not have cellular resolution (103–105). HR-OCT scanners, however, provide a significantly higher lateral resolution, up to 10 um as illustrated in Table 4. The method permits superficial imaging of tissue with morphologic differentiation of the epidermis, papillary dermis, reticular dermis and subcutis. There is a growing body of literature regarding HR-OCT, but a recent systematic meta-analysis had inconclusive recommendations due to the variability of image features used and the standards of reporting in trials (106). Individual reports suggest that HR-OCT has the capability to provide morphological imaging with sufficient resolution and penetration depth to discriminate cytologic features and architectural patterns in the epidermis and dermis for the diagnosis of MM(107,108). One study, however, reported a high overlap in HR-OCT images between benign naevi and malignant melanoma. The authors detail that the architectural and cellular alterations discernible of melanocytic skin lesions included the fusion of rete ridges, pagetoid cells, and junctional and/or dermal nests with atypical cells. The key limitation from the study was that in 20% of MM cases the authors reported HR-OCT images had no evidence of malignancy(109). Further studies support that HR-OCT cannot resolve single cell morphology but does permit assessment of the lesion architecture(110). Images have revealed architectural disarray with an indistinct dermo-epidermal junction, but the inability to clearly visualize the basement membrane zone and cellular features has prohibited rule-out of melanoma based solely on morphological analysis (111).

2.2.2.2 High-Frequency Ultrasound

Contrast Mechanism

Image contrast in High-Frequency Ultrasound (HFUS) is produced from the differences in the acoustic impedance of tissue types that is detected through a pulse-echo, emitted and detected by a transducer. A transducer converts mechanical energy (or sound energy) to electrical energy

and vice versa. The frequency of sound waves produced by a transducer depends on its resonant frequency. Frequencies of 15 MHz or more may be considered high frequency and their use produces higher resolution images of tissues and structures, albeit closer to the skin surface due to a decreased depth of tissue penetration. The decrease in penetration depth occurs because of an inverse relationship with axial resolution that is determined by the pulse duration (bandwidth). Sometimes HFUS is referred to as biomicroscopy because the image produced compares to that of a low-power microscope.

Specifically concerning melanoma, contrast is characterized by a high reflectance from melanocytes and a strong attenuation of the acoustic wave within tumors. Melanin granules (~30 nm diameter within melanosomes) have a refractive index of 1.7 compared with the surrounding cytoplasm of 1.35(112). The strong attenuation of the acoustic wave is a result of the slower speed (1360 ± 50 m/s) of sound in melanoma cells compared to BCC, SCC, and healthy soft tissue (1540 m/s) (113).

Clinical Utility

For clinical use, the diameter and site of the lesion should guide the choice of probe frequency because transducers with higher frequency wavelengths have a decreased depth of penetration.(105) High-frequency ultrasound is considered the best modality for detecting and diagnosing in-transit metastases due to its high accuracy in detecting smaller lesions (114). 7.5 to 15 MHz sonography was helpful in detecting metastases (40-60 mm penetration and 450 um resolution) into the soft tissue in proximity of the primary melanoma tumor (115). Frequencies of 20 MHz to 25 MHz allowed visualization of both the dermis and epidermis while higher frequencies of 50 MHz and above visualize the epidermis only. A transducer at 50 Mhz achieved a resolution of 30-40 μm but a maximum imaging depth of 5-9 mm. A 100 MHz transducer (axial and lateral

resolution of 10 and 84 um) has been reported for very thin metastatic melanomas when the infiltration depth was less than 1 mm.

The scar of the primary cutaneous melanoma, the lymphatic drainage areas, and the regional lymph node basin have been examined by US with a 7.5-10MHz probe. Thus, even with conventional US, in one-third of patients metastases could be detected before being clinically palpable (116). Consequently, lymph node ultrasound is recommended for staging and follow-up of patients with melanomas >1mm in thickness in some European countries (117). With a consensus rate of 90% the current evidence based recommendation (level A) is that ultrasound of the locoregional lymph nodes should be done for the initial workup in all primary melanomas pT1b and higher. However, ultrasound is still not considered as a substitute for sentinel lymph node biopsy. In primary melanoma without a clinically or radiologically positive lymph node, sentinel node biopsy is the most important prognostic factor in primary tumors with a Breslow >1 mm (117).

Ultrasonography (US) surveillance can be more sensitive compared to physical examination for the detection of local and regional lymph node recurrences if performed by a trained professional(116,118,119); as such, ultrasonography has been incorporated into many international guidelines for the follow-up of melanoma patients. Some limitations that have tempered widespread and consistent use included a dependence on operator skill, the availability of an expert radiologist, and a considerable study-performance time. Studies rarely provided information on the expertise and experience of the test operator or sonographer. US has been integrated into clinical practice for over 30 years and a large amount of clinical data is available, but the accuracy of high-frequency ultrasound in identifying melanoma is difficult to interpret due to overall poor reporting and significant heterogeneity between studies. A recent Cochrane

systematic review (20 datasets using HFUS of 1125 lesions and 242 melanomas) detailed patient selection, ultrasound technique, test thresholds, prior testing, and blinding as major sources of the heterogeneity between these studies (106). It is also possible that there was no single parameter in the tested set that was sufficient to discriminate melanomas from other melanocytic skin lesions reliably.[1]

2.2.2.3 Photoacoustic Tomography

Contrast Mechanism

Photoacoustic tomography (PAT) is one of the fastest growing fields in biomedical optics. The technique uniquely combines the benefits of OCT and US in terms of optical excitation with acoustic detection (120). This hybrid mechanism is highly advantageous since optical absorption of endogenous biomolecules (e.g., melanin, water, lipids, hemoglobin) produces tissue-specific contrast (121). In addition, the generated images are high-resolution because acoustic waves scatter less than light in tissue. Ex-vivo experiments have demonstrated a capacity to detect about 200 melanoma cells in a tissue-mimicking substrate and even 6-10 melanoma cells clustered together when circulating in blood (122). This emerging imaging modality is currently transitioning from preclinical to clinical use.

Clinical Utility

By detecting acoustic signals from endogenous biomolecules, PAT could be used to detect melanin from melanoma metastases in the body. Although amelanotic cutaneous melanoma accounts for about 5% of cases, there is actually still enough melanin in the melanocytes to be detected by PAT (123). A notable application of PAT is the quantitative, label-free evaluation of micrometastases within regional lymph nodes. Both in vivo and ex vivo studies for this purpose have been reported, with lateral and axial resolutions of 86um and 119um, respectively (124–128). A notable experiment was performed by Neuschmelting et al in 2016 with PAT in a mouse model.

They reported that PAT enabled detection of melanoma lymph node micrometastases and in-transit metastases that were undetectable with FDG PET/CT and helped differentiate melanoma metastasis from other lymphadenopathies (129). While significant clinical validation is still required, promising early results promote PAT as a highly specific and sensitive label-free imaging approach that may be used to survey the nodal basin for the occurrence melanoma micrometastases. In the future, PAT may especially benefit node-negative patients that currently undergo SLN excision and help detect early stage in-transit melanoma metastases that are currently missed with the use of SLN techniques.

A challenge for PAT using endogenous contrast has been a depth detection limit of about 10 mm and damage to tissue due to light exposure (130). The use of exogenous contrast agents has circumvented this limitation but naturally introduces limitations for clinical use (i.e., allergic reaction, biocompatibility, tumor-specificity) (121). The use of intrinsic chromophores also does not provide information regarding the benign or malignant nature of the cells detected.

Table 4: Emerging non-invasive imaging methods for melanoma detection.

	High-frequency ultrasound	**High-resolution optical coherence tomography**	**Photoacoustic Imaging**
System emits	Acoustic wave	Electromagnetic wave	Electromagnetic wave
System detects	Acoustic wave	Electromagnetic wave	Acoustic wave
Wavelength	(15 - 50 MHz)	~1,300 nm	650-1,300 nm
Lateral resolution (um)	60-250	3-6.5	44-230
Axial resolution (um)	30-120	3-22	28-59
Penetration depth (mm)	4-30	0.5 – 2.0	3.7-4.8
Field of view (cm)	~ 1	~ 0.1 x 0.1	~ 1
Signal from melanocytes versus healthy tissue	Decreased	Decreased	Increased
Probe-tissue contact	Yes	No	Yes
Commercially available?	Yes	Yes	No
Reference	(131),(132)	(131),(108),(133)	(134),(135),(136)

Adapted table from Ref. (132)

2.2.3 Future Outlook

The application of computer-aided detection for real-time data analysis may further increase the sensitivity and specificity of each of the presented methods. Due to digital acquisition, the imaging modalities are generating quantitative and functional datasets that may be used for training deep learning algorithms pending sufficiently accurate (or large-scale) clinical annotation.(137) Alternatively, another emerging non-invasive method is genomic testing for classification of melanocytic lesions in order to guide further biopsy (138). The proposed system can be used as an additional tool for clinical decision support to improve the early-stage detection of malignant melanoma.(139) There exists plenty of room for improvement but even PET can only identify about 50% of subpalpable nodes (140).

OCT was generally most effective when coupled with either HFUS or PAT as a dual modality imaging system (141). The high-resolution iterations of each of these systems was ultimately depth-limited, but there are histologic subtypes of melanoma that may especially benefit from increased local surveillance. Primary melanomas with a purely desmoplastic histologic subtype have a lower risk of nodal and distant metastases and a potentially higher risk of local recurrence.(142) Similarly, the lentigo maligna pattern, which is commonly observed on the head and neck, may be associated with subclinical peripheral and periadnexal extension beyond the visible margins and may require wider surgical margins to clear histologically (143,144).

Additional future applications include pre-operative assessment of lesion dimensions and depth for surgical planning, intraoperative metastasis guidance, and visualization of response to treatment. The 5-year relative survival rate for patients diagnosed with melanoma now exceeds 90%, and the number of survivors is increasing after what was once a dismal prognosis.

Treatments for melanoma are rapidly advancing and there is an emerging need for the identification of patients with locoregional melanoma recurrence who are appropriate candidates for enrollment into clinical trials. Finally, considering the stress of value-based medical treatment, the low cost and burden of each of these modalities merits continued research into their clinical utility and diagnostic accuracy. Pending sufficient evaluation and testing, these imaging tools may significantly augment clinical and patient self-examination to detect recurrent disease.

2.3 Fluorescence Imaging And Autofluorescence In Head And Neck Surgery

Fluorescence imaging for *in vivo* and *ex vivo* characterization of tissue has been well-established for many decades (145). These efforts all share a common aim: accurate delineation of tissues using tissue-specific fluorescence signals. Several studies have demonstrated that cancers, including those of the head and neck, can be accurately identified using fluorescence-guided techniques (53,56,59). Limited improvement in the survival and recurrence rates of OSCC have continued to drive the advancement and evaluation of fluorescence-guided techniques for early diagnosis, staging, and characterization of malignant lesions in the head and neck. More recently, interest has considerably grown in the clinical use of fluorescence imaging methods for intraoperative margin detection, largely due to a more comprehensive understanding of autofluorescence and the availability, decreasing cost, and clinical translatability of the necessary instrumentation (e.g. light sources, optical fibers, and imaging detectors). Using real-time fluorescence properties, optical imaging has the potential to reduce adverse surgical outcomes by offering surgeons guidance in locating the best sites for biopsy, defining the clinical margins for tumor resection, and optimizing or monitoring treatment.

2.3.1 Basic Principles of In Vivo Fluorescence Imaging

The fundamental aim of fluorescence imaging in surgical oncology is to exploit the optical contrast - either intrinsic (i.e. autofluorescence) or induced (i.e. exogenous fluorophores) - between the lesion and surrounding normal tissue. This contrast can be generated from fluorescence intensity, spectral shape, lifetime, or a combination of these features. Most studies using fluorescence imaging in head and neck tumors focus on spectral intensity measurements (62). To more adequately understand how tissue pathology relates to image contrast and the sensitivity of this technique, a brief overview of basic fluorescence imaging principles is detailed in the subsequent sections.

Figure 2-3 illustrates the geometric principle behind fluorescence imaging (62). A spectrally resolved light source (e.g., filtered broadband source, light-emitting diode, or laser diode) is used to deliver a bundle of light with a specific wavelength that can excite a fluorophore. The fluorophore can be an intrinsic tissue component (i.e., autofluorescence) or an injected external fluorescent agent that binds to peptides on tumor-specific cells. This excitation light must then enter and travel through tissue to reach the fluorophore, and therefore, is partly influenced by reflection and refraction at the tissue surface, scattering, and absorption by various components in the tissue. When absorption of a photon results in a gain of energy in the fluorophore, it enters an excited state (Figure 2-3 **(b)**). The electrons briefly remain in an excited state, which is referred to as the ‘lifetime’ of the fluorophore. The system then returns to its ground state following the emission of a photon at a longer wavelength (lower energy); this phenomenon is termed the Stokes shift. The light emitted is captured by a detector or a charge-coupled device camera. Following analog to digital conversion, the camera readout generates an image that is a quantified spatial map of the detected fluorescence.

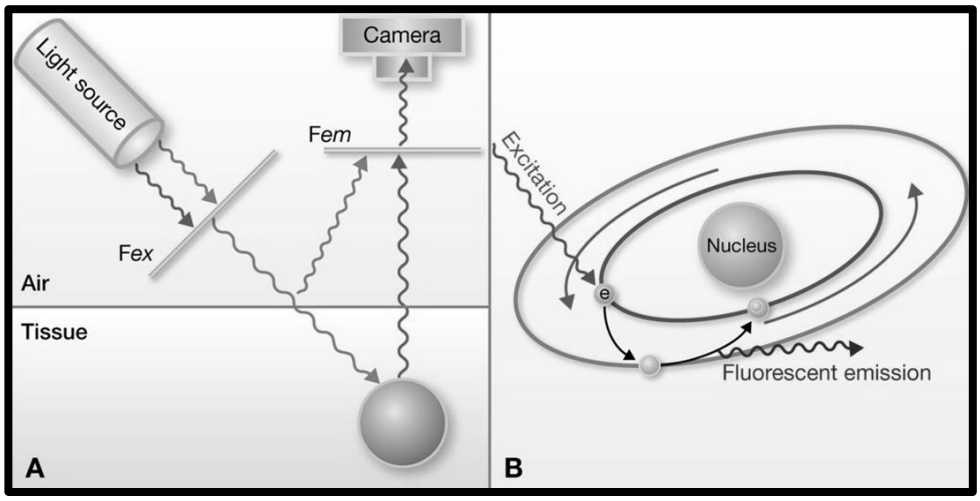

Figure 2-3: Basic principles of fluorescence imaging.
(a) Light of specific wavelength is selected using a filter (Fex) located between a light source and the specimen. The excitation-light is absorbed by a fluorophore, which subsequently emits light of a longer wavelength. A filter (Fem) is placed in front of the detector, which allows only the emitted light to pass into the detector. **(b)** Absorbed light by the fluorophore instigates an electron (e) in the ground state toward an electronically excited state. Upon return to the ground state, the fluorophore emits a photon. The wavelength of this emitted photon is specific for the fluorophore. Fex, excitation filter; Fem, emission filter. Permission requested from the American Association for Cancer Research, Keereweer, S. et al., 2013. Optical image-guided cancer surgery: challenges and limitations. Clinical Cancer Research, 19(14), pp.3745-3754.

2.3.2 Tumor Detection Using Fluorescent Probes

Conventional fluorescent techniques use fluorescent agents, or probes, in the visible light spectrum, which is not ideal for intraoperative image-guided surgery; this spectrum is associated with a relatively high degree of nonspecific background light, often leading to low signal-to-background ratios (SBR) (58). Imaging in the near-infrared (NIR) light spectrum offers a key advantage: increased penetration depth and increased SBR of contrast agents (44,58,146). As a result, NIR fluorescence-guided surgery systems are among the most commonly explored steady-state optical technologies for head and neck cancer surgery.

2.3.2.1 Near-Infrared Fluorescence Imaging Systems And Applications

Numerous commercial NIR fluorescence imaging technologies have been designed for both preclinical and clinical studies of the head and neck (Figure 2-4) (58). The FLARE™ imaging system (Frangioni lab, Beth Israel Deaconess Medical center, MA, USA), which uses specific nanobodies and the NIR fluorophore IRDye800CW to target tumor tissue, has been evaluated in preclinical murine studies, and the Mini-FLARE™ system (an optimized version for clinical studies) has been used to guide fluorescent inspection of sentinel lymph nodes (146). The photodynamic eye camera system (when used in conjunction with indocyanine green (ICG)) has demonstrated the ability to localize lymphatic drainage pathways and detect sentinel lymph nodes in humans (147). The HyperEye Medical System (Mizuho Medical, Tokyo, Japan) has been used for fluorescence imaging-guided tumor delineation in humans after systemic administration of ICG. However, to date, no concurrent histological studies have been performed to verify the observed image contrast (148). The SPY imaging system (Novadaq, Ontario, Canada) is another NIR device used to image and guide head and neck cancer resection in orthotopic animal models (149,150). These studies required the use of peptides conjugated to near-infrared quantum dots. Lastly, FluoSTIC™ (Fluoptics, Grenoble, France), a preclinical device, and its equivalent fluorescence imaging system are hand-held NIR cameras that have been specifically designed for oral oncologic procedures (Figure 2-5**)** (151); both technologies require an intravenous injection of a NIR contrast agent.

Figure 2-4: Near-infrared intraoperative camera systems.
(a) The Novadaq SPY™ system, **(b)** ArtemisTM, **(c)** Hamamatsu's Photodynamic Eye (PDE™), **(d)** Fluoptics' Fluobeam®. Functional intraoperative fluorescence molecular imaging systems: **(e)** FLARE™ imaging system, **(f)** Multispectral fluorescence molecular imaging system from Technische Universität München & Helmholtz Zentrum, **(g)** Surgical navigation system GXMI Navigator from the Institute of Automation, Chinese Academy of Sciences. Permission requested from IvySpring, Chi, et al., 2014. Intraoperative imaging-guided cancer surgery: from current fluorescence molecular imaging methods to future multi-modality imaging technology. Theranostics, 4(11), p.1072.

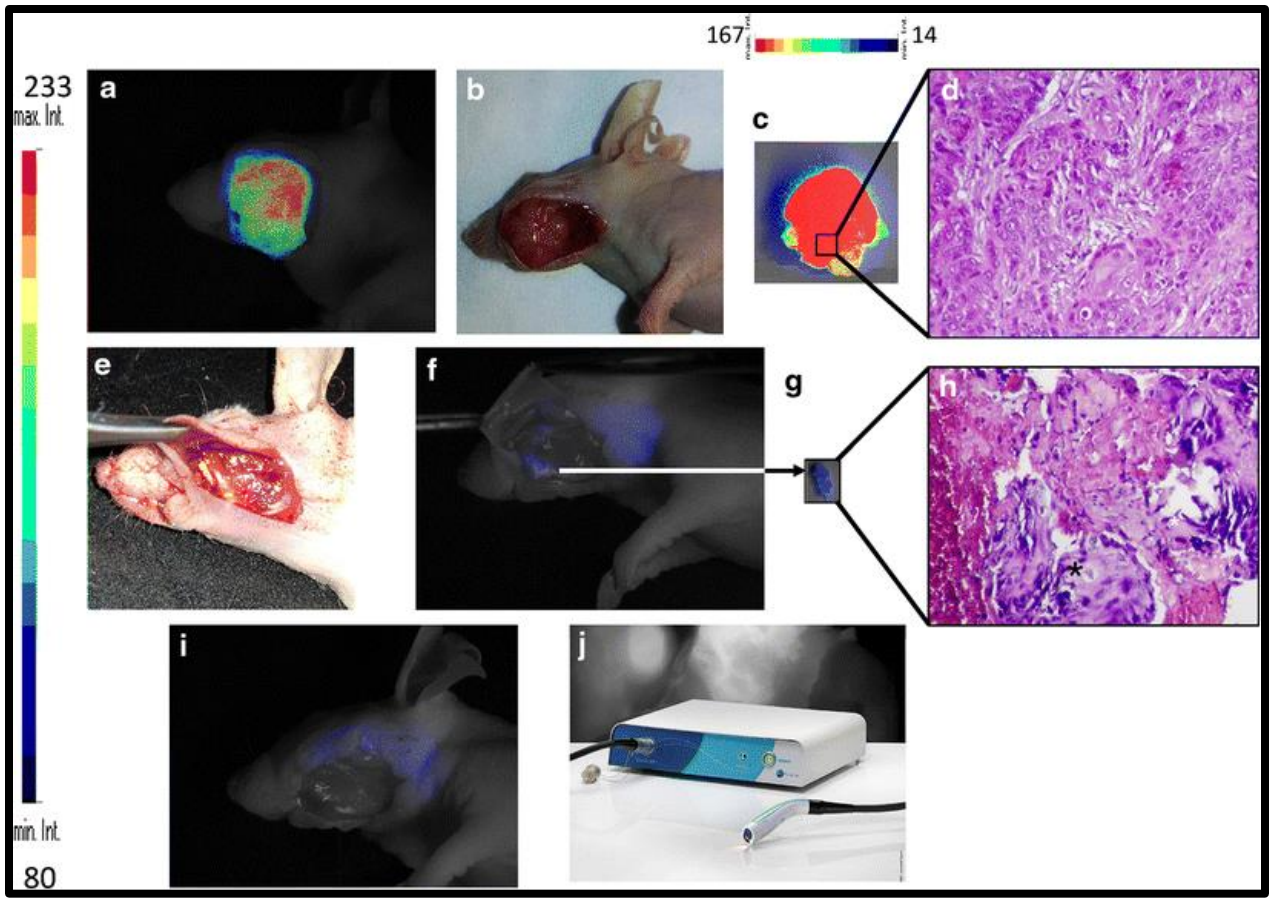

Figure 2-5: Orthotopic tumor resection with the aid of a FluoStick™ Clinical System device after systemic injection of the AngioStamp™ 800.
(a) *In vivo* fluorescence imaging of the tumor. **(b)** *In vivo* macroscopic appearance of the tumor. **(c)** *Ex vivo* fluorescence imaging of the tumor after macroscopic resection without the aid of FluoStick. **(d)** Haematoxylin-eosin (HE) staining of the orthotopic tumor. Microscopic images were acquired under 20× magnification. **(e)** Surgical bed after macroscopic tumor resection showing no residual macroscopic disease. **(f)** Fluorescence imaging of the surgical bed. **(g)** *Ex vivo* fluorescence of the fluorescent residue. **(h)** HE staining of the fluorescent residue. Microscopic images were acquired under 20× magnification. **(i)** No residual fluorescent signal observed in the surgical bed after removal of the fluorescent tissue. **(j)** The FluoStick™ Clinical System. Permission requested from Springer, Atallah, I., et al.., 2015. Role of near-infrared fluorescence imaging in head and neck cancer surgery: from animal models to humans. *European Archives of Oto-Rhino-Laryngology*, *272*(10), pp.2593-2600.

2.3.2.2 Challenges For Clinical Translation

The key challenge in intraoperative NIR fluorescence imaging lies in the clinical translation of tumor-specific agents (47,146,152). As noted in the previous section, NIR fluorescence guided

surgery requires a fluorescent probe and a compatible imaging device. Clinical use and development of these components has been significantly limited considering Food and Drug Administration (FDA) approval of standardized imaging devices and agents is costly, of unknown toxicity, and very time-sensitive (54,153); limited benefits are expected compared to traditional therapeutic agents used to target head and neck cancers. Among the few number of fluorescent probes that have been approved for clinical use, ICG, a non-targeted dye, is the only NIR fluorescent agent that has been approved by both the FDA and European Medicines Agency (58). Fluorescein has been recommended for tumor imaging. However, this contrast agent is highly soluble and very rapidly cleared *in vivo,* making it unsuitable for this application (154). Pharmacokinetics and clinical toxicity studies need to be performed for other probes that have demonstrated effective targeting of head and neck cancers in preclinical studies.

Although NIR fluorescence imaging is based on the detection of photons, Figure 2-3 illustrates how the spectral shape and intensity of emitted light may be significantly affected by optical properties of the tissue (i.e. absorption and scattering) (62). As a result, observed fluorescence image contrast is often blurry due to surface scattering effects and characterized by distorted intensities due to the varying absorptive properties of tissue. The majority of NIR fluorescence systems are limited to single-band NIR cameras that do not enable separation of background light from the probe signal, and, thus, cannot correct for spectral and intensity distortions caused by unique photon-tissue interactions (44,53). Imaging over a range of wavelengths may allow for this correction, however, such a correction scheme is cumbersome cannot be performed in real-time, a fundamental component of intraoperative image-guided surgery (44).

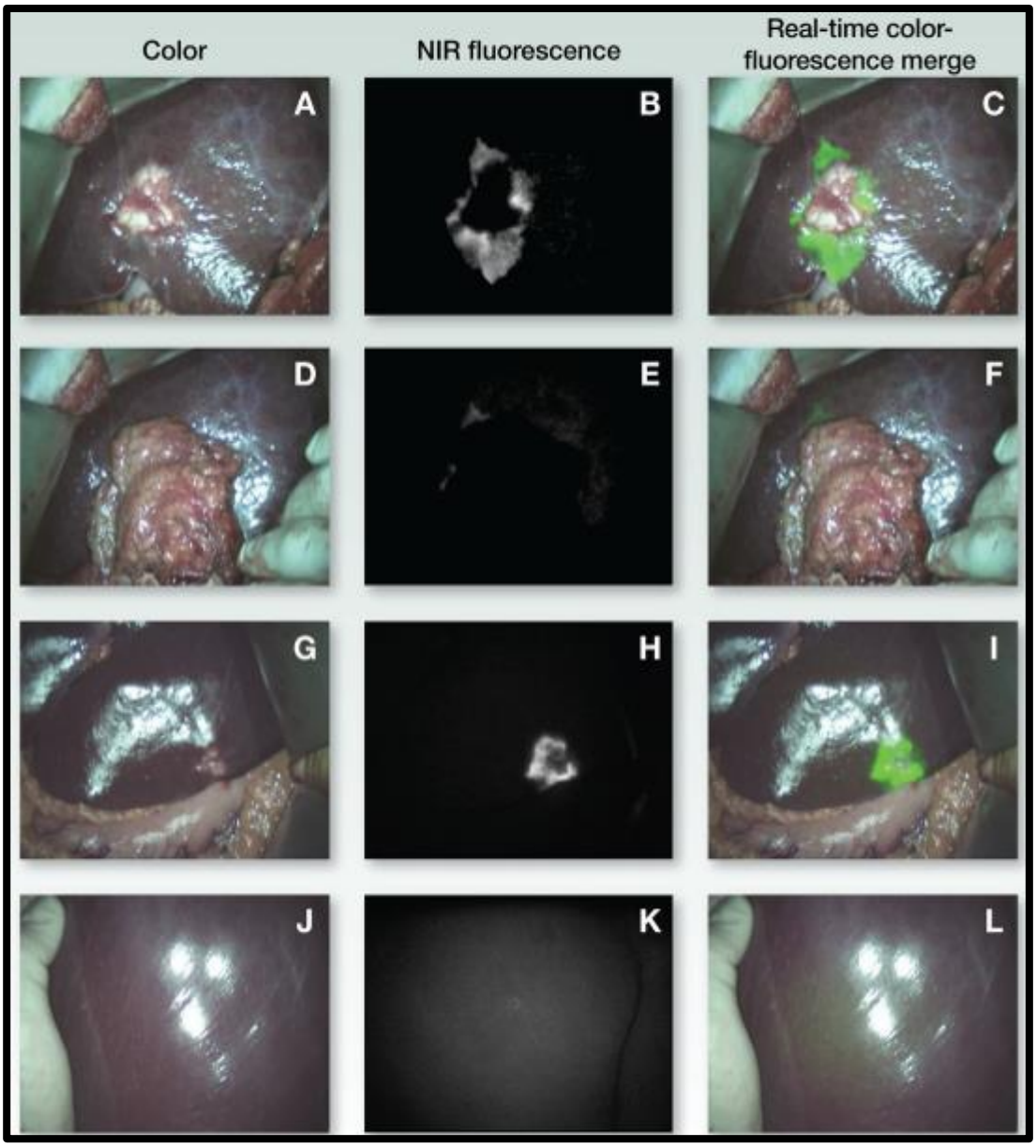

Figure 2-6: The effects of absorption and scattering on image contrast during real-time intraoperative fluorescence imaging of liver metastases in humans. At the surface, fluorescent agents will appear as a bright and sharply delineated spot. However, the target will always be surrounded by a halo of fluorescent light that is directed into the tissue after emission, scattered around locally, and then emitted from the surface at some distance from the target location. Moreover, due to absorption and scattering, an identical fluorescent agent that is located deeper within the tissue will have lower signal intensity and will be imaged as an indistinct feature. An example is shown of a liver metastasis that is delineated by fluorescence signal **(a-c)**. When a thick layer of greater omentum covers the area of interest, fluorescence signal is not detected **(d–f)**. A second liver metastasis is indicated in a different patient **(g-i)**. However, when the liver is flipped around and the opposite side is imaged, high absorption of the liver that is saturated with blood results in an indistinct fluorescent blob **(j–l)**. Permission requested from the American Association for Cancer Research, Keereweer, S. et al., 2013. Optical image-guided cancer surgery: challenges and limitations. *Clinical Cancer Research*, *19*(14), pp.3745-3754.

2.3.3 Tumor Detection Using Intrinsic Fluorescence

Autofluorescence (AF) describes the intrinsic fluorescence of tissue that is excited by visible or ultraviolet light of a specific wavelength. Because the optical properties of tissue are influenced by tumor-induced morphologic and biochemical changes, AF serves as a useful diagnostic indicator because it can be used to illuminate structures of interest (155). This is a significant advantage for image-guided surgery, as there is no need for exogenous fluorescence agents that can often complicate the regulatory approval process for clinical use.

Several studies have confirmed a loss of normal tissue AF in cancerous tissue as compared to healthy parenchyma (155–159). The reasons for AF alteration in neoplastic tissue are broad and attributed to alterations of intrinsic tissue fluorophore distribution. The dynamic tumor fluorophore landscape include break-down of collagen matrices, reductions in flavin adenine dinucleotide concentration during cellular remodeling, and upregulations in tumor metabolism (e.g. increases in nicotinamide adenine dinucleotide (NADH) concentration) (155,160–163). As a result, AF profiles are of particular clinical interest because changes in metabolic activity and cellular interactions can be reflected by spectral changes in emitted fluorescence.

2.3.3.1 Imaging Systems and Applications

The efficacy of AF-guided surgery in improving OSCC disease recurrence and overall survival, as assessed by surgical site and regional lymph node status, was recently investigated (155). VELscope (LED Medical Diagnostics, Vancuover, Canada) is the only commercially available handheld AF device for visualization of tissue fluorescence in the oral cavity. Under fluorescence visualization, normal oral mucosa emits various shades of pale green AF, while lesions appear as dark patches (Figure 2-7**)**. Among the 156 patients with squamous cell carcinoma, the 92 patients in the AF-guided surgery group showed a significant reduction in the 3-year local

recurrence rate, from 40.6% (26 of 64 patients) to 6.5% (6 of 92 patients) ($P < .001$). Multicenter, phase 3, randomized surgical trials have been proposed to validate the results of this study (155).

2.3.3.2 Challenges For Clinical Translation

Most AF studies have discriminated between normal and tumor tissue in the head and neck by detecting differences in measured steady-state fluorescence intensities or spectra. Although simple to use, both techniques suffer from limitations that make quantitative analysis of image

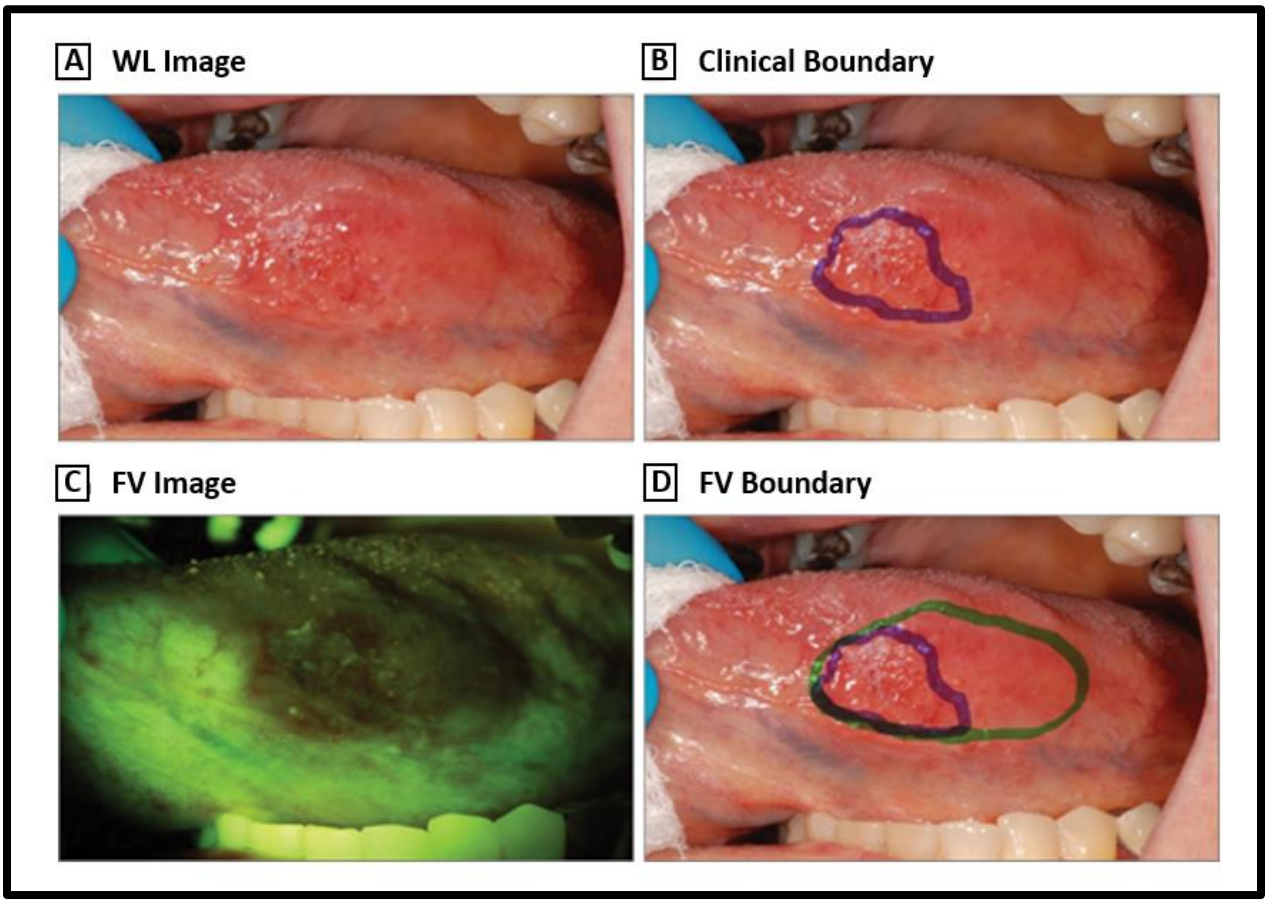

Figure 2-7: Representative Clinical Lesion Assessment with white light (WL) and Fluorescence Visualization (FV).
(a) A WL image of an ill-defined red lesion at the left lateral tongue. **(b)** The clinical tumor boundary is outlined using a blue skin marker. **(c)**, FV image at the same area. **(d)**, The FV boundary is outlined using a green marker. Permission requested from the American Medical Association, Poh, C.F., et al., 2007. Direct fluorescence visualization of clinically occult high-risk oral premalignant disease using a simple hand-held device. *Head & neck*, *29*(1), pp.71-76.

contrast challenging (164,165). The contrast generated with steady-state AF imaging techniques is not only influenced by the concentration and fluorescence quantum yield of the fluorophore but also by: 1) temporal and spatial properties of the excitation flux; 2) angle of the excitation light; 3) detection efficiency; 4) spatial variations in the tissue microenvironment; and 5) attenuation by light absorption and scattering within the tissue (62,164). The clinical implications are particularly evident when imaging highly vascularized lesions or organs since blood and its components are highly light-absorbent and reduce the fluorescence signal created (44,166). Therefore, blood may mask the potential fluorescence signal produced in tissues containing high concentrations of fluorophores when compared to adjacent non-vascularized tissue beds of lower fluorophore concentration (167). In addition, reduced AF associated with malignant tissues is also exhibited by a variety of other conditions, such as inflammation, keratosis, and benign lesions, thereby limiting the clinical utility of intensity and spectral-based AF measurements for intraoperative margin control (168). Technical improvements in signal analysis and quantitation have been made through ratiometric imaging utilizing spectral emissions windows, yet the heterogeneity in tissue fluorophore distribution and their broad overlapping emission spectra continue to limit the degree of achievable discrimination (155). The clinical utility of AF contrast imaging is clearly apparent yet the above considerations have limited the widespread adoption of AF intensity imaging for the detection of neoplastic tissue. The current AF imaging tools in clinical use are hampered by low specificity and a high rate of false positive findings (44,53,62).

2.4 Fluorescence Lifetime Imaging

2.4.1 Fluorescence Lifetime Imaging: Robust *in vivo* Contrast

Time-resolved techniques such as fluorescence lifetime imaging (FLIM) add a further dimension to AF intensity and wavelength measurements by analyzing the temporal properties of emitted fluorescence (164,169,170). FLIM permits differentiation between individual fluorophores in

malignant and normal tissue by visualization of the specific temporal decay after excitation(164,171,172). The key advantage of measuring the fluorescence decays (i.e. lifetime) of fluorophores is that this parameter is directly dependent upon excited-state reactions and independent of local fluorophore concentration, attenuation due to tissue scattering and absorption (e.g. blood), nonuniform tissue geometry, optical path, local excitation intensity, and local fluorescence detection efficiency(173,174). While these factors may significantly affect the signal and detection capabilities of intensity-based AF systems, the ratiometric nature of lifetime measurements in FLIM is robust against imaging artifacts and confounders. Unlike fluorescence intensity imaging, fluorescence lifetime is sensitive to several chemical and metabolic variables in the tissue microenvironment (including pH, ion concentration, binding states, enzymatic activity, and temperature) (174,175). In this way, fluorescence lifetime measurements complement intensity and spectrum measurements by providing additional information on the composition and function of tissue (164,170,176). In cancers of the head and neck it has been reported that the main metabolic contributor to the fluorescence emission is a co-enzyme (NADH) associated with cellular metabolism (177–179). During disease progression from healthy to malignant, the contribution of NADH fluorescence from tumor tissue rises substantially, resulting in a sub-nanosecond lifetime (~0.5 ns) in unbound form and a lifetime greater than 1 ns in a bound form(180). The observed reduction of fluorescence lifetime results from changes in biochemical composition and morphology in head and neck cancer tissue. Furthermore, FLIM can easily differentiate between biomolecules with overlapping fluorescence emission spectra that have different fluorescence lifetimes. Complete emission spectra can be generated by measuring time-resolved fluorescence at wavelengths across the entire emission spectrum. Time-resolved fluorescence measurements acquired with FLIM, thus, have inherent advantages over steady-state fluorescence systems for reliable and quantitative analysis of biological tissue.

2.4.2 FLIM Instrumentation and Data Analysis

FLIM systems record the time-resolved fluorescence intensity of fluorophores to generate images. Fundamental to lifetime imaging is acquisition of the time-decay interval following fluorophore excitation. Methods for measuring fluorescence lifetime are usually divided into time domain and frequency domain techniques(181). Regarding time-domain techniques a schematic diagram of fluorescence lifetime decay is illustrated in Figure 2-8. In the time domain method, cells are first excited with a short duration (< 1-2 ns) pulse-width energy source with an ideal pulse interval duration that is shorter than the fluorescence lifetime (τ) to be measured. When a molecule absorbs energy of suitable wavelength it transitions to from a ground to an excited state. Upon relaxation and return to the ground state, the molecule then emits fluorescence with typically longer wavelength in the form of a radiation transition. Fluorescence lifetime is the average amount of time that the molecule stays in its excited state before emitting a photon, and is usually defined as the time required for the fluorescence intensity to decay from its maximum value to 1/e of its maximum value(181). The decay of fluorescence intensity immediately following excitation (often modeled as a Dirac delta function if a pulsed laser is used for excitation) will decay exponentially with time. For a single molecule, the fluorescence lifetime (τ) may be modeled by the single exponential function detailed in Equation 5-1.

$$I(t) = I_0 e^{-t/\tau} \qquad \text{(Eq. 2-1)}$$

In Equation 5-1, t is the time (in nanoseconds) following molecule excitation, I_0 is a constant determined by the magnitude of excitation and the quantum efficiency of the fluorophore with peak at $t = 0$, and $I(t)$ is the fluorescence intensity at time *t* (182,183). In reality, the fluorescence decays from each point in the produced image are more complex than a single exponential model. In biologic tissue, the presence of multiple fluorophores in a range of different microenvironments

results in emitted fluorescence from an area that is composed of the superposition of many fluorescent lifetimes. Thus, a multi-exponential function (Equation 5-2) is required where $\tau_i$is the fluorescence lifetime of the (i)th fluorophore, and α_i is its weighted contribution, respectively(184).

$$I(t) = \sum_{i}^{n} \alpha_i \, e^{-t/\tau_i} \qquad \text{(Eq. 2-2)}$$

Fast and sensitive detectors (e.g., avalanche photodiodes, streak cameras (640 spectral x 480 temporal channels), gated intensified charge coupled device (iCCD) cameras (repetition rate maximum of 10 MHz, time gate 200 ps), and time correlated single photon counting (TCSPS) detection modules) are usually necessary to record the time-dependent distribution of emitted photons following each pulse considering the nanosecond order of the fluorophore decay. (176,182). The rate of decay (i.e. “lifetime”) of fluorescence at each point in the image is plotted as a distribution of fluorescence ‘lifetime’ values (τ). In the presence of fluorophores the slope of the decay curve is less steep due to the existence of a finite excited state. Thus, fluorophores with longer lifetimes are characterized by larger slopes (182). Based on the specific lifetime of the fluorophore, florescence between normal and cancerous tissue can be distinguished. To date, the differences in fluorescence lifetime between normal and neoplastic tissue has been reported for both *ex vivo* and *in vivo* tissues (i.e., including the breast, brain, colon, esophagus, and oral cavity) (178,185–194). Details of the measurement methods, instrumentation, data acquisition, and analysis of fluorescence lifetime imaging methods are extensively detailed in comprehensive reviews on this subject (176,181,182,195–199).

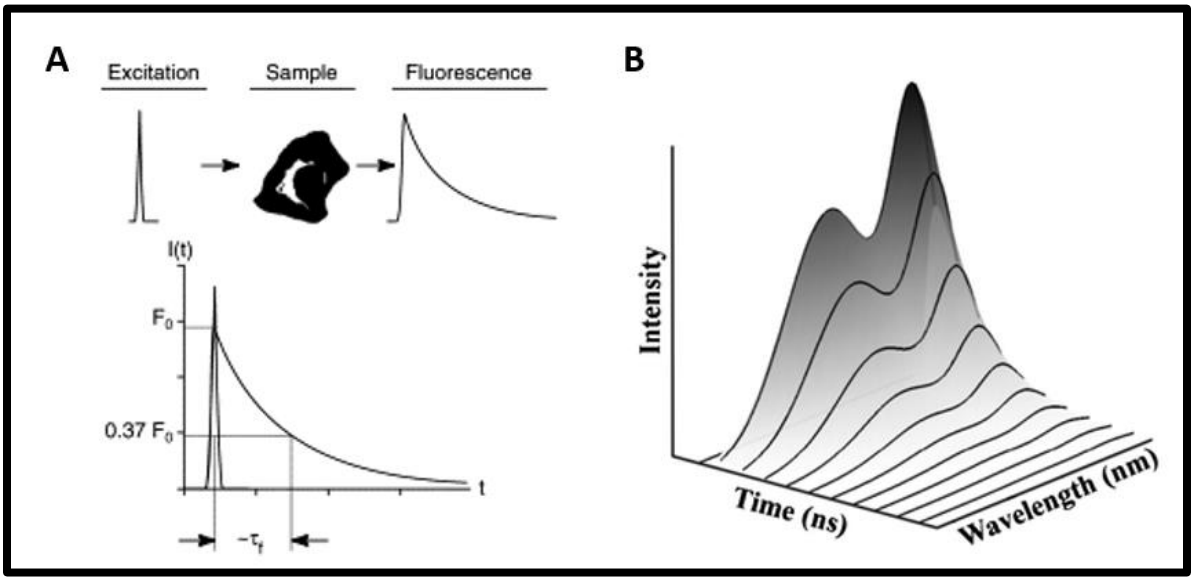

Figure 2-8: The Principle of Time-Domain Fluorescence Lifetime Measurement. **(a)** In the time domain, the fluorescence lifetime is directly measured upon excitation of the sample with a short pulse of light, where the duration of the pulse is ideally much shorter than the fluorescence lifetime (τ) to be measured. This results in a fluorescence emission whose intensity decreases exponentially with time. For a sample comprising a single fluorescent species, the fluorescence lifetime is given by the time over which the fluorescence intensity drops to about 37% of its initial value. **(b)** Spectro-temporal profile of fluorescence emission in response to an excitation light stimulus. Permission requested from Elsevier, Bastiaens, P.I. and Squire, A., 1999. Fluorescence lifetime imaging microscopy: spatial resolution of biochemical processes in the cell. *Trends in cell biology*, *9*(2), pp.48-52.

2.4.3 Clinical Applications of FLIM in the Head and Neck

Steady-state fluorescence spectroscopy and imaging studies have shown high sensitivity in the head and neck, yet these techniques suffer from poor specificity in identifying tissue pathology. Time-resolved measurements acquired with FLIM have the ability to fundamentally improve the specificity of fluorescence imaging and consequently advance tissue fluorescence-based diagnostic accuracy. The diagnostic potential of this method has not been fully evaluated given the limited number of patients enrolled and studies performed employing time-resolved techniques (174). Among the published head and neck literature, the primary objectives of FLIM investigations are: 1) determine differences in lifetime fluorescence between normal and

malignant tissue of the head and neck; 2) evaluate the potential of FLIM as a diagnostic tool for oral and head and neck squamous cell carcinoma (OSCC); 3) evaluate FLIM as an intraoperative tool for detection of residual tumor tissue in cancer surgery.

Lifetime measurements have been successfully used to distinguish normal mucosa from premalignant lesions in human oral tissues(174). In a pilot study of nine patients with suspected OSCC, time-resolved laser-induced fluorescence imaging microscopy demonstrated malignant tissues of the aerodigestive tract are characterized by shorter lifetimes as compared to those of normal tissue(174). The potential of intraoperative endoscopic FLIM has also been investigated to accurately diagnose lesions in a group of 10 patients presenting with OSCC (174,180). As shown in Figure 2-9, OSCC exhibited a weaker fluorescence intensity (~50% less) when compared to healthy normal tissue and a shorter mean lifetime (τ_{HNSCC} = 1.21 ± 0.04 ns) than surrounding tissue (τ_{N} = 1.49 ± 0.06 ns) (180)**.** Although having previously been implemented in the operating room, FLIM must overcome several challenges before the technology can become a practical clinical tool**.**

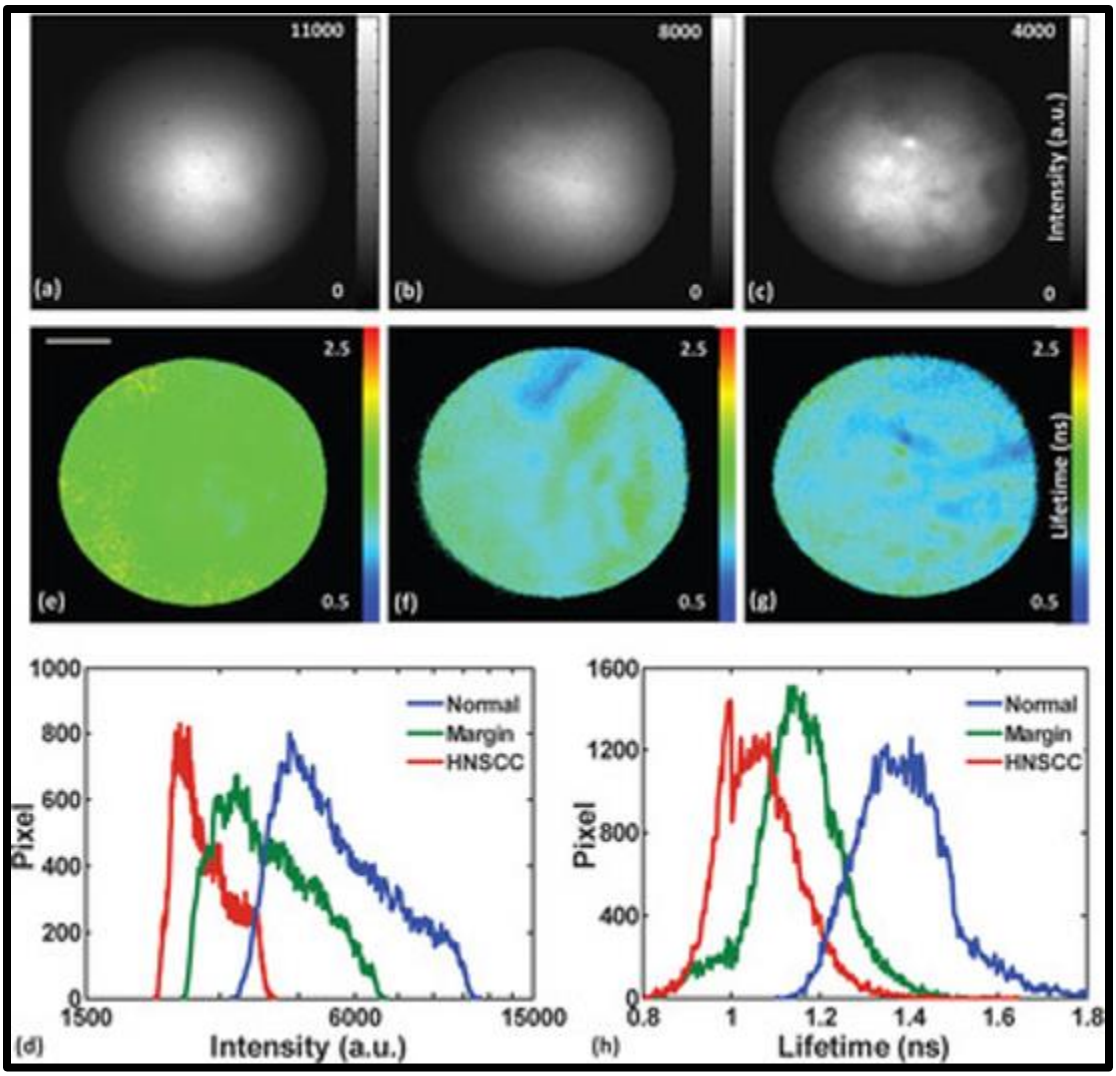

Figure 2-9: Endogenous fluorescence lifetime imaging microscopy images of human buccal mucosa.
(a)–(c) depict the intensity images, and **(e)–(g)** depict the average lifetime images from three areas: normal, tumor, and adjacent normal-tumor, their corresponding histograms are depicted in **(d)** for intensity and **(h)** for average lifetime. ONSCC, head and neck squamous cell carcinoma. Permission requested from the Cambridge University Press, Sun, et al., 2013. Endoscopic fluorescence lifetime imaging for in vivo intraoperative diagnosis of oral carcinoma. *Microscopy and Microanalysis*, *19*(4), pp.791-798.

2.4.4 Challenges for Clinical Translation

Due to technological challenges in measuring lifetime decay on a picosecond timescale, only a handful of studies have been published on the application of time-resolved fluorescence for

intraoperative margin detection of OSCC (176,178,193). Clinical integration of FLIM technologies (particularly in screening for disease, guided biopsies, or intraoperative imaging) has been significantly hampered by their 1) instrumentation requirements; 2) image acquisition methods; and 3) complex data processing techniques (Table 5) (62). Most FLIM studies evaluate the capabilities of laser scanning microscopy systems, however, their limited FOVs (intended for cellular research) are not applicable for large field, intraoperative, or clinical use (173,193,200,201). Repeated point measurements or probe attachments used to screen larger fields of view are laborious, time-consuming, and sacrifice the spatial resolution of the AF signal. These techniques thus offer little morphological information concerning the tissue under investigation.

Table 5: Key limitations preventing the clinical translation of FLIM

Limitations	Clinical Challenges
• Complex and expensive instrumentation and limited availability of light sources and sensitive detectors	• Limits development of practical research/clinical instrumentation
• Slow data acquisition speeds	• Reduces the amount of data recorded from patients, thus impeding statistical evaluation of the results
• Lack of analytical methods for accurate representation of fluorescence decay profile from measurements in tissues	• Difficult to interpret the decay profile and its relationship to tissue pathophysiology

FLIM systems typically require high repetition rate pulsed lasers or rapidly modulated continuous wave (CW) lasers (traditionally cost prohibitive for wide-scale investigation) to generate the temporal profile of the illumination pulse. Additionally, improved methods for analyzing the complex decay profile of multiple lifetimes and quantitatively reporting lifetime changes in heterogeneous tissue are still required. FLIM datasets are typically large and render the fitting of mono-exponential decay curves to experimental data very time-consuming and processor capacity-dependent (202,203); the additional post processing steps required to display the image further delay fluorescence lifetime mapping (202). Collectively, these issues are likely to preclude

FLIM spectroscopy and laser scanning systems from many intraoperative and clinical point-of-care applications where mobility of equipment and computational speed are necessary to enable physician incorporation of data into their delivered treatment.

CHAPTER 3: **DYNAMIC OPTICAL CONTRAST IMAGING**

3.1 Towards The Clinical Application Of Time-Domain Fluorescence Lifetime Imaging

Taking into consideration the limitations to clinical translation of traditional FLIM systems (detailed in section 2.4.4), several techniques and algorithms have recently emerged to increase FLIM performance and recording speed of FLIM in biological and biomedical applications(204). Algorithms that require fewer images to calculate decay parameters have gained increased attention due their potential to permit in vivo real-time clinical imaging while staying under the limits of maximum excitation power as determined by resultant photodamage and the ANSI standards. Considering the simple case of a one-component fluorescence lifetime measurement, the fluorescence lifetime of the molecule may be calculated using at minimum two frames if the attenuation of the fluorescence intensity from the region of interest is measured at two different times (t_1, t_2), according to Equation 6-1 (184).

$$\tau = \frac{(t_2 - t_1)}{\ln (I_1/I_2)} \qquad \text{(Eq. 3-1)}$$

In Equation 6-1, I_1 and I_2 are the fluorescence intensities detected at time t_1 and t_2. This algorithm is the rapid lifetime determination (RLD) algorithm. Benefits of the RLD algorithm are that it is non-iterative and minimizes the acquisition time (204,205). An assumption of the method is that the illumination profile on the detector corresponds to the true fluorescence decay of the sample. This is actually a source of accuracy error because the excitation laser pulse has a finite width and the laser pulse width should be at least two orders of magnitude shorter than the fluorescence lifetime of the fluorophore studied. If a wider laser pulse width were to be used in the RLD algorithm the convolution between the laser pulse and the fluorescence decay widens the

illumination profile and has been described to degrade the accuracy of RLD determined lifetimes(206).

3.2 DOCI: Innovation and Theory

Our research group designed and developed a clinically relevant system to generate clear and meaningful contrast from *differences* in fluorophore lifetimes without the need to compute *absolute* lifetime values. This optical imaging technology is termed Dynamic Optical Contrast Imaging (DOCI) (207–211). The intrinsic contrast mechanism utilized by DOCI is the same as utilized by FLIM in which the endogenous fluorophore lifetime of tissue is probed by illumination with a pulsed long-wave ultraviolet (UV) light source. However, in contrast to illumination using the narrow pulse of a laser the DOCI system relies on light from an illumination source that is ideally a quasi-square wave and permits use of less expensive light emitting diodes (LEDs) with pulse shapes that are on the same order of magnitude as the lifetimes of the investigated fluorophores. Only two data points are acquired with this method that contain sample fluorescence (i.e., three frames are acquired overall if counting the background image). Each data point is produced via integration of the fluorescence intensity over a specific time interval. For the two data points containing sample fluorescence, the two time intervals are referred to as the “steady-state” (producing the calibration image) and the “decay-state” (producing the decay image). The steady-state detected fluorescence serves as a reference peak for normalization of the integrated intensity measured in the decay state. A detailed mathematical derivation was previously performed that details the merit of the DOCI contrast mechanism(210–212). Overall, through a unique image frame normalization scheme (illustrated in Figure 3-1**)** DOCI generates pixel values that are proportional to the aggregate fluorophore of the probed tissue without the requirement of fitting complex mathematical models to acquired data(213). This relaxes the requirements on the temporal profile of the illumination pulse and enables the replacement of picosecond pulsed lasers

(that are required for FLIM) with nanosecond pulsed light emitting diodes (LEDs). With these improvements the scalable mapping of fluorophore lifetimes over macroscopic (not microscopic) fields of view (FOV) has been possible within a relatively short time frame (~ 10 seconds per emission band), with all pixels acquired simultaneously. These improvements thus provide a significant step towards intraoperative clinical use.

$$\text{DOCI value per pixel} = \frac{\int_B^C f(x)dx - background}{\int_A^B f(x)dx - background} \qquad \text{(Eq. 3-2)}$$

The strength of DOCI is that it converts fluorophore lifetime into contrast by computing the area under the decay time curve normalized to the steady state fluorescence. In the limit of stationary noise this process is robust to variations in obscurants and can produce significant contrast under low SNR. Further, unlike standard FLIM, contrast is enhanced when the gate width is increased as it increases the overall number of collected photons while reducing noise variance. The simplicity and intrinsic sensitivity of the technology enables rapid imaging of large (several centimeter) FOVs practical for clinical imaging.

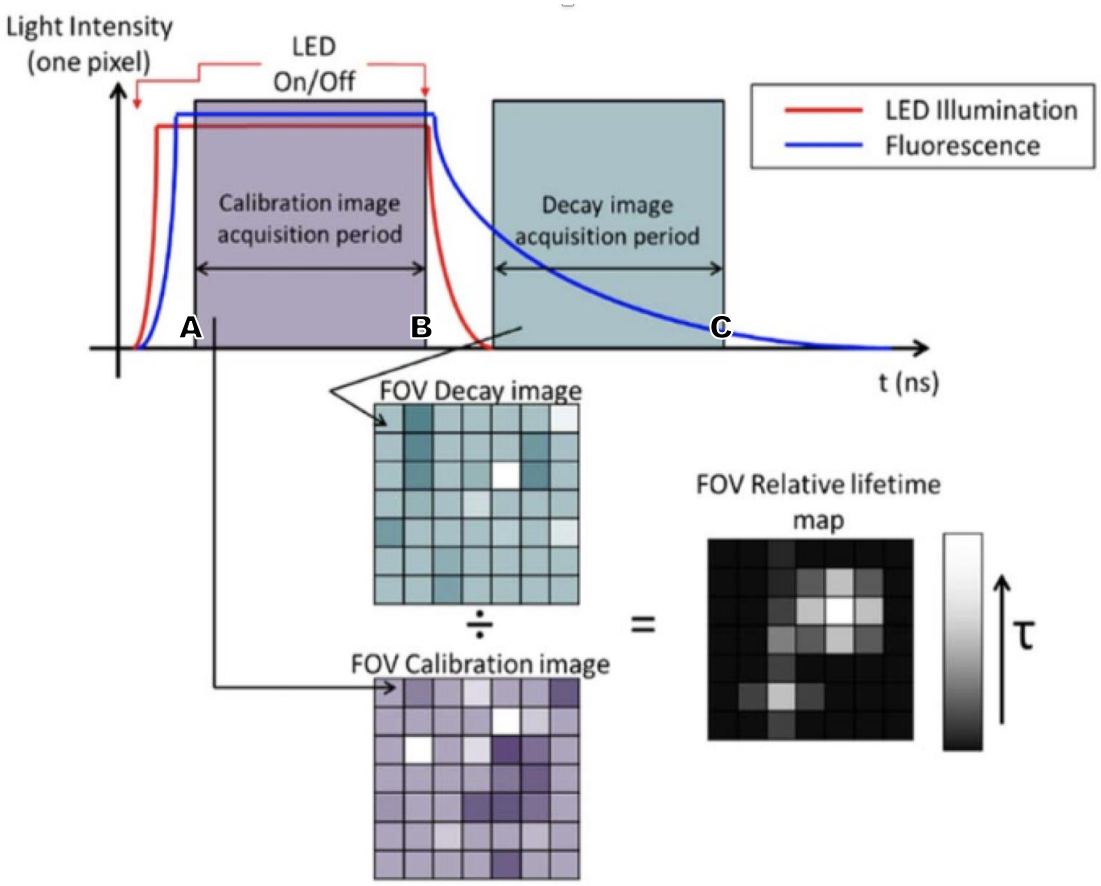

Figure 3-1: Method of Dynamic Optical Contrast Imaging.
Image modified and permission requested from John Wiley and Sons, Tajudeen, B.A., et al., 2017. Dynamic optical contrast imaging as a novel modality for rapidly distinguishing head and neck squamous cell carcinoma from surrounding normal tissue. *Cancer*, *123*(5), pp.879-886.

DOCI utilizes a UVA band LED light source operated in relatively long pulse durations (~ 30 ns) with nanosecond order rise and fall times to produce contrast between fluorophores of different decay rates. A pictorial representation of this concept is displayed in Figure 3-1 and additional details are discussed in the subsequent sections. A nanosecond gated intensified charge coupled device (iCCD) is oriented to detect the fluorescence emission from the area of interest.

Following normalization of the decay to the calibration image the resulting pixel values may alternatively be considered as a lifetime-weighted sample of the quantum yield from intrinsic

biologic fluorophores. The fluorescence lifetimes of most tissue constituents of interest in head and neck imaging fall within the range of 1 ns to 10 ns (214–216). Thus, usually after 10ns following the illuminating LED reaching peak intensity the fluorophores in tissue are pumped to a steady state where the rate of fluorescence decay from the excited state equals the rate of LED dependent pumping to the excited state. The lifetime-dependent emission image is acquired at > 10 ns following the illuminating LED reaching peak intensity because the dominant fluorophores in tissue must reach a steady excited state. This time is of course an approximation because the fluorescence lifetime (τ) of a molecule depends on competing decay pathways (i.e., radiative and non-radiative decay). To calibrate the fluorescence emissions acquired, images are captured: (1) mid-UV pulse duration (>10 ns) and termed “calibration image;” (2) at the beginning of illumination pulse decay, termed “decay image”. A third dark image (not shown) is obtained at over 10 times the longest expected decay for the purpose of flat-fielding the intensity and calibration images acquired by the detector. The decay image is then normalized (pixel wise by the calibration image) and the resulting pixel values are proportional to the aggregate fluorophore decay time of the illuminated area. These pixel values represent *relative* tissue lifetimes and are referred to as DOCI pixel values. DOCI relies on the fact that the longer lifetime fluorophores generate more signal than shorter lifetime fluorophores when referenced to their steady state fluorescence.

This approach has many key strengths that make it ideal for clinical imaging. First, as discussed above, the computational technique is simple; lifetimes are not calculated, therefore curve fitting is not required. Second, relaxed lifetime calculations allow for longer pulse duration intervals and fall times (> 1 ns); thus, expensive lasers may be replaced with cheap LEDs driven by electronic pulses. The use of LEDs is not only cost-effective but yields additional information regarding the sample when probing with a nanosecond order rise and fall in illumination intensity. This is not apparent when compared with the picosecond-width (or shorter) impulse from a laser. Furthermore, the incoherent light emitted by an LED does not generate interference fringes when

exciting a larger area of interest. The difference in signal between the emission decay of two fluorophores is positively correlated with gate time. In other words, the longer the gate is open during the decay image, the larger the difference signal. In addition, the signal to noise ratio (SNR) significantly increases due to increased signal and decreased measurement noise arising from the integrative properties of the detector. This is in stark contrast to FLIM where gates need to be short to accurately sample the decay time.

3.3 Regarding Standardized Lifetime Measurements

Previous work on the system suggested a linear decay (in contrast to exponential decay) for the LED(s) may produce up to a 40% increase in detected signal (207,211). A simulation of three different possible LED decay functions and the resultant sample fluorescence is depicted in the upper panel of Figure 3-2. These square, linear, and exponential LED decay profiles were convolved with the exponential decay of a simple fluorescent system, the output of which is shown in the lower panel of the same figure. Following the assumption that the phenomenon of fluorescence may be modelled as a linear time-invariant system, both square and exponential decays naturally result in an exponential function for emitted fluorescence. Notably, a linear decay rate convolved with an exponential will result in a reasonably linear function (illustrated in red). In theory, this is the principle permitting standardization of DOCI values with actual fluorescent lifetime values along the linear region of fluorescence decay. However, this result may be affected by fluorophores with multiple conformational states of different lifetimes, and the presence of both multiple (and even orthogonal) fluorescence decay parameters that are common in biologic systems in contrast to reference dyes.

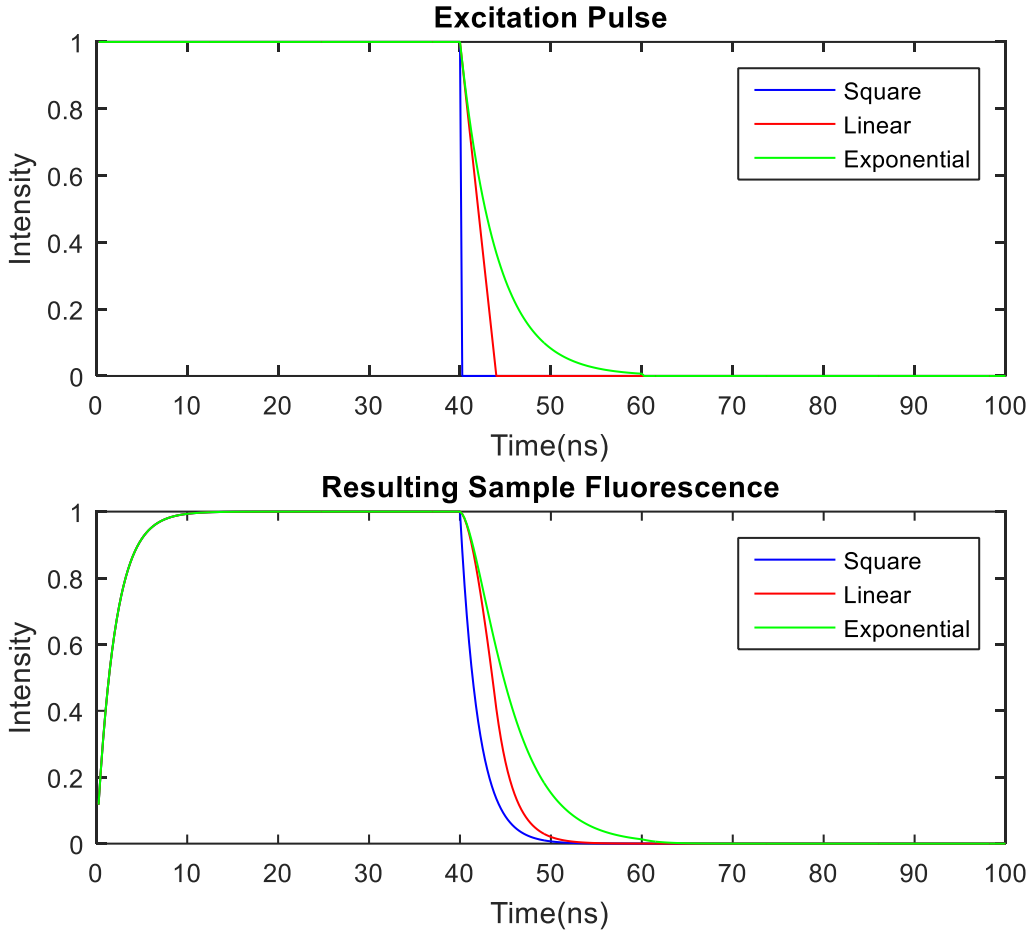

Figure 3-2: Simulated excitatory pulses with square wave, linear shut off, and exponential decay shut off behaviors.
(Lower) Simulated sample fluorescence corresponding to the different pulse behaviors. Illustrated in red, a linear rising and falling excitation pulse will result in a linear measurable fluorescence, theoretically permitting standardization of DOCI ratiometric values to absolute values of fluorescence lifetime. Image adapted with permission of Aidan Pearigan.

CHAPTER 4: PILOT IN-VIVO CLINICAL TRIAL OF DYNAMIC OPTICAL CONTRAST IMAGING AT LARGE FIELD OF VIEW

4.1 Introduction

Head and neck cancer is the sixth most common human cancer, of which 48% are located in the oral cavity(217). The prognosis for patients with oral cavity squamous cell carcinoma (OSCC) is largely determined by the stage of disease at clinical presentation (34,218,219). Patients diagnosed with advanced OSCC have shorter survival times (5-year mortality, 85%, 75%, 47%, and 35% among patients diagnosed as having distant, regional, local, and *in situ* cancer, respectively) (20). Despite medical advances in the management of OSCC, the global incidence, morbidity, and mortality associated with this disease remains relatively unchanged over the past three decades (20,220–222). One of the major factors accounting for these dismal reports is that over 60% of OSCC cases are detected at a late stage (III or IV), when diagnostic evaluation, treatment, and management of complications and recurrences are often lengthy, complex, and burdened by poor outcomes (24,221,223).

The primary surgical management of OSCC (successful when diagnosed at earlier stages) may result in significant functional morbidity; impairments in speech, swallowing, taste, smell, and has the potential to greatly affect the quality of life in these patients (33,34). Unfortunately, surgeons are only equipped with their natural senses of sight and physical touch to localize the contours of a tumor followed by limited frozen section biopsy to establish “clean margins”(2,3,224). Consequently, the determination of tumor margins by palpation and visual inspection has led to recurrence rates of 25-50% (5,6). These challenges substantiate both a clinical need for improved screening and a surgical need for intraoperative guidance to localize tumor margins. In order to address these challenges the aim was to translate the novel optical image-guided technology

(termed dynamic optical contrast imaging- DOCI) into a mobile system suitable for a preliminary in-vivo clinical trial.

4.2 Materials and Methods

4.2.1 System Design

The key elements comprising the system were a nanosecond gated and cooled iCCD camera, motorized filter wheel, imaging lens, UV LED driver circuit, bright field illumination source (for image orientation), and a high voltage pulse generator (HVPG). The system diagram, 3D computer model, and photograph of the intraoperative implementation of the DOCI system are depicted in Figure 4-1.

The illumination system was composed of 6 directional UV-LEDs (Thorlabs LED370E Ultra Bright Deep Violet LED) arranged in two series couplings of three LEDs each in a circular configuration (225). Notably, the model LED370E emits light at wavelengths centered around 375 ± 10 nm. Each light source had a half viewing angle of 19° and emitted 2.5 mW total optical power from 20 mA current. The LED illumination characteristics (i.e., pulse width and peak intensity) were measured using a fast photomultiplier tube and confirmed to be sufficiently linear with minimal ringing following the decay (210). The decay profile of the LED was approximately exponential. Under these operating parameters, the UV illumination delivered the maximum average optical power approximately 4.5 uW at the focal plane and a pulse width of 30ns. A 100 Khz repetition rate of 30 ns pulse width generated a low duty cycle that permitted over driving the LEDs while maintaining thermal stability for long-term use. The energy from 375 nm photons was sufficiently low to avoid any measurable DNA damage under the planned exposure to UV fluorescence [87]. The total exposure of patients to UV radiation was well below the maximum permissible exposure (MPE) limit as defined by the American National Standards Institute (Z136.1-2014).

A high-voltage pulse generator (HVPG), Avtech, operating at 100V peak voltage and 100 kHz repetition rate determined the LED pulse width. The pulse profile of the generator was set at 46ns pulse width with approximately ~1ns rise and fall times. The pulse generator also was attached to the iCCD system to supply a trigger signal for the image capturing process to occur at the correct time around the optical pulse. Imaging delays were adjusted to fit the delay of the circuit allowing for visualization of the rise and steady state at the beginning of the imaging period.

The key elements of the detection arm were the lens, filters, and camera. The nanosecond gated iCCD camera (iStar, Andor technology) captured the intensity images of fluorescence calibration, decay, and background signal. Detailed specifications of the detector are presented in Table 6.The camera was operated with a gate width of 30ns to capture the fluorescence decay. The pulse generator triggered the gating to synchronize the optical illumination with image acquisition. A 50 mm focal length, f/2.8 imaging lens provided a field of view of 6 cm x 6 cm at a standoff of 12 cm, a key feature of this system making it suitable for intraoperative use.

Table 6: Specifications of iCCD Camera.

Parameter	Value
Model	Andor iStar 334t iCCD
Pixel matrix	1024 x 1024
Pixel size	13 um
Max frame rate (full frame)	4.2 FPS
Max frame rate (ROI)	333 FPS
Pixel well depth	100,000 e^-
Lowest read noise	5 e^-
Min. dark current	0.1 e^-/pix/s
Time-resolution	< 2 ns
Cooled Temperature (C^o)	-25

Tissue relative lifetime values typically display a large variation with respect to emission wavelength, and additional contrast and discriminatory power could be generated by analyzing the fluorescence emissions in specific spectral bands (173,174,226). For this purpose, two 6-slot motorized filter wheels (Edmund Optics) were used that in total contained eleven bandpass filters

(Semrock) centered at: 407 nm, 434 nm, 465 nm, 494 nm, 520 nm, 542 nm, 572 nm, 605 nm, 652 nm, 676 nm with ~20 nm bandwidth each, along with a 405nm long-pass UV filter, in order to obtain filtered spectral signal. A second UV rejection filter (Edmund Optics, 405 nm longpass filter) was used in conjunction with the bandpass filters to further reject reflected UV illumination. The system was designed on top of a custom built mobile cart with extending boom suitable for use in the operating room. Standardization with fluorescein and other reference dyes of known lifetime was conducted and is reported separately (210).

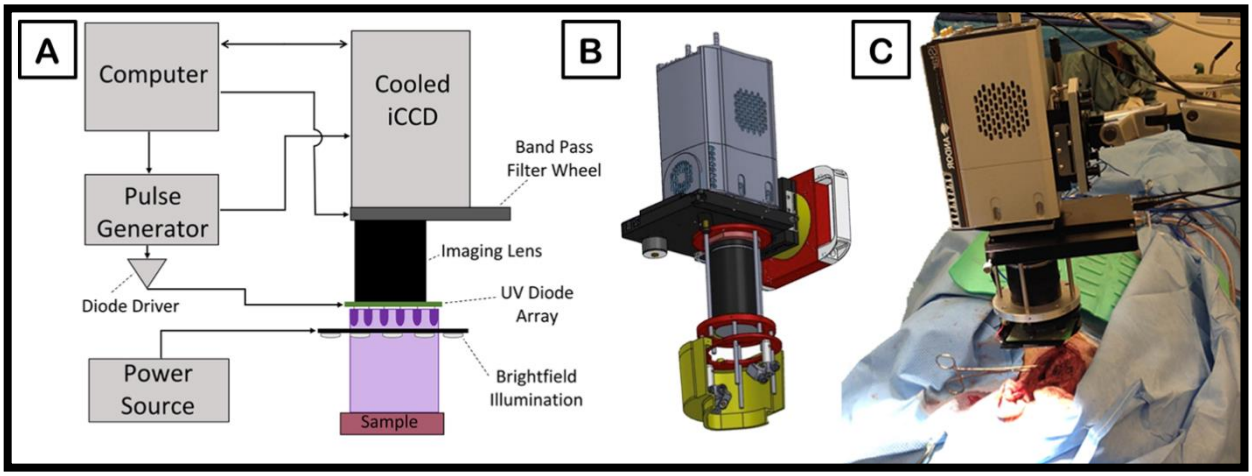

Figure 4-1: Design, model, and application of intraoperative imaging system.
(A) System diagram of key elements of DOCI system with CAD model of system assembly. **(B)** Constructed DOCI system mounted on translational arm in the operating room during procedure. Permission requested from Wolters Kluwer, Pellionisz PA, Badran KW, Grundfest WS, St John MA. Detection of surgical margins in oral cavity cancer: the role of dynamic optical contrast imaging. Curr Opin Otolaryngol Head Neck Surg. 2018 Apr;26(2):102–107.

4.2.2 Study Safety and Approval

Study approval was obtained from the Institutional Review Board of the University of California at Los Angeles. Patients undergoing surgical resection for head and neck SCC, cutaneous melanoma, or cutaneous BCC were identified on a prospective basis. When a patient presented to clinic with a newly diagnosed lesion and surgery was recommended, the patient was asked for voluntary participation in this study to allow imaging with DOCI during their procedure before

routine histopathological analyses. Before surgery the risks were discussed with the patient and an opportunity for questions was provided. All patients provided signed written consent for involvement in the study. All patients received the standard of care and results from the investigational DOCI system were not used to make clinical decisions. This study neither lengthened the standard procedures the patients received nor delayed their care or efficacious treatment.

4.2.3 Patient Population

The demographics for the complete patient population consented for the study are presented in Table 7. In vivo and ex vivo imaging with the DOCI system was conducted for 62 patients over a 12 month period. In total, 207 imaging sessions were conducted, with 154 sessions successfully completed for a 53 unique patient dataset. Locations for DOCI imaging included both clinical and surgical settings of the Head and Neck Department and Surgical Dermatology Department at UCLA Ronald Reagan Medical Center in Los Angeles, California. All head and neck SCC cases were from the department of Head and Neck Surgery where the surgeon performed resection via wide local excision. All but two cases of Melanoma and BCC were from the department of Surgical Dermatology where the surgeon performed Mohs micrographic surgery for tumor resection.

Table 7: Summary of patient demographics and clinical characteristics

Characteristic	Patients enrolled	Imaging completed	Presented in comparative analyses
Total # of subjects	62	53	24
Gender			
Male	46	39	14
Female	16	14	10
Race			
White	50	45	21
Asian	5	3	1
Black	1	1	0
Other/Unknown	6	4	2
Ethnic Category			
Hispanic/Latino	4	4	1
Not Hispanic/Latino	58	49	23
Age, years			
Mean	64.95	65.75	63.25
St. Dev.	15.67	15.19	12.35
Range	23 – 86	28 – 85	35 – 75
≤ 65	28	21	9
> 65	34	32	15
Tumor type			
SCC	37	32	16
BCC	9	8	5
Melanoma	4	3	3
Other / Unknown	12	10	0
Anatomic region (SCC)			
Oral Cavity*	25	23	16
Scalp	6	3	0
Ear	3	3	0
Neck	1	0	0
Other	4	3	0

*Oral cavity included: tongue, lip, gingiva, buccal mucosa, palate, and floor of mouth.

4.2.4 Imaging Protocol

Following patient consent, DOCI imaging was conducted with the mobile system (detailed in 4.2.1). First, the clinician demarcated the area of interest and a DSLR image was acquired for purposes of future orientation. Next, the patient chair or operating table was lowered and the extensible arm of the DOCI system was oriented above the area of interest. Two 1mW red laser

pointers attached to the edges of the imaging lens converged into a single spot at exactly the focal length of the imaging lens. This permitted quick adjustment to ensure correct focus was achieved between the DOCI system and the area of interest. The two low-power lasers were then switched off and the room lights were asked to be switched off. The DOCI imaging sequence was then initiated on the system controlling computer. The first filter wheel contained red, green, and blue filters in order to recreate an intensity image for future comparison together with the DSLR image. Next, bandpass filters automatically rotated position at 10 second intervals per filter position. Once all images using the first filter wheel were acquired, a second filter wheel was switched into position in about 20 seconds time. Thus, the complete duration of the image acquisition session was about 2 minutes. Both intensity and calibration images were saved to the microscope controlling computer and processed after the surgery was completed (detailed in 4.2.6). If authorized by the lead clinician, this imaging process was repeated for the tumor bed (in vivo) immediately following resection and also for the excised tissue specimen (ex vivo) within about 15 minutes to at most 2 hours following surgical tissue resection. The DOCI system was used with the same settings and imaging protocol in both clinical and surgical environments.

4.2.5 Ex-Vivo Tissue Confirmation With Histology

The process of ex-vivo tissue inking and registration was continued from our previous works and is demonstrated in Figure 4-2 (210). First a DSLR image is taken of the designated area for purposes of future orientation. Following surgical resection both a grayscale intensity photo and the multi-spectral relative lifetime images are acquired using the same detector. A surgical marking pen is then used to annotate lines on the sample based on observable morphological features. These lines are inked in multi-color dyes, and another DSLR photo is obtained, once again for future reference. The inked tissue is then processed according to standard protocol in surgical pathology, and notes by pathologist or technician are added to the patient chart regarding

the histology slides that correspond to each inked line. Thus, the obtained histology serves as the ground truth to confirm DOCI contrast.

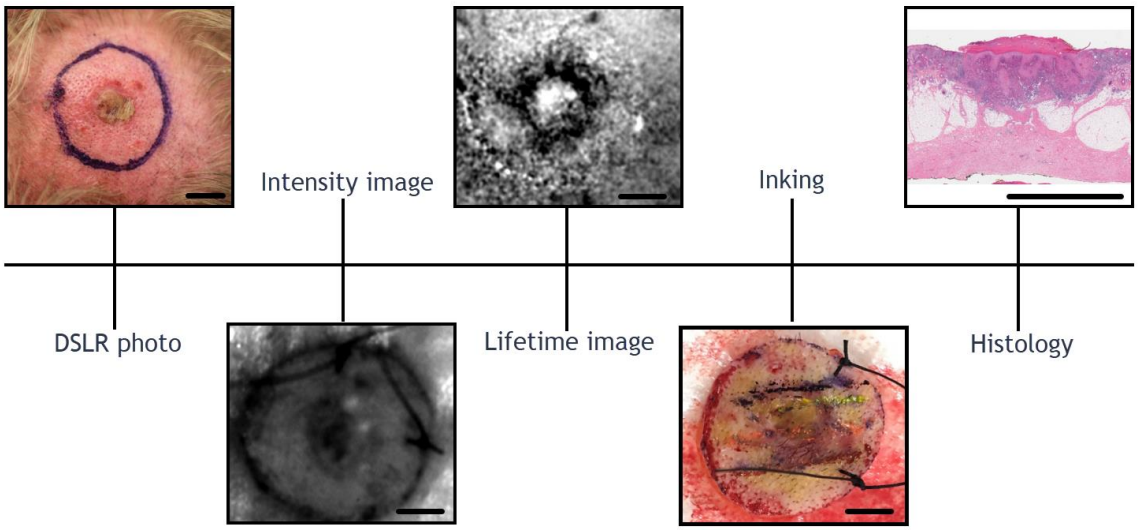

Figure 4-2: Image registration protocol.
Scale bars: 1cm.

4.2.6 Statistical Image Analyses

The algorithm and explanation behind the creation of the primary DOCI image are detailed in section 3.1. In brief, three intensity images were acquired per filter for a total of 33 individual images per imaging session. For each wavelength, the background image was subtracted from both the calibration and decay frames. Both images were converted to double format and the decay image was then divided element-wise by the calibration image to produce the raw DOCI image. Any value exceeding the maximum threshold of one was set to the maximum value of one. Any value below zero or not a number was set to the minimum value of zero. The ***stretchlim()*** function was utilized to stretch the intensity histogram of the raw DOCI image to the 2nd and 98th percentile image upper and lower thresholds in order to increase available image contrast. This was done even if the percentage of saturated pixels was zero. Contrast stretching is a linear normalization that stretches the original interval of pixel intensities of an image and fits the

interval to image maximum and minimum values, thus maximizing the entire dynamic range in a linear and reproducible fashion. This is in opposition to histogram stretching, which is sensitive to outliers, and often results in images that have poor contrast without any percent thresholding. It is usually better to accept some small amount of visual saturation, in order to produce more contrast between pixel values at the extreme values. The normalized and contrast stretched grayscale image was then used for quantitative statistical comparison.

For qualitative comparison, a two-dimensional (7x7) median filter was applied. An advantage of the median filter is that the modulation of signals oscillating over a period less than the width of the median window may be reduced. At the same time, the gray values of constant or monotonically increasing signals on a scale larger than the window size may be preserved. In other words, the variance of additive noise is reduced while edge structure is conserved(227). Thus, this filter removed gaussian noise in the image and preserved edges to a greater degree than using an average filter. A Jet colormap was then applied in order to permit discrimination by color and not just pixel intensity. This image processing and computation was performed in batches and automated with Matlab (Mathworks 2019b).

For In Vivo Imaging of SCC and preneoplastic lesions in the oral cavity, acquired images were segmented into 80x80 pixel regions of interest. This was accomplished by drawing manually delineated region of interest masks based on macroscopic appearance and histopathological correlation with the instruction of the Head and Neck clinician supervising the study and a pathologist from the department of Surgical Pathology. The masks were overlaid on to the corresponding fluorescence images and applied to the statistical processing of the DOCI fluorescence images. For each patient, matched pairs of ROI’s were generated of either normal, lichen planus, leukoplakia or squamous cell carcinoma, compared to an adjacent normal appearing mucosal region of the oral cavity. For in vivo SCC comparison the lower lip was used

in two cases whereas all other matched pairs were from the tongue. The sample distribution consisted of five normal, five lichen planus, three leukoplakia, and eight SCC matched pairs of ROIs. Within a matched pair of ROIs of one patient, the mean intensity of aggregate pixel populations with pooled variance was calculated using Matlab and used for tissue region comparison. The absolute difference between two ROIs was measured and evaluated statistically, thus both a decrease or increase in signal intensity were equally represented in terms of the positive difference from adjacent normal tissue. Segmentation and ROI analyses were conducted with ImageJ (version 1.9.0_112) using the ROI tool with data organized using Matlab (Mathworks 2019b).

Pixel populations of the normalized and contrast stretched DOCI image were compared in order to quantify relative differences between tissue types across unique spectral bands of detection. Nonparametric test of the aggregate pixel populations between tissue types was conducted with GraphPad software (Graphpad Software, San Diego, CA). The non-parametric Kruskal-Wallis test was used as a more stringent alternative to a one-way ANOVA with subsequent comparisons evaluated using Dunn's multiple comparison test with alpha set at 0.05. All data expressed as mean ± the standard error of the mean (SEM).

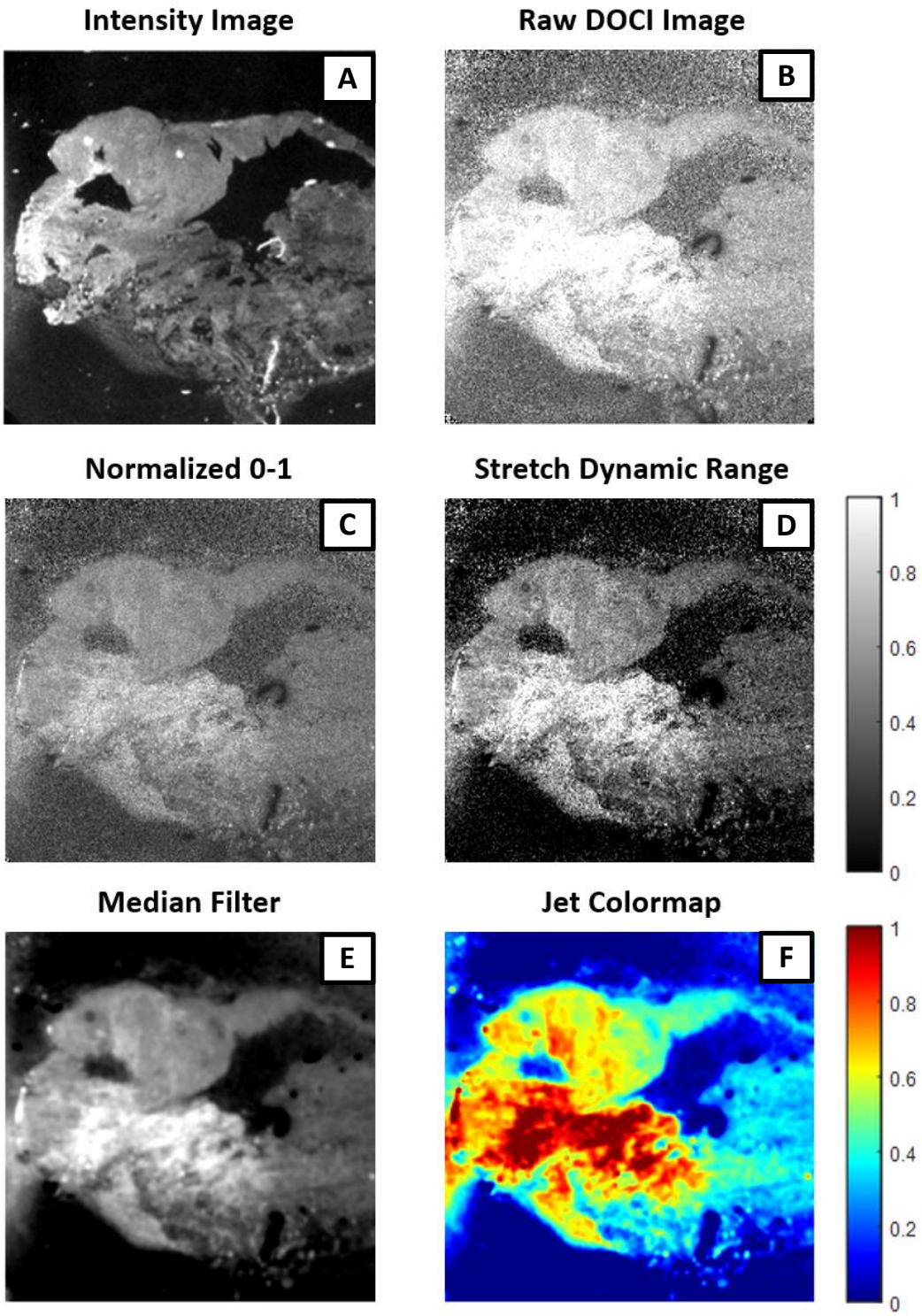

Figure 4-3: Image processing from acquisition to display.
(A) intensity image **(B)** Calibration image. **(C)** DOCI image following division of decay image by steady-state image. **(D)** Threshold and scaling of data. **(E)** 7x7 2Dmedian filter. **(F)** Jet colormap. Resected SCC from floor of mouth (procured by Shan Huang for analyses).

4.3 Results

4.3.1 Application Of DOCI For Premalignant And Malignant Oral Lesions

In vivo results from both Head and Neck Surgery and Surgical Dermatology are summarized in Table 7. The cohort of patients enrolled in the study had a mean age of 64.95 years, were predominantly white (50/62) with about three times more males than females (46:16). The age ranged from 23 – 86 years with 34 patients over age 65 and 28 patients of age 65 or less. Concerning SCC from the oral cavity, 25 patients that presented to the Head and Neck Surgery department signed consent to participate in the study and 23 completed the imaging session without interruption. An imaging session was considered completed if all 33 individual images were successfully acquired and recorded by the imaging system. In one case the imaging system ran out of power and the session needed to be aborted. In the other case a medical emergency prevented image acquisition. Of the 23 cases there were 6 patients with SCC of the lateral tongue and 2 with SCC of the lower lip. Preneoplastic lesions (leukoplakia, N = 3) and inflammatory lesions (lichen planus, N = 5) all occurred on the tongue. The sample size for the normal population was (N = 5) patients. In total, these three groups amounted to 24 patients with mean age 63.25 years, ranging from 35 to 75. The majority of patients were white (21/24) and there were more males than females (14:10). Examples of each lesion, ROI pixel areas compared, and DOCI images of the respective area, are presented in Figure 4-4. In the figure (A,D) The second and third column of panels are horizontally flipped for the purpose of consistent orientation between all images. Also in the figure for panel (B) and (C) a DSLR image is substituted for the basic intensity image of tissue since the original frames were obscured by glare from high-intensity clinical spotlights.

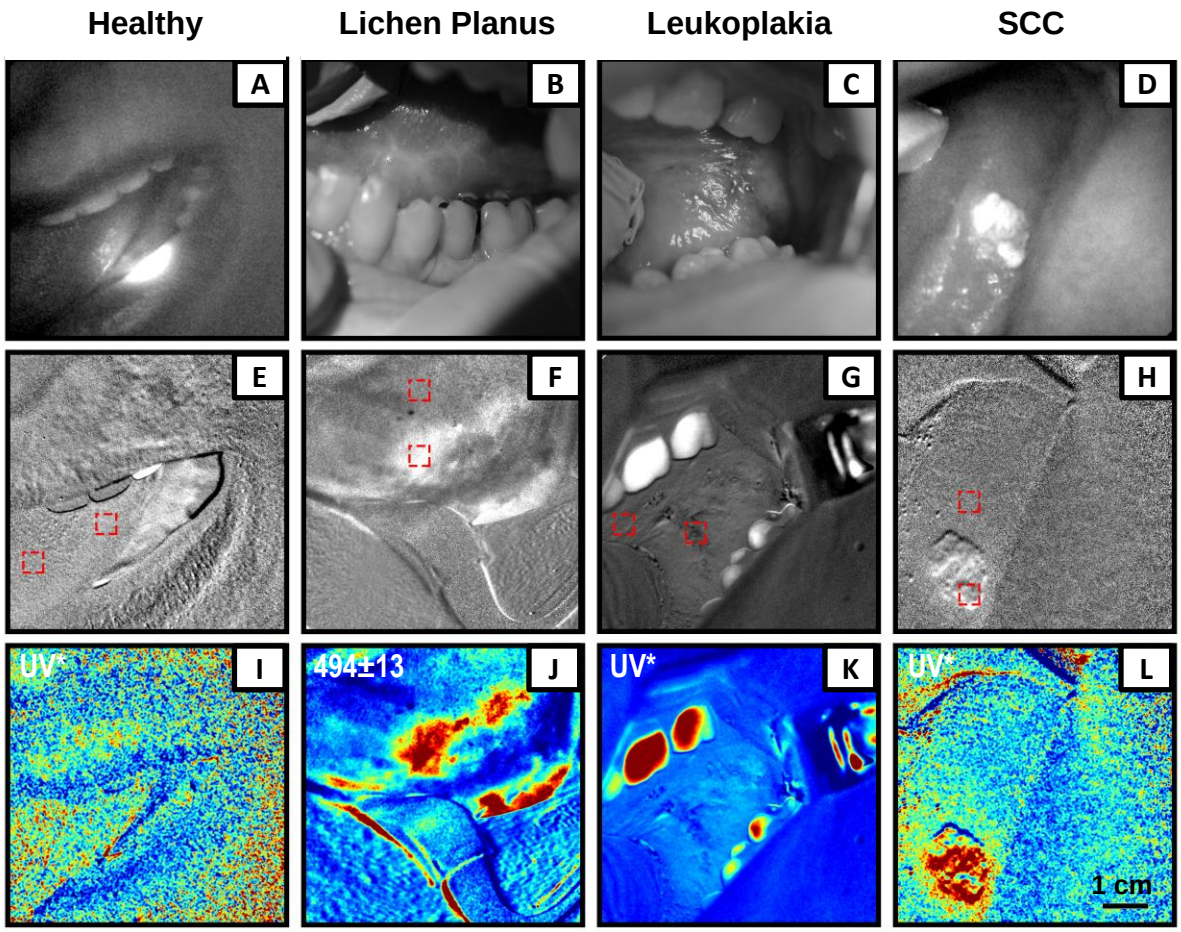

Figure 4-4: Intensity, DOCI, and ROI boundaries for intensity and relative lifetime comparison of patients with lichen planus, leukoplakia, SCC, and visually healthy superficial mucosa of the tongue.
(A-D) Steady-state intensity images of the region of interest; **(E-H)** ROIs used between target and adjacent normal tissue; **(I-L)** Spectral wavelength with largest difference between paired regions of interest;. UV* is a long-pass 405nm filter. Scale bar, 1cm.

Statistical analyses comparing the median ROI values in Lichen Planus/Leukoplakia/SCC vs. adjacent "healthy" and visually normal tissue indicated that spectral features of median relative autofluorescence lifetime showed statistically significant distributions between certain spectral channels. Detailed in Table 8, the median pixel value for was significantly different for normal vs. SCC in two channels (676nm and UV longpass) and normal vs. leukoplakia in one channel (UV longpass). Normal vs. Leukoplakia was trending towards significance ($p = 0.06$) in the 676nm spectral channel. Normal vs. Lichen planus was also trending towards significance ($p = 0.08$) at

the 494 nm channel. Contrast appeared almost entirely in the 494nm spectral band, and all spectral frames are included for review in Appendix A2. While not statistically analyzed, qualitative contrast remained upon imaging the tissue area ex vivo and was absent on the medial/deep surface (Appendix A2). In vivo, the median pixel population difference between lichen planus vs. normal was marginally significant at (0.08) while SCC vs. normal was not significantly different ($p > 0.99$) in the 494 nm spectral channel. These differences in DOCI pixel contrast are graphically illustrated across all spectral channels in Figure 4-5. Lesions from the scalp, ear, neck, deep oral cavity and other areas of the face did not consistently yield enough fluorescent signal for comparative studies.

Relative fluorescence lifetime spectroscopy of in vivo tissue using dynamic optical contrast imaging

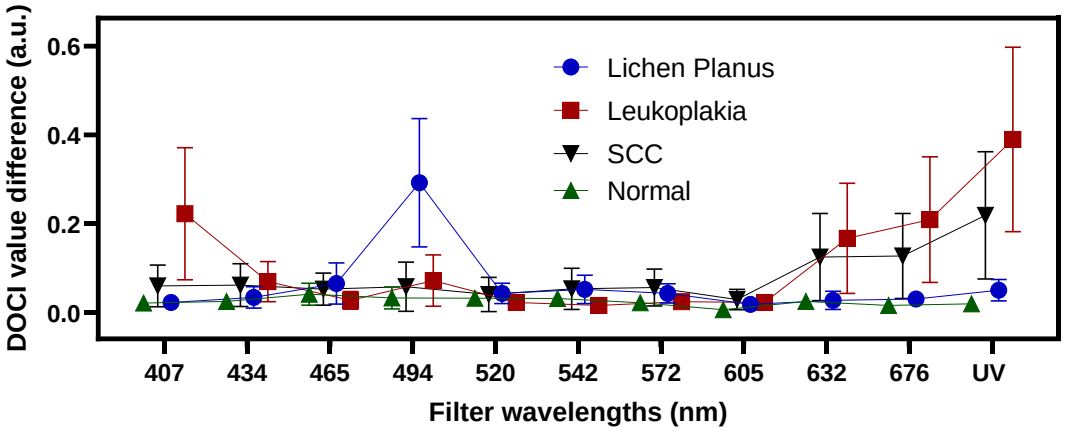

Figure 4-5: Relative fluorescence lifetime spectroscopy difference in oral cavity. Scale bars indicate SEM.

Table 8: Statistical analysis for in vivo spectrometry.

Kruskal-Wallis	0.15	0.29	0.81	0.03	0.72	0.50	0.40	0.37	0.06	0.008	<.001
Normal v. Lichen Planus	>0.99	>0.99	>0.99	0.08	>0.99	>0.99	>0.99	>0.99	>0.99	>0.99	>0.99
Normal v. Leukoplakia	0.25	0.97	>0.99	>0.99	>0.99	>0.99	>0.99	>0.99	0.31	0.06	0.003
Normal v. SCC	>0.99	0.88	>0.99	>0.99	>0.99	>0.99	0.71	>0.99	0.35	0.02	0.008
Lichen Planus v. Leukoplakia	0.25	>0.99	>0.99	0.36	>0.99	0.78	>0.99	>0.99	0.31	0.40	0.08
Lichen Planus v. SCC	>0.99	>0.99	>0.99	0.04	>0.99	>0.99	>0.99	>0.99	0.35	0.31	0.30
Leukoplakia v. SCC	0.95	>0.99	>0.99	>0.99	>0.99	>0.99	>0.99	>0.99	>0.99	>0.99	>0.99
Spectral band (nm)	**407**	**434**	**465**	**494**	**520**	**542**	**572**	**605**	**632**	**676**	***UV**

P-value for Kruskal-Wallis test displayed in top row. Specific tests performed per condition with Dunn's multiple comparison. Significant results are highlighted in red.
*UV is a long-pass filter.

4.3.2 Application Of DOCI In Mohs Micrographic Surgery For Cutaneous Malignant Melanoma And BCC

In vivo results from both Head and Neck Surgery and Surgical Dermatology are summarized in Table 7. Concerning cutaneous BCC there were 6 patients that received Mohs micrographic surgery and 3 that received wide-local excision. Of the 3 that received wide local excision there were 2 imaging sessions that were not completed and 1 that was not in focus at the region of interest during acquisition. Of the 6 that received Mohs surgery all 6 were completed but one case was not included in the analyses because the room lights needed to be turned on midway through the imaging session. The anatomic locations of these 5 included cases were: 3 scalp, 1 arm, 1 leg. An example of a BCC lesion imaged in vivo with accompanying ex vivo section and histology is displayed in Figure 4-6. Regarding cutaneous MM there were 4 patients imaged in the department of Head and Neck Surgery and 3 imaging sessions were completed. All 3 anatomic locations were from the scalp.

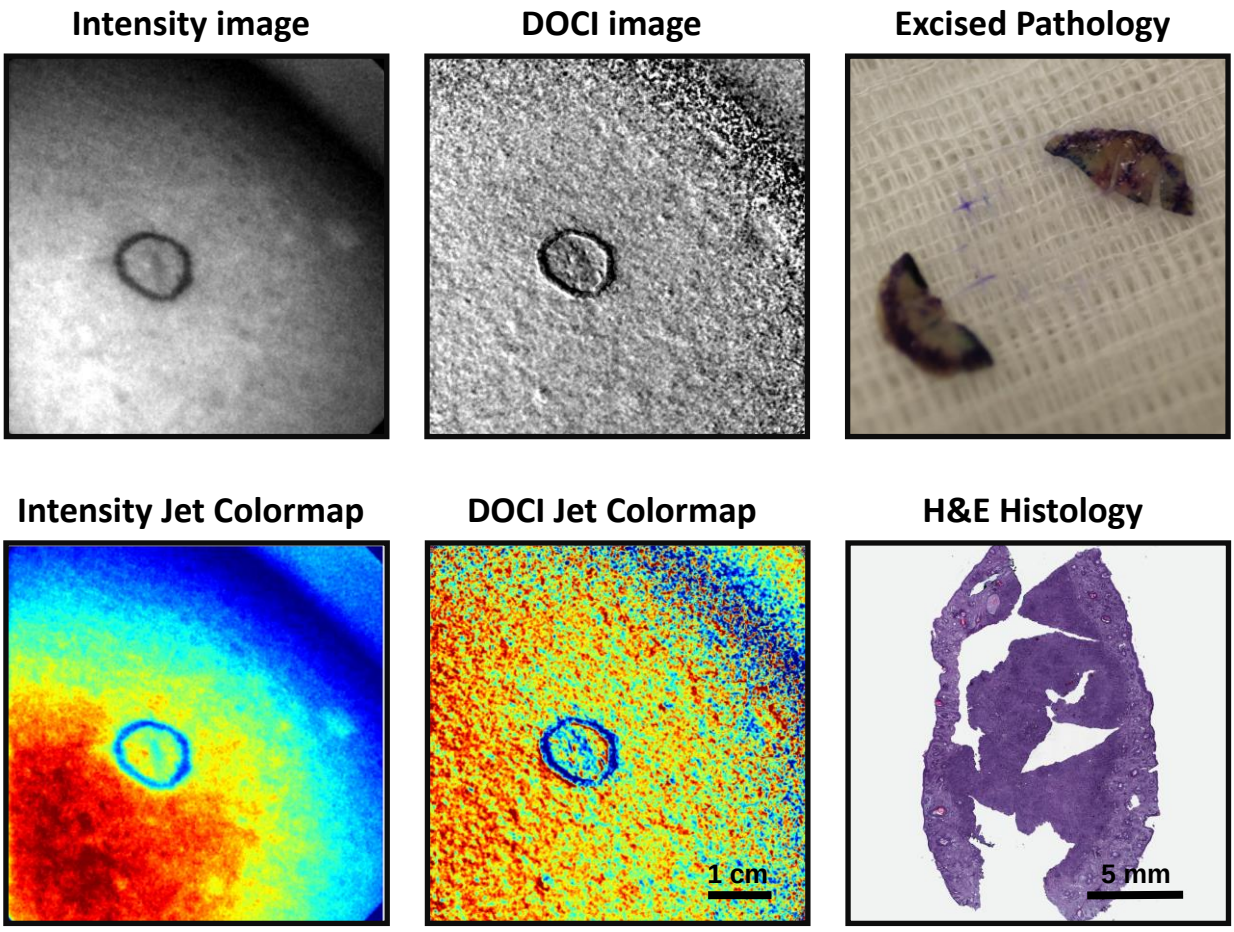

Figure 4-6: BCC encircled before Mohs micrographic surgery.
Top left, Intensity image of BCC in clinic before resection. Top middle, DOCI image of same region as top left. Bottom left and bottom middle are the same regions as above with Jet colormaps. Top right is the resected BCC. Bottom right is histology consistent with diagnosis of BCC. FOV is 6x6 cm. Scale bar on Histology is 0.5cm

Statistical analyses comparing the median ROI values in BCC/Melanoma vs. adjacent normal tissue indicated that spectral features of median relative autofluorescence lifetime significantly differed in their distributions between certain spectral channels. Detailed in Table 9, the median pixel value was significantly different for normal vs. BCC in two channels (542 nm and UV longpass). Relative lifetimes were consistently smaller for areas of BCC at spectral bands 434-520nm and typically appeared higher at 632, 676, and UV longpass bands. Additional complete image sets demonstrating results are presented in Appendix A4.

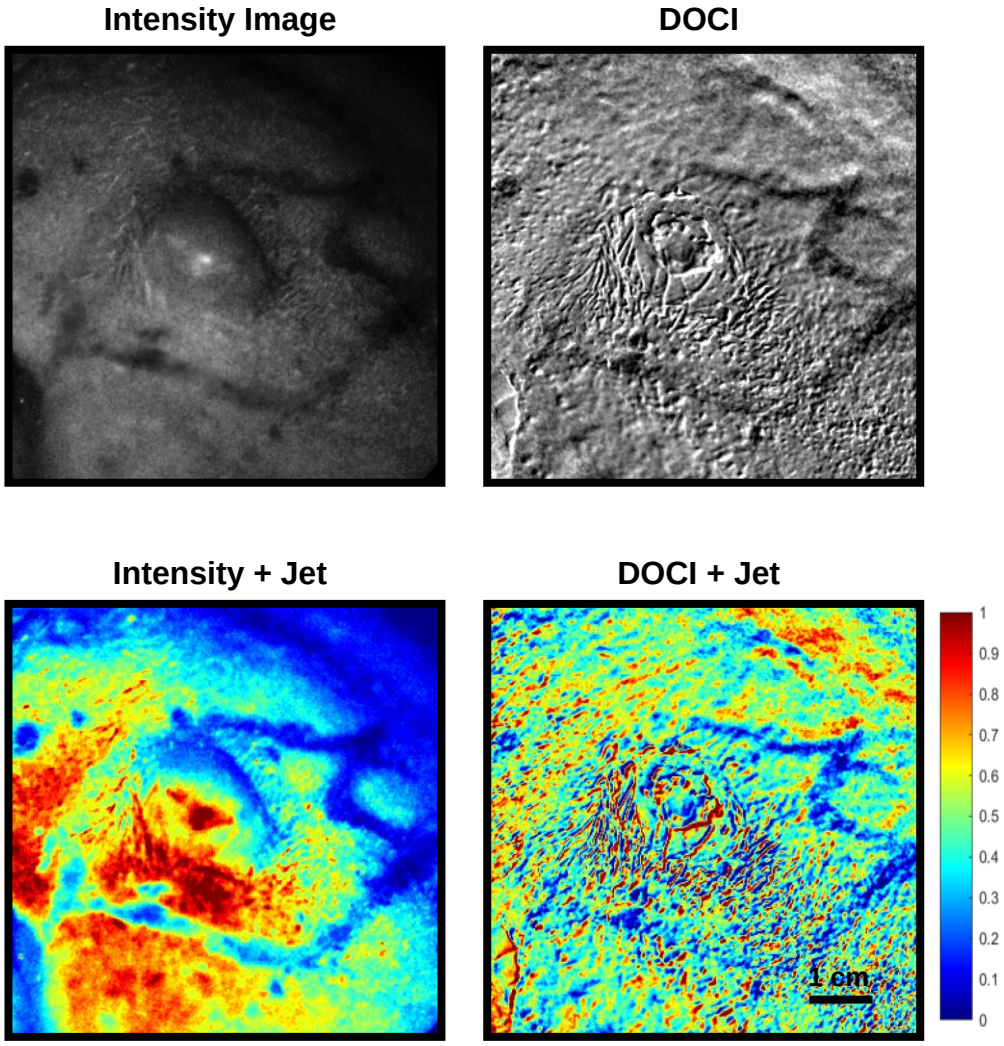

Figure 4-7: Intensity and Relative Lifetime Images of Cutaneous Malignant Melanoma.

There was no consistent relationship between MM relative lifetime values and areas of normal surrounding skin, and MM was not statistically significantly different in any recorded spectral channel. The sample size of the normal population was (N = 5). Notably, more contrast was visualized in resected tissue with Melanoma (presented in Appendix A1) than under in vivo conditions, which was not observed for SCC nor BCC. These differences in DOCI pixel contrast between relative regions of interest for BCC, Malignant Melanoma, and adjacent normal tissue are graphically illustrated across all obtained spectral channels in Figure 4-8.

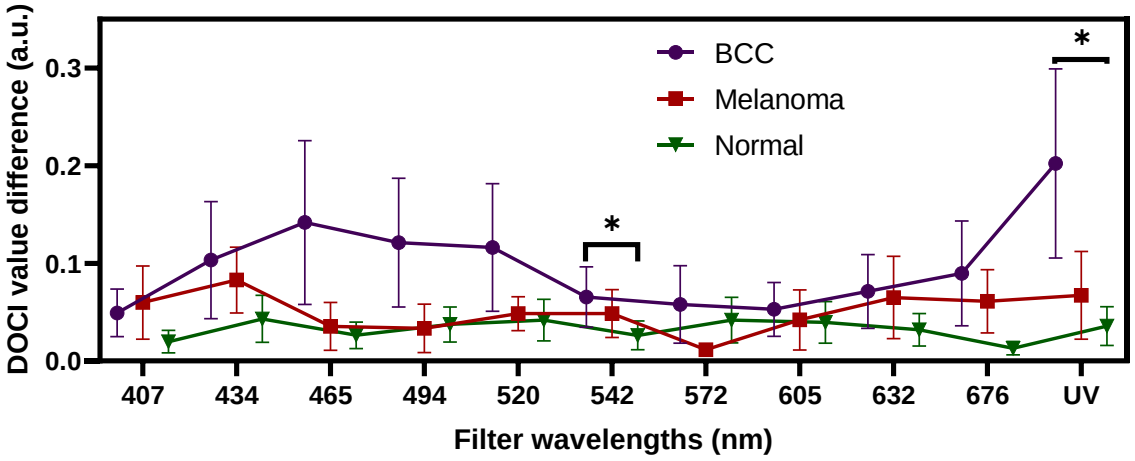

Figure 4-8: DOCI values for cutaneous BCC and melanoma compared to adjacent normal tissue.
Scale bars: SEM

Table 9: Statistical analysis outside oral cavity.

Kruskal-Wallis	0.17	0.29	0.22	0.16	0.11	0.04	0.32	0.90	0.45	0.16	0.003
Normal v. BCC	0.18	0.33	0.18	0.21	0.08	0.03	>0.99	>0.99	0.45	0.25	0.007
Normal v. Melanoma	0.27	0.35	>0.99	>0.99	>0.99	0.35	0.24	>0.99	0.65	0.17	0.67
Spectral band (nm)	**407**	**434**	**465**	**494**	**520**	**542**	**572**	**605**	**632**	**676**	***UV**

Exact p-value for Kruskal-Wallis multiple comparisons test displayed in top row. Specific tests performed per condition with Dunn's multiple comparison with p-values reported adjusted for multiple comparisons. Significant results are highlighted in red.
*UV is a long-pass filter.

4.4 Discussion

4.4.1 In Vivo Imaging Of SCC And Oral Cancer Screening

Using a novel relative lifetime imaging system (228) wide-field relative lifetime maps were created from unstained tissue in vivo. Oral SCC lesions were successfully imaged in 8 patients, leukoplakia in 3 patients, and lichen planus in 5 patients, yielding statistically significant information from different spectral bands. The exceptionally large field of view (6x6 cm) and short acquisition time (10 seconds per spectral channel) enabled quick and simple in-vivo imaging in both the clinical and surgical settings.

The multispectral relative lifetime images were processed offline to generate widefield maps of endogenous fluorescence lifetime. Notably, statistical analysis revealed that normal tissue could reproducibly be differentiated from lichen planus, leukoplakia, and SCC independently at the wavelengths of 494, 676, and 405nm+ (UV longpass). The tongue was the most common site for intraoral carcinoma in our study and our small sample population accurately reflected worldwide incidence where the tongue statistically accounts for around 40% of all cases in the oral cavity proper.

The LED-based light source illuminated tissue at 375nm and the changes observed in the 407nm band for Leukoplakia may possibly be related to collagen and or elastin. Interestingly however, breakdown of collagen crosslinks in connective tissue and an overall decrease in lifetime were expected in leukoplakia and SCC (~400nm range), yet such a change was not observed in both conditions. While an increase in both epithelial thickness and tissue optical scattering were expected in dysplastic and cancerous change it is possible that these differences are more pronounced with intensity as opposed to lifetime measurements. The detected fluorescence at

the longer wavelengths of 632 and 676nm may be from porphyrins which would be present in increased amounts in neoplastic tissue.

Eight spectral bands did not provide statistically significant information regarding the studied patient groups. Lifetime changes from NADH and FAD were expected near 450 and 500nm and their absence raises questions concerning the overall optical power of the system. If continued studies confirm this finding then there will be a possibility to eliminate these filters and thus reduce the overall time that is required to complete an imaging session. It is also possible that unique versions of the system may be created that are specific to a particular clinical application. Considering the distribution of paired normal tissues the variance is much lower in Figure 4-5 in comparison to Figure 4-8. This may be due to additional scattering and attenuation by the presence of a keratinized layer in cutaneous epidermal tissue compared to intraoral mucosa.

Additional studies will be necessary to confirm the unique change in fluorescence lifetime for lichen planus at the 494nm band. These early results, however, suggest a unique feature that could possibly serve as a novel fluorescence lifetime biomarker to differentiate a commonly misdiagnosed benign condition. Thus, this preliminary clinical study provides promising results concerning the use of biochemical and metabolic autofluorescence biomarkers of oral precancer and cancer for potential patient screening.

The significant majority of patients with HNC present with SCC of the oral cavity, and this finding was confirmed in the first clinical trial with the imaging system, in which 25/37 (67.6 %) of patients with SCC had lesions in the oral cavity. Unfortunately, only 8/23 (34.5 %) of the completed imaging sessions yielded enough contrast to resolve any morphological structure in the DOCI image. A likely cause of the low to no signal could have been the inability of light from the large 4” diameter circular array to illuminate the inside of the oral cavity and reach the fluorophores of interest. This large diameter was originally

designed to accommodate the detection zoom lens and uniformly illuminate the sample at the focal plane of the lens. This issue presented not only when imaging inside the oral cavity but also when attempting to image the parathyroid glands. A wider entrance angle could theoretically be achieved additional surgical resection but that solution would be counterproductive to the goals of minimally invasive surgery. Given the promising results from clinical application of the system towards preneoplastic and neoplastic lesions of the tongue, an endoscopic attachment was simulated and evaluated as a possible option (detailed in 9.2.1).

4.4.2 In Vivo Imaging Of Malignant Melanoma And BCC

Autofluorescence spectral measurements were made on different cutaneous neoplastic lesions, namely basal cell carcinoma and malignant melanoma. The complex geometry and surface irregularities in both tumors and resected specimens of SCC quickly proved a challenge for recording accurate lifetime measurements, especially considering the absence of any exogenously used contrast material. In order to mitigate this issue and reduce the overall size of the targeted area and the variation in surface contour, a subset of patients were imaged in the Surgical Dermatology suite at UCLA where patients underwent Mohs micrographic surgery. Unintentionally and by chance, nearly all of the patients imaged with the DOCI system at this department presented with BCC, making it a logical grouping of cases for comparison. The prototype DOCI system permitted statistically significant tissue discrimination between BCC and adjacent healthy normal tissue between the averaged values across all samples tested. The 465, 494, and 520nm bands yielded a considerably different lifetime between the majority of samples that may warrant a higher powered study with a larger sample size. At 434-520nm band BCC showed consistently smaller relative lifetime values that are in agreement with previously reported results.(165) In this study the lifetimes at these bands (across all samples) were either not statistically significant because the sample size was too small, or because the expected mean lifetime difference (32 – 186 ps shorter than paired normal regions) was too short to resolve.

Considering that the expected difference was under half a nanosecond it was very encouraging in terms of the temporal resolution of the system to see that the results were trending towards significance and were significant for the 542nm band.

These results suggest that application of this new technology towards Mohs micrographic surgery seems very promising. At 375nm, the tissue penetrance of incident light is under 100um (182). This limitation seems best suited for Mohs surgery where cutaneous tumors are removed by repeated resection of thin slices. Ideally, in the future DOCI may provide valuable information to the Mohs surgeon during the operation and possibly reduce the total duration and cost of the procedure. From our results of imaging the tumor bed an issue encountered were the image artifacts due to wound cauterization and reduced signal due to the absorbing effects of blood. Possible solutions for future experiments may be irrigation of the surgical bed and local epinephrine injection for purpose of blood vessel vasoconstriction.

The lifetime maps appeared to provide greater visual contrast than the intensity maps but actually less morphological information than intensity images. This was especially apparent in the relative lifetime maps generated for cutaneous malignant melanoma. It is well known that solar elastosis increases with age but this may not have been a factor since the mean age for patients in the melanoma and BCC cohorts were similar at (73.3) and (70.6), respectively. While the results are confounded by surgical approach there may be additional factors contributing to the minimal contrast observed for MM targets imaged. Foremost, the early diagnosis of malignant melanoma has been described as the most challenging application in dermatology(229). Since both melanin and red blood cells are strong UV absorbers, one possible hypothesis is that increased blood vessel recruitment and melanocyte production are strongly attenuating the incident light. Melanoma was the only disease where DOCI contrast actually increased ex vivo (Appendix A1)

This finding may have some relation to the blood that drained from the tumor nodule during excision.

In literature a greater fluorescence lifetime contrast has been reported between BCC and adjacent normal tissue for the nodular and superficial variants of BCC compared to infiltrative, micronodular, and mixed subtypes (165). This finding may be interesting to validate and pursue with DOCI imaging in future experiments

4.5 Conclusion

These results are the first examples of in-vivo tissue differentiation based on relative lifetime contrast at 6x6cm FOV. In future applications, this feature may be exploited for the choice of biopsy site and possibly reduce the limitations associated with random sampling.

Relative lifetime images from different tissues also revealed unique spectral features for individual states of disease before tissue biopsy. The unique spectral signatures may be used for detection of presence of pathological alterations in the investigated tissues. The absence of image contrast for malignant melanoma in-vivo and ex-vivo SCC also provide valuable information regarding suggested inclusion criteria for a larger scale clinical study. For malignant melanoma, it may be more feasible to use DOCI for imaging margins on ex-vivo specimens while the opposite may hold true for larger resections of SCC.

This preliminary study yields encouraging results concerning the translation of the technique towards the new clinical application of Mohs micrographic surgery that is worthy of further study with a lens of increased magnification. Since the procedure is conducted in a smaller patient room it is much more feasible to completely darken the room during imaging, thus significantly reducing

background noise in acquired images. In addition, the repeated thin sections obtained by the surgeon reduce the limitations posed by the shallow tissue penetration depth of the DOCI system. An image-guided technique with histologic resolution may have significant potential in reducing the time spent waiting on frozen sections.

CHAPTER 5: EX-VIVO HNSCC IDENTIFICATION WITH IMPROVED SYSTEM

5.1 Introduction

Oral and head and neck squamous cell carcinomas (OSCCs) are debilitating diseases for which a patient's prognosis heavily depends on complete tumor resection. The establishment of margin-free resection, however, is often difficult given the devastating side effects of aggressive surgery and the anatomic proximity to vital structures. Positive margin status is associated with significantly decreased survival (13,230). Currently, it is the surgeon's fingers that determine resection margins by palpating the edges of the tumor. Accuracy varies widely based on the experience of the surgeon and the location and type of tumor. Prior efforts to use a variety of optical and ultrasonic techniques for margin detection have not succeeded clinically for several reasons. These methods include standard autofluorescence, Raman spectroscopy, diffuse reflectance, and infrared imaging (231–237). While promising results have been reported, these techniques generally suffer from a sensitivity to imaging confounders encountered *in vivo* and in intraoperative settings. In our prior works, DOCI has been used to generate statistically significant contrast between tumor and surrounding normal tissue in resected tissue (ex vivo) from OSCC patients (228,238,239).Following the addition of a redesigned circuit board, higher power LED, and numerous optimized system components the performance of the system was evaluated through *ex vivo* study of resected OSCC tissues. In this study we made several improvements to our system and conducted a higher resolution study into the lifetime response of studied tissue to our unique LED pulse profile.

5.2 Materials and Methods

5.2.1 Human Tissue Collection And IRB Approval

Study Design: In this pilot study, patients undergoing surgical resection for primary HNSCC were identified on a prospective basis at UCLA medical center. When surgery was recommended, the patient was asked for voluntary participation to allow DOCI imaging on resected tissue following their operation. All patients provided signed written consent for study involvement. We did not lengthen the standard procedures patients received nor delay care for efficacious treatment. Study approval was obtained by the institutional review board of the University of California at Los Angeles.

5.2.2 System Design And Verification

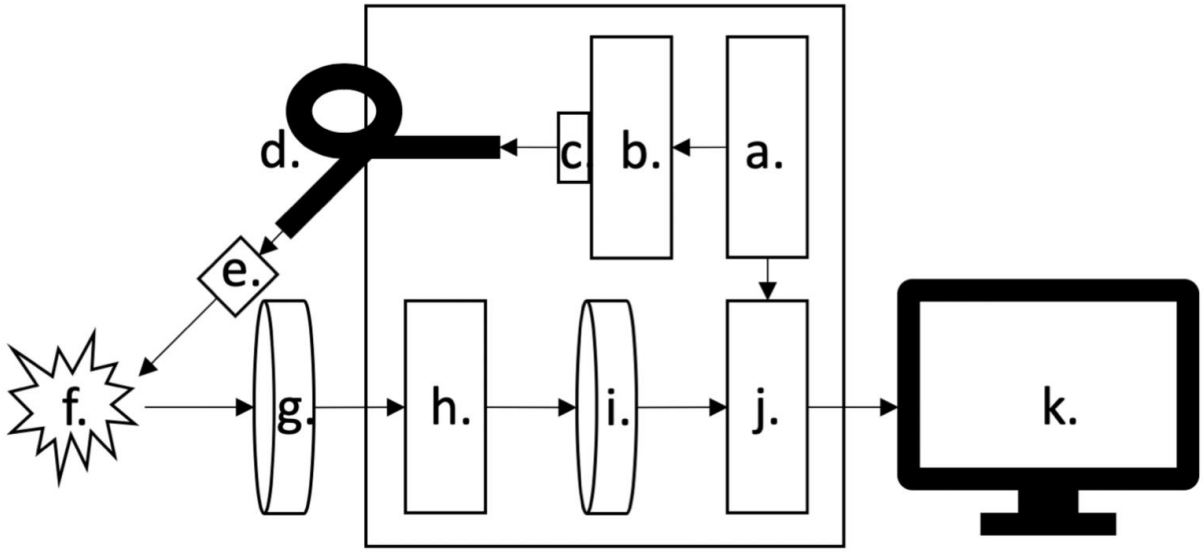

Figure 5-1: Imaging system components.
(a) Dual output function generator **(b)** LED driver board **(c)** 365nm LED **(d)** light guide **(e)** collimating lens **(f)** excitation of endogenous fluorophores in tissue **(g)** UV filter **(h)**zoom lens **(i)** motorized filter wheel with bandpass filters **(j)** iCCD camera **(k)** computer controller and display.

Illumination Source

One of the key elements of the presented technique is the reliance on light emitting diodes LEDs for illumination. The LED is a semiconductor diode that produces light in a non-coherent and divergent fashion. Overall, the two main areas of interest were (1) increasing the radiant flux for exciting tissue fluorophores and (2) driving the LED with a suitable pulse to achieve nanosecond order rise and fall times.

In order to increase available photons from fluorescence the amount of incident light upon tissue needed to be increased. Recent advances in the availability of higher power UV-A emitting LEDs permitted an increase in radiometric flux of over two orders of magnitude compared to the previous source. The detailed specifications of the original Thorlabs 370E model and the new LED from Luminus are presented in Table 10.

Table 10: Specification of illuminating LED diode.

Parameters*	Thorlabs 370E	Luminus SST-10-UV-A130-E365-00
Peak Wavelength Range (nm)	375 (±10)	370 (±5)
DC Forward Current (mA)	30	1000
Radiometric Flux (mW)	2.5 (20 mA)	875
FWHM at 50% of Φ (nm)	10	10
Viewing angle (degrees)	38	130

*Manufacturer quoted specifications.

Previously conducted experiments determined that an increased voltage from the pulse generator to the LED above a threshold caused a secondary peak in later decay. The appearance of electrical reflections in the noise floor served as the previous limit for the maximum voltage used to drive the LEDs. Design constraints for the new circuit board included under 10% amplitude variance in steady-state at peak intensity, ideally linear LED decay with 90-10% change within about 5 nanoseconds. Ideally linear rise time was a secondary priority.

Illumination at focal plane

The power of incident illumination was test at the focal plane of the detection lens with using a portable silicon-based power meter (Edmund Optics). Measurements for each cm^2 of the two by two cm field of view are presented in Figure 5-2. The average power per square cm was 2.63mW. By normalizing results, measurements may be taken from all parts of the field of view without concern for inhomogeneity in illumination profile. This was demonstrated through acquisition of signal from 16 ROIs distributed over the focal plane with results plotted in Figure 5-3. In panel (A) the different peak amplitudes may be noticed between ROIs from different regions of the field of view. In panel (B), following normalization, the signal from all ROIs demonstrate the same pulse profile detected from the LED.

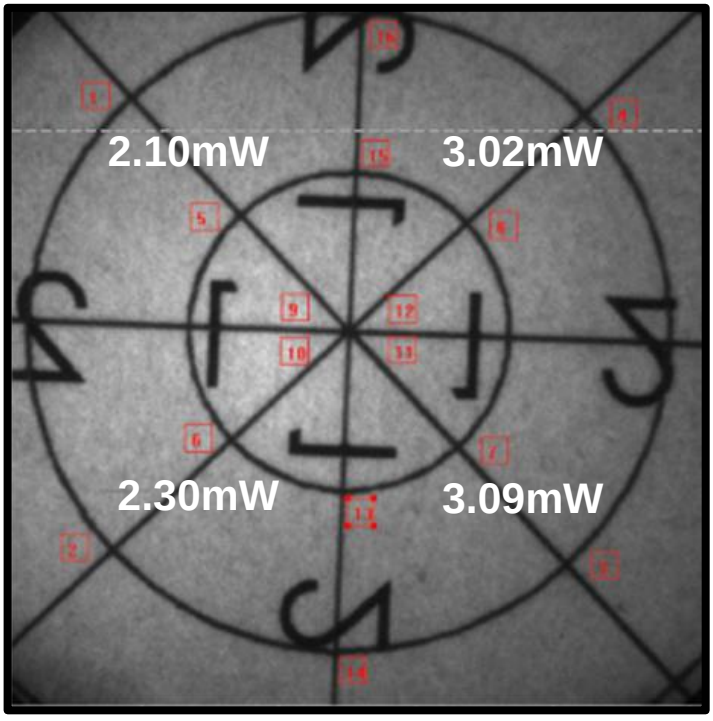

Figure 5-2: Light intensity at focal plane.
16 ROIs distributed in the field of view measure light intensity distribution at the focal plane.

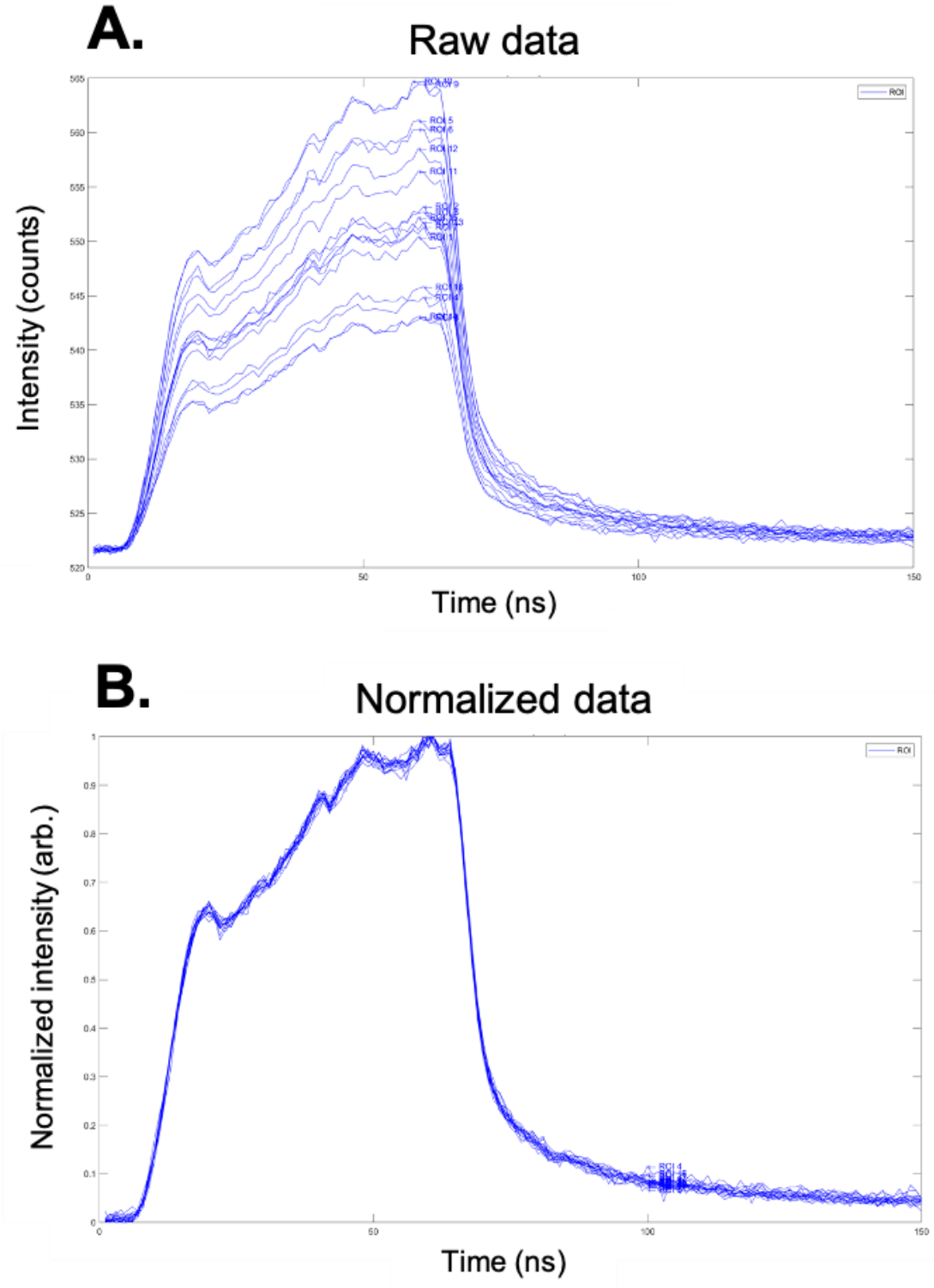

Figure 5-3: Method of image normalization in imaging system.
(A) Inhomogeneity in illumination results in different measured intensities between the ROIs. **(B)** Normalizing each pixel population to peak intensity results in system insensitivity to illumination inhomogeneity.

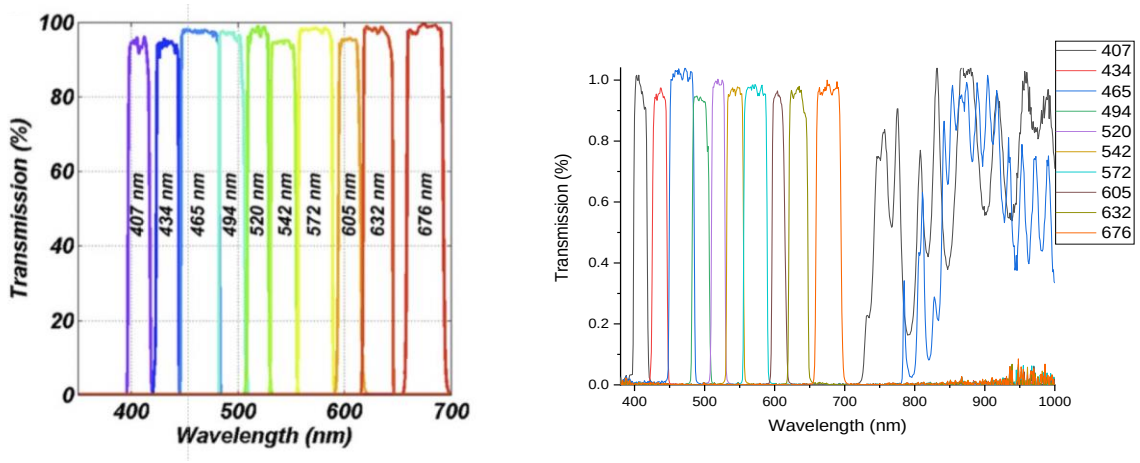

Figure 5-4: Theoretical and actual filter transmittance.
(Left) Filter specifications from Edmund Optics (Right) Actual filter transmittance was determined with custom built spectrometry system. Note the significant infrared-pass through.

Experimental verification of filter transmittance

The optical response of the LED was measured using the Andor iStar 334T camera. Spatial resolution was determined using a fluorescent 1951 USAF target (Edmund Optics) with peak excitation at 365nm and peak emission at 550nm. The filters were individually tested using a compact spectrometer (Thorlabs CCS200) with extended range (200-1000nm) and accompanying Thorlabs OSA software for PC. The spectra from each filter was normalized and plotted altogether using Matlab 2019b (Mathworks) with custom written code. The results are plotted in Figure 5-4.

System controlling computer

Several components of the associated computer hardware were upgraded in order to improve the stability of the system. While infrequent, there were several occasions in the previous system requiring restarting of the program or even rebooting of the computer that controlled the imaging system. In order to maximize performance in a small enclosure the decision was made to construct a custom computer based off of an Intel Nuc with 32Gb ram, 2Tb M.2 flash drive, and intel i7 six-core processor. An alternative would have been a workstation grade laptop but

concerns regarding security and storage were during lab meeting were raised concerning that option. The pc controller required power from electric mains and the highest-capacity uninterrupted power source that fit into the mobile cart was added. The nearly 80lbs power supply served as an excellent ballast for the new cart design to prevent tipping when the articulating arm is extended over the wheelbase.

Concerning software and operating system a switch was made from Labview to Matlab. This change permitted a unification of all aspects of system control, data acquisition, image processing, and storage. Ideally a Linux operating system would be chosen to minimize costs for future systems and further decrease operating system resource usage. In future iterations this change may also decrease the computer related cost of the imaging system. Open source alternatives could have been utilized to decrease cost but were not pursued in the interest of a rapid development time.

5.2.3 Ex-Vivo Imaging

Ex-vivo tissue was taken to CASIT for imaging in a black room with the improved system (system diagram in Figure 5-1). For illumination, a new LED board was manufactured for increased light intensity (40mW) with robust pulse shape at 365nm driven at 500kHz with 40ns pulse width.

The illuminating pulse was generated by a single high-power LED in this new system and transmitted to tissue via liquid light cable at a 45º incident angle. ROI selection (40x40 pixel) was completed by choosing tissue areas that were unambiguously normal or neoplastic based on morphological appearance and verified with correlated histopathology. For detection, a gated and intensified CCD camera (iStar, Andor technology) was coupled to a high-speed motorized 10 position filter wheel (Zaber) with bandpass filters (Semrock, blank, 405LP, 415/10, 434/17, 465/30, 494/20, 520/15, 542/27, 572/28, 605/15). 150x2 nanosecond bins were acquired with 1ns step size (0-150 ns overall acquisition time). DOCI values were then determined for each ROI, at

each wavelength, for each sample. The mean aggregate pixel populations in each ROI and their pooled variance were used for statistical analyses as detailed in 5.2.4.

5.2.4 Statistical Analysis

Pixel populations were generated by the tabulation of multiple 40 by 40 DOCI pixel values (depending on sample size) for each tissue type with gate widths of 30nm for both rise and decay across all samples. The means and pooled variances of these pixel populations were then normalized to the peak excited state fluorescence intensity with the average and standard deviation recorded for each set of averaged pixel populations within each acquisition. Tumor and adjacent healthy cutaneous skin were evaluated with a Wilcoxon rank-sum test (i.e., a modification of the t test that does not require the 2 test populations to have equal variances and does not require normal distributions of sample population variance). We opted to use the Wilcoxon rank-sum test because it is more stringent and thus forms a lower limit for the statistical significance of the imaging results. Wilcoxon rank-sum tests were performed between DOCI pixel populations from identified tumor and adjacent normal skin areas at each emission wavelength. Significance was set at $P<0.05$.ROI locations on specimens

5.3 Results

154 ROIs of 40 by 40 pixel areas were imaged across 10 individual resected SCC specimens (from eight patients) ex vivo. Resected tumors (ID # 2,3,4) all originated from one patient that had 3 separate SCC neoplasms resected from the scalp. Complete comparative results are presented in Table 11. The 434nm and 520nm filters significantly distinguished between all cases of primary SCC (ID#1-9). Specimen ID#10 was 1.5x1.5cm with a 0.3cm area of recurrent SCC from a previous surgery. In the patient chart the pathologist noted that the specimen exhibited extensive dermal scarring with severe background solar elastosis.

Detailed investigation was conducted for the ROIs of specimen (ID #7). Three groups of ROIs were generated, corresponding to HNSCC, hairy skin, and oral mucosa (Figure 5-5). The mean aggregate relative lifetime values were tested for statistical differences with multiple rank-sum tests with results presented in Figure 5-7. Each tissue region encircled with ROIs was subsequently validated by generated histopathology (Figure 5-7(B-D)). The temporal fluorescence of HNSCC of epidermal skin and oral mucosa (non-keratinizing stratified squamous epithelium) was further examined with 150 second exposures at each spectral wavelength. From this experiment, 30 nanosecond rise and decay are graphed in Figure 5-6. Significant spectral contrast was found between the tissue during rise and decay for nearly all spectral bands tested (Figure 5-7).

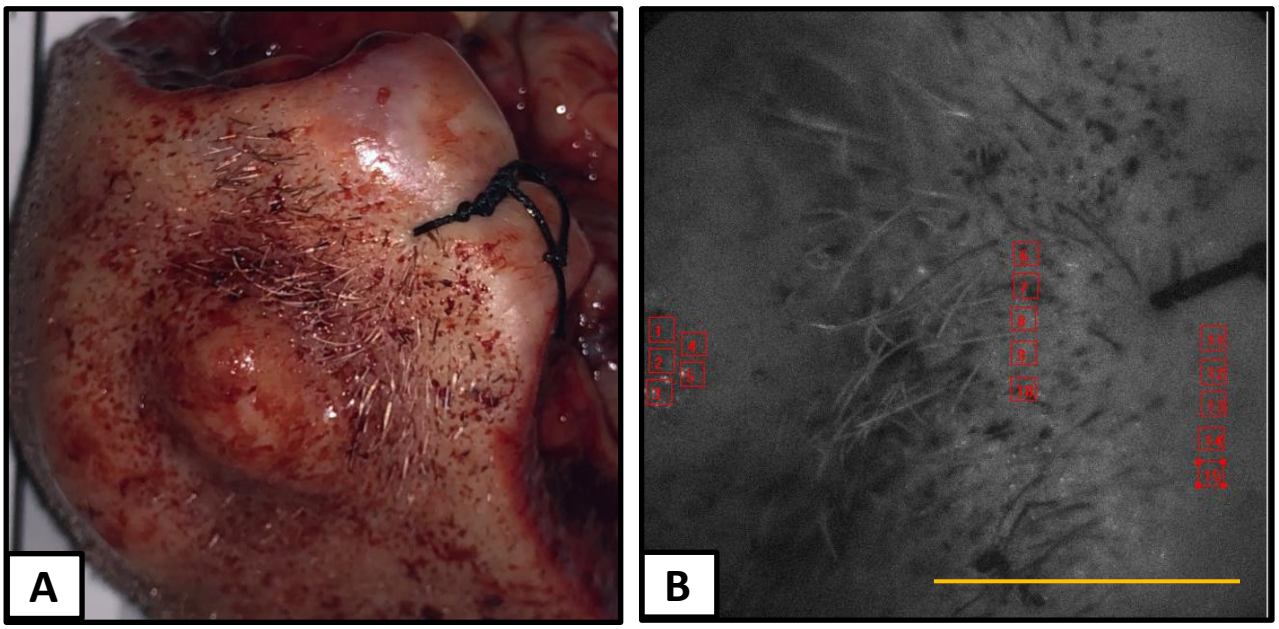

Figure 5-5: HNSCC of mandible (ID #7) and ROI locations.
(A) Ex vivo resected mandible of patient with superficial HNSCC. **(B)** 40x40 pixel regions of interest located over HNSCC protuberance (1-5) hairy skin (6-10) and oral mucosa (11-15). bar = 1cm

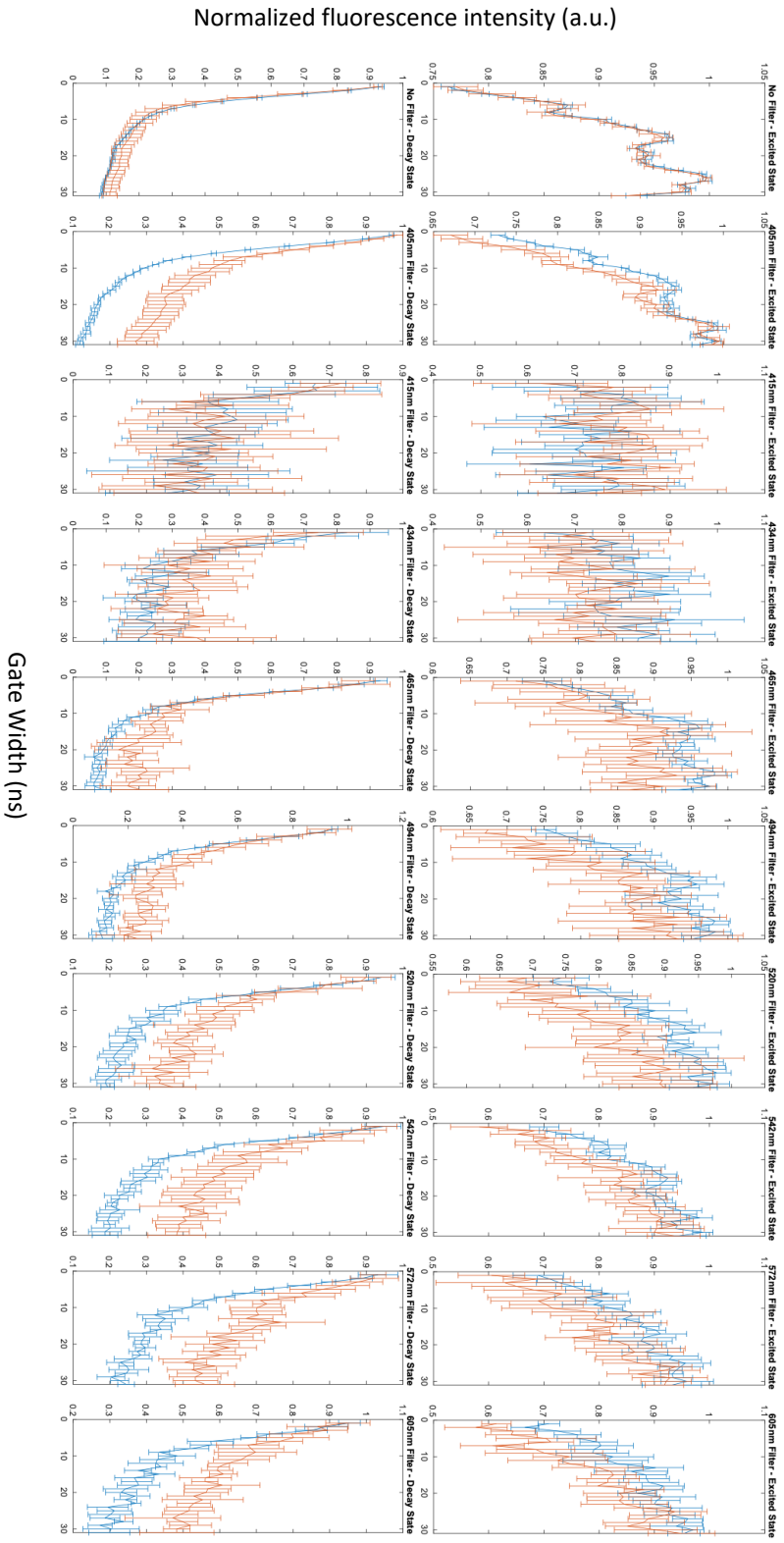

Figure 5-6: Excited and decay-states of endogenous tissue lifetimes significantly differ between superficial HNSCC and both epidermal skin and oral mucosa.
(A) Population mean lifetime kinetics between HNSCC and oral mucosa (non-keratinizing stratified squamous epithelium).

A.

		HNSCC vs.	
		Hairy epidermal skin	Oral mucosa
Excited State	Blank	0.6625	0.7568
	405LP	0.1857	0.1811
	415	<0.001	0.0033
	434	<0.001	<0.001
	465	0.0001	0.0002
	494	0.0003	0.0002
	520	0.0007	<0.001
	542	0.0149	0.0045
	572	0.0096	0.0045
	605	0.1054	0.0049
Decay State	Blank	0.0143	0.2314
	405LP	0.0005	0.0001
	415	<0.001	0.5082
	434	<0.001	0.0005
	465	0.0027	0.0015
	494	0.0015	0.0008
	520	0.0004	0.0002
	542	0.0003	<0.001
	572	0.0004	<0.001
	605	<0.001	<0.001

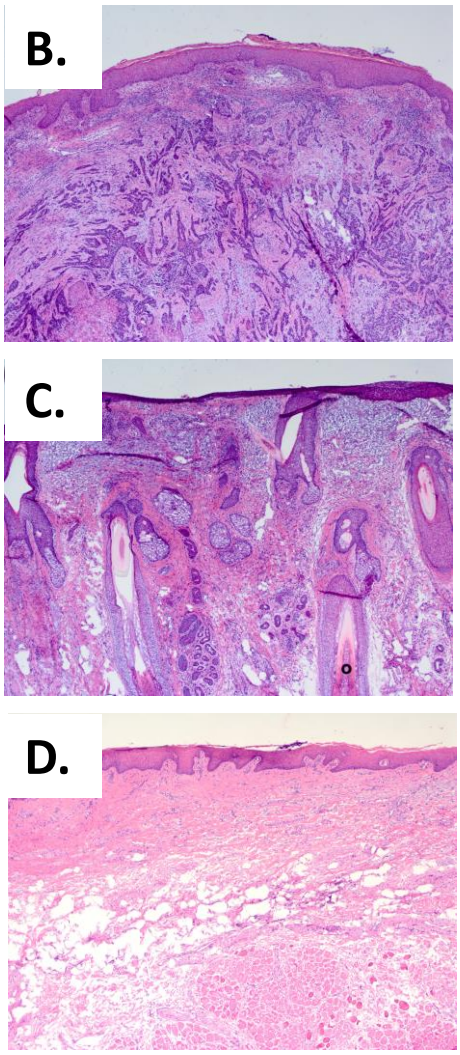

Figure 5-7: Rank sum tests and histology validation.
(A) Epidermal skin outside the mouth (keratinized stratified squamous epithelium). **(B,C,D)** Histological verification of HNSCC, epidermal skin, and oral mucosa, respectively.

5.4 Discussion and Conclusion

In this study, we validated our re-designed and significantly improved imaging tool. Our method utilized a safe and low-cost single LED for illumination, was insensitive to inhomogeneities in illumination, and significantly distinguished between cutaneous SCC, cutaneous hairy skin, and oral mucosa.

Based on results from the previous clinical study, The highly irregular surfaces, sizes, and consistencies of resected tumors made fluorescence lifetime imaging challenging. In addition, the patient samples were far more heterogenous than originally expected. Patient age, medical history, comorbidities, prior procedures, presence or absence of prior chemoradiation, and duration of time since first diagnosis of carcinoma are just a few of the factors that influenced sample diversity. Fluorescence lifetime measurements are sensitive to the microenvironment of the fluorophores studied and all of these factors are likely to have some effect on the morphologic and metabolic state of the tissue studied. Regarding specimens obtained from the Department of Head and Neck Surgery, resected primary SCC from the scalp exhibited the most favorable geometry for imaging. Thus, the decision was made to primarily image resected primary SCC specimens for system validation. Ex-vivo tissue samples correlated with histology and generated images to demonstrate the capability of the system to produce useful contrast for the operating surgeon toward identifying tissue and determining boundaries.

Spectral differences were consistent across multiple ROIs within the same specimen, and also robust between ROIs across nine different ex-vivo specimens. One specimen (ID #10) did not reveal significant contrast during decay. This specimen was the only case of recurrent and non-primary HNSCC, and the significant dermal scarring from previous surgery (as noted in the pathology report) may have affected the resolution of the DOCI system. If confirmed, this finding may also influence future inclusion criteria for a larger clinical trial.

Table 11: Autofluorescence lifetime differences are robust between ex vivo specimens with primary HNSCC.

	ID #	1	2	3	4	5	6	7	8	9	10
	Disease and Region	SCC - Nose	SCC - Scalp	SCC - Scalp	SCC - Scalp	SCC - Scalp	SCC - Scalp	SCC - Mandible	SCC - Mandible	SCC - Tongue	SCC - Scalp **recurrent**
Excited State	Blank	0.5172	0.9215	0.4641	0.6934	0.7891	0.9495	0.8992	0.3175	0.6831	0.7945
	405LP	0.3751	0.5082	0.1765	0.1857	0.2975	0.5927	0.1634	0.1592	0.6934	0.7461
	415	0.9663	0.0161	<0.001	<0.001	0.0281	0.0028	<0.001	<0.001	<0.001	0.0471
	434	0.132	0.0053	<0.001	<0.001	0.0398	0.0053	0.5082	<0.001	0.0003	0.2102
	465	0.5356	0.0137	<0.001	0.0008	0.2154	0.7783	0.0002	0.0002	0.0028	0.2314
	494	0.5172	0.0261	0.0002	0.0281	0.3313	0.1249	0.0611	0.0132	0.4815	0.3751
	520	0.0555	0.2426	0.0008	0.0033	0.1356	0.0324	0.0002	<0.001	0.2051	0.237
	542	0.1677	0.0693	0.0006	0.2314	0.3313	0.2721	0.2721	0.0173	0.0017	0.155
	572	0.0715	0.237	0.0003	0.1148	0.3041	0.0833	0.4471	0.0127	0.0001	0.2051
	605	0.0651	0.8327	0.0672	0.3905	0.6222	0.0226	0.3384	0.0209	0.0004	0.1116
Decay State	Blank	0.0784	0.3455	0.0261	0.0202	0.7783	0.888	0.147	0.0085	0.4387	0.3384
	405LP	0.0072	0.1284	0.0047	0.0025	0.0261	0.0291	0.0016	0.0002	0.1249	0.4992
	415	0.0538	0.5543	<0.001	<0.001	0.4815	0.0031	<0.001	0.0049	0.0385	0.3905
	434	0.0127	0.0441	<0.001	0.0002	0.0324	0.0471	0.0359	0.0002	0.0058	0.1765
	465	0.0194	0.0715	0.0004	0.0252	0.8108	0.4305	0.0058	0.0053	0.0471	0.4992
	494	0.0015	0.0651	0.0003	0.0034	0.0859	0.0471	0.0013	0.0004	0.0631	0.8437
	520	0.0007	0.0291	0.0003	0.0008	0.0252	0.0041	0.0053	0.002	0.0302	0.4471
	542	0.0008	0.0939	0.0013	0.001	0.0108	0.0025	0.0003	0.0004	0.0217	0.2102
	572	0.0026	0.1024	0.0024	0.002	0.0072	0.0025	0.0043	0.0008	0.0693	0.4142
	605	0.0037	0.2102	0.0045	0.0039	0.0034	0.0017	0.0784	0.0007	0.5449	0.1054

The relative lifetime contrast between carcinoma and adjacent visually normal tissue was significant at nearly every spectral wavelength, with differences present during both decay and rise from the improved LED pulse profile. Notably, the improved system revealed significant contrast between malignant neoplasms and both non-keratinized and keratinized cutaneous tissue. Subsequently, the significant DOCI contrast was confirmed via histology and interpretation by pathologist. In comparison, the previous clinical system with six LEDs did not yield significant results when imaging keratinized cutaneous tissues.

A limitation to this study is system standardization between imaging sessions and different specimens. This issue is addressed in greater detail parathyroid identification in CHAPTER 6:.

In summary, the presented results support ongoing efforts of adapting the DOCI algorithm into an imaging technology permitting characterization and differentiation of HNSCC and different tissues in situ. Besides increasing the sample size, next steps will be en-face imaging of the interior surfaces of bisected tissue in order to permit co-registration of DOCI images with histological sections in congruent anatomical planes.

CHAPTER 6: PARATHYROID IDENTIFICATION WITH DYNAMIC OPTICAL CONTRAST IMAGING

6.1 Introduction

Primary hyperparathyroidism, often caused by a single adenoma (80-85%) or four-gland hyperplasia (10-15%), can lead to elevated parathyroid hormone (PTH) levels and resultant hypercalcemia (240–242). Surgical excision of offending lesions is the standard of care, as the removal of pathologic adenomas reduces PTH and calcium values to baseline and avoids the risk of associated morbidities (242). The small size, variable location, and indistinct external features of parathyroid glands can make their identification quite challenging intraoperatively (243,244). Patient prognosis depends heavily on complete resection of the involved parathyroid glands. The inability to accurately localize the parathyroid glands during parathyroidectomy and thyroidectomy procedures can prevent patients from achieving postoperative normocalcemia. The goal of these surgeries is to remove the diseased thyroid or parathyroid tissues while minimizing risks to surrounding nerves and vessels. Rapid imaging methods that can accurately and efficiently identify parathyroid gland tissue and differentiate it from surrounding neck tissues would be transformative in gland localization.

Approximately 80,000 parathyroid and thyroid surgeries are performed in the United States each year. One of the most common problems in the surgical intervention of patients with parathyroid and thyroid disease is the inability to localize the parathyroid glands (243,244). Thyroid and parathyroid surgery involves dissection through skin and subcutaneous tissues, retraction of neck muscles, and a careful dissection of the thyroid gland as the parathyroid glands are most often located on the posterior surface of the thyroid. Illustrated in Figure 6-1, the Recurrent laryngeal nerve (RLN, responsible for allowing proper vocal cord motion) is located behind the thyroid gland

often intimately related to the parathyroid glands anatomically. If the RLN is damaged on one side this may lead to vocal cord paralysis and possible tracheostomy.

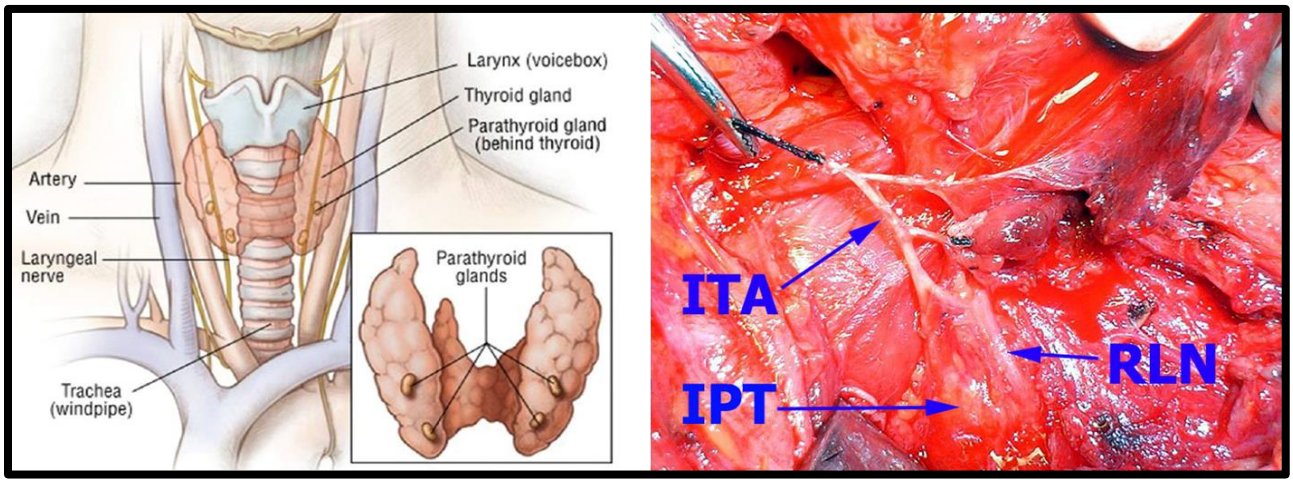

Figure 6-1: Variable location and indistinct features make parathyroid localization difficult. Adapted from Gad SS, Elsamie MA, Saleh YA. Parathyroid gland injuries during total and subtotal thyroidectomy. Menoufia Med J 2015;28:807-12

The challenge of parathyroid localization is heightened in patients undergoing reoperation or presenting with ectopic and/or supernumerary abnormal glands (243,244). Accidental removal of healthy parathyroid glands during thyroid surgery causes postoperative hypocalcemia in 20% to 30% of thyroidectomy cases (243,244). Complications, including hypoparathyroidism and RLN injury, are generally limited in experienced hands(245) however, revision surgery and comprehensive exploration increase this risk(240). In cases where the parathyroid glands are diseased, insufficient removal of affected parathyroid glands during parathyroidectomy can require reoperation due to persistent hypercalcemia (244,246).

Precise preoperative localization of parathyroid adenomas can help the surgeon formulate strategic operative plans and perform minimally invasive parathyroidectomies (MIP) that lead to smaller incisions, limited dissection, decreased pain, reduced hospital lengths of stay, and decreased overall cost (240,245,247–250). Although primary hyperparathyroidism is most

commonly caused by a single parathyroid adenoma, 10%–30% of patients will have multigland disease (MGD) due to parathyroid hyperplasia or multiple adenomas (249,250). This group represents a challenge for radiologists and surgeons because these patients have a much higher frequency of nonlocalizing imaging studies and failed surgeries (249,250).

Though there exists a multitude of imaging studies like ultrasonography (US), 99mTc- sestamibi SPECT/CT (SeS), computed tomography (CT), and magnetic resonance imaging (MRI), the choice and quality of imaging studies differ depending on surgeon preference, technology availability, and operator skill (249). The sensitivities for ultrasonography and sestamibi imaging glands vary, ranging from 64 to 76% and 58 to 90%, respectively (249,251). SeS requires the administration of radiotracers and results can be affected by nonselective tissue uptake. Ultrasonography, while widely utilized, is suboptimal in patients with co-existing nodular thyroid disease or deep-seated adenomas (252). These methods are limited by their inability to reliably localize healthy glands or provide rapid intraoperative information.

Concerning optical approaches, earlier work in fluorescence lifetime imaging (FLIM) has demonstrated potential value for functional imaging (253–256). FLIM is a technique where the auto-fluorescence of a sample is probed in both the wavelength and time domains by excitation of the sample with a short optical pulse. Subsequently, the autofluorescence lifetime of tissue is detected at a range of different wavelengths (257). Lifetimes are dependent on the intrinsic biochemical composition of the targeted material and significant contrast can be generated by mapping the measured decays into an image. Thus, advantages of this technique are that time-resolved fluorescence is invariant to obscurants in the surgical field (blood, sweat, hair, etc.) and surfaces defined by complex geometries. In addition, fluorophore lifetimes are often strongly dependent on conditions related to occurring physiological processes, (e.g., oxygenation, pH, and temperature). Together, these characteristics of FLIM support its application towards in situ

functional imaging and tissue identification (176). The utility of fluorophore lifetimes in application to intraoperative localization of tissue is an active area of research especially relevant to head and neck surgery due to the high density and proximity of delicate anatomy (e.g., carotid artery and recurrent laryngeal nerve) to areas frequently undergoing operation. Currently there are insufficient instruments to intraoperatively delineate parathyroid tissue.

This work presents the application of ratiometric fluorescence lifetime imaging system termed Dynamic Optical Contrast Imaging (DOCI) for enhanced intraoperative parathyroid localization. In addition to demonstrating image contrast between parathyroid tissue and adjacent fatty tissue, we sought to validate our results through two-photon imaging. Another aim was to standardize the values generated by our DOCI system to actual fluorescence lifetimes using reference fluorophores and a commercial two photon imaging system.

6.2 Materials and Methods

All studies were conducted with appropriate IRB approval. The protocol, system used for ex vivo imaging, and statistical analyses of ROIs based on segmentation are described in section 0. In addition to the description therein, a validation experiment was conducted between the resultant DOCI contrast in imagery and the actual fluorescence lifetimes of both unstained parathyroid tissue and adjacent adipose tissue as analyzed in the phasor space (using n-exponential fit algorithm of the FLIM module in LASX software by Leica) using a commercial Leica DIVE multiphoton FLIM imaging system at the California Nanosystem Institute at University of California, Los Angeles. The total planned time for parathyroid imaging is four hours following resection. Parathyroid autofluorescence intensity has been reported to decrease over time following excision ($T_{1/2}$ 150hours) but changes with respect to fluorescence lifetime could not be found in existing literature(258).

Regarding the standardization experiment, stock solutions of NADH, Laurdan, and 7-hydroxy-4-methylcoumarin were prepared as detailed in Figure 6-2. The stock solutions were then immediately split in two equal parts with one half of each solution transported taken to the experimental DOCI system and imaged while the other half was imaged by a commercial Leica SP8 MP-DIVE system with FLIM extension at the nearby California NanoSystems Institute located at the University of California at Los Angeles. 100 microliter samples of each dye were pipetted into open top 12-well slides and excited with a femtosecond pulsed laser at 736nm for two photon occurrence at approximately the same 365nm emission of the LED in the DOCI system. The SP8 microscope used a Leica HC PL FLUOTAR 10x/0.40 CS2 Dry objective and HyD detector. The Leica HyD detector was configured with a 408-550nm bandpass filter while the DOCI system utilized a 405 long-pass filter, thus solely filtering out the illuminating wavelengths of light. Fluorescence lifetimes for each dye were determined at multiple concentrations using the fit-free phasor module of the Las X (Leica) software with n-exponential autofitting enabled. Results were analyzed for linearity using Prism 8 (Graphpad) for Mac OS by creating a best-fit-line with simple linear regression. Error in DOCI lifetime value was calculated by measuring the absolute value of the difference between middle DOCI value and corresponding empirically measured fluorescence lifetime divided by the empirically measured fluorescence lifetime. The standardized temporal resolution of the DOCI system was determined by fitting a line through the longest and shortest DOCI values and comparing against their referenced lifetime values as determined from two-photon experiment detailed above.

6.3 Results

6.3.1 Standardization Against Fluorescent Dye and Commercial Two-Photon Microscope

Results from standardization experiment with different fluorescent dye of known lifetime are presented in Figure 6-2. Regarding the standardization experiment, stock solutions of NADH, Laurdan, and 7-hydroxy-4-methylcoumarin were prepared as detailed in Figure 6-2. The stock solutions were then immediately split in two equal parts with one half of each solution transported to the experimental DOCI system and imaged while the other half was imaged by two-photon microscope at the California NanoSystems Institute. Both DOCI and two-photon imaging began within 15 minutes from the split of the diluted solutions. The fluorescent dye were imaged concurrently with the DOCI system and commercial two-photon microscope in order to control for changes in lifetime due to exposure to oxygen. Imaging with the DOCI system was completed within ~40 minutes while imaging with the two-photon system lasted two hours. Phasor analysis of each reference dye was performed with the two photon system to determine sample purity and single exponential nature of fluorophore lifetime decay (data not shown). The temporal resolution of the DOCI system was standardized against actual lifetime values in the range of zero to eight nanoseconds where each 0.01 change in DOCI value equated to 0.2127 ± 0.0206 (ns) lifetime change. The error in DOCI measurement was 9.8%. These results were confirmed in repeated experiment (data not shown).

Dye	**Solvent**	**Concentration** (uM)	**Lifetime** (ns)	**DOCI Value** (0-1)
7-hydroxy-4-methylcoumarin	Distilled water	400	5.229	0.8556
		260	5.243	
Laurdan	Methanol	1000	3.143	
		650	3.106	0.7653
		430	3.172	
NADH	Distilled water	21500	0.397	0.6280
		14500	0.417	

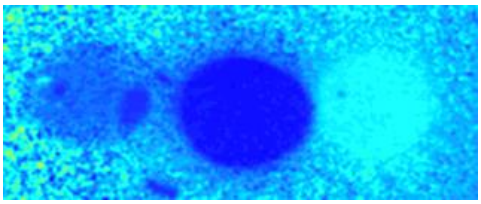

Laurdan,650 | NADH-21500 | 7-C,400

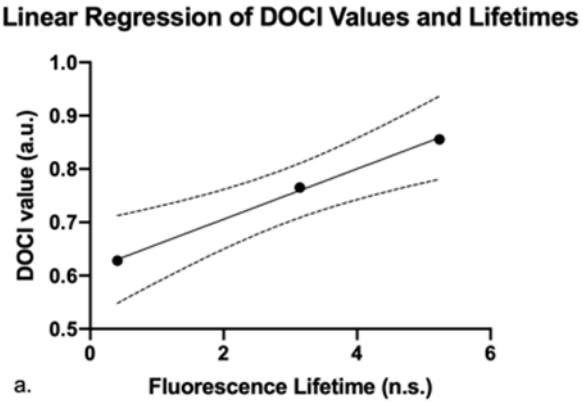

Figure 6-2: Lifetime analysis of reference dye between DOCI system and Leica MP-DIVE FLIM system.

6.3.2 Ex Vivo Parathyroid Measurement

The specimen for this study was from a 74 year old female patient who presented to the Department of Head and Neck Surgery with primary hyperparathyroidism and a thyroid nodule scheduled for parathyroidectomy and right thyroid lobectomy. Following appropriate consent, the right superior parathyroid gland and small fragment of adjacent fat were recovered and imaged with the DOCI system within one hour following surgical excision. The total time spent imaging the tissue with the DOCI system was about an hour and a half. In order to validate DOCI contrast the excised tissue was then transported (15 minutes) and immediately imaged at the nearby two-photon fluorescence lifetime imaging facility on campus. The total time spent with the two-photon microscope was approximately two hours, after which the specimen was returned to surgical

pathology for routine histopathology. The irregular soft tissue fragment weighed 0.13g and measured 1.2 x 0.5 x 0.2 cm. The department pathologist confirmed the presence of an enlarged, hypercellular parathyroid with extracellular fat tissue with conventional H&E stain.

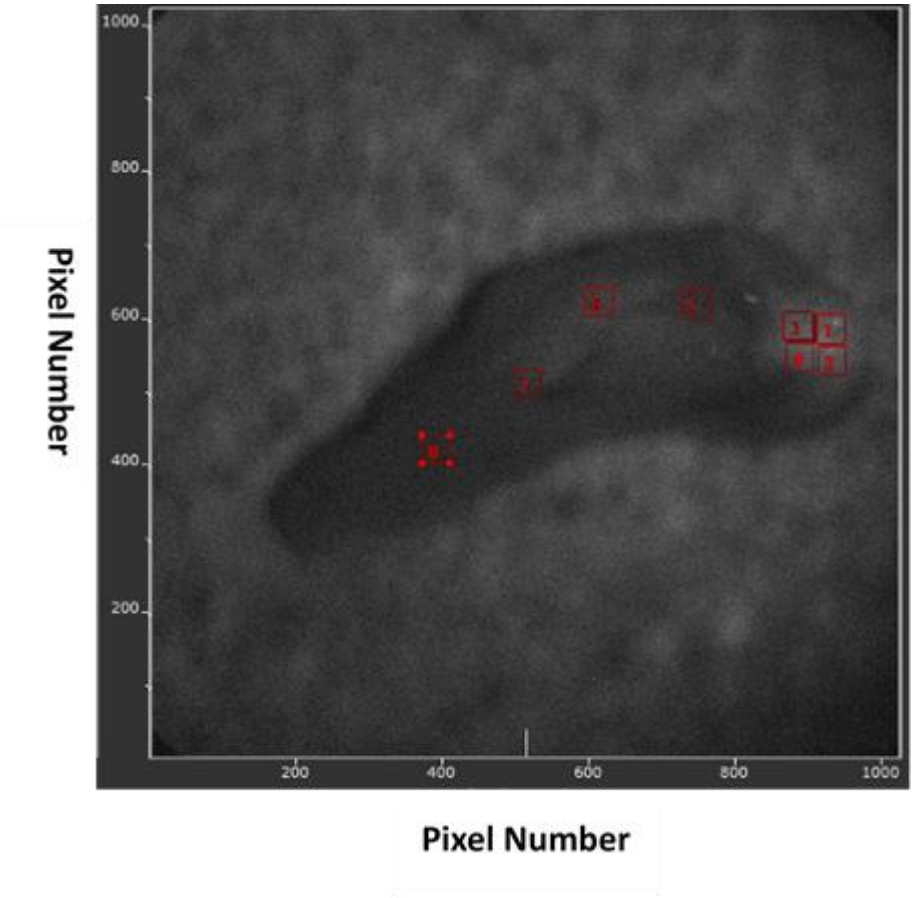

Figure 6-3: Region of interest locations for parathyroid adenoma and adjacent adipose tissue

ROI-based long exposure was conducted where imaging data was acquired from eight ROIs (40 x 40 pixel each) that were evenly distributed between two equal groups denoted “fat” or “parathyroid” tissue. The exact locations of the eight ROIs are presented in Figure 6-3. The regions were selected based on morphologic evaluation and guidance from the chair of the Head and Neck Surgery department and confirmed via routine histopathology following the study (Figure 6-5(D)). The exposure time was 150 seconds for each spectral channel with 150, two-nanosecond bins and one nanosecond step size.

Whole field image acquisition was performed following ROI-based acquisition. One intensity image and nine spectral DOCI images were acquired of the entire gland with adjacent fat tissue. The near real-time graphical output that was immediately displayed to the user is presented in Figure 6-5(B,C1-C9). The exposure time per spectral channel was one second with individual gate widths of 35ns for both steady-state and decay frames.

After completion of imaging the data were analyzed with hypothesis testing for statistical significance offline. In Figure 6-4, 30ns of individual DOCI values are plotted (mean and standard deviation) for the two groups of ROIs. Individual rank-sum tests were conducted comparing relative lifetime of parathyroid tissue versus fatty tissue for each spectral band and also state of fluorescence (i.e., rise or fall). During the rising state (i.e., tissue pump by LED begins) a statistically significant difference ($P<0.05$) was found between parathyroid tissue and adjacent adipose tissue in four spectral bands (i.e., 415,434,465, and 494nm). During the decay state there were two spectral bands that revealed a significant difference (405LP and 415nm) between the two tissue types.

Two-photon imaging of the parathyroid generated five, 200x200um size tiles (each composed of five averaged line-scans each). These five tiles were stitched together to create the 200umx1mm image in Figure 6-5(F) with LASX for Life Sciences application by Leica. N-exponential fit was used to estimate the lifetimes for two areas off tissue. These areas are represented by false-coloring that corresponds to the average lifetime of the major component in the focal plane. The colormap was chosen to encompass the lifetimes of both tissue groups as represented in the phasor space.

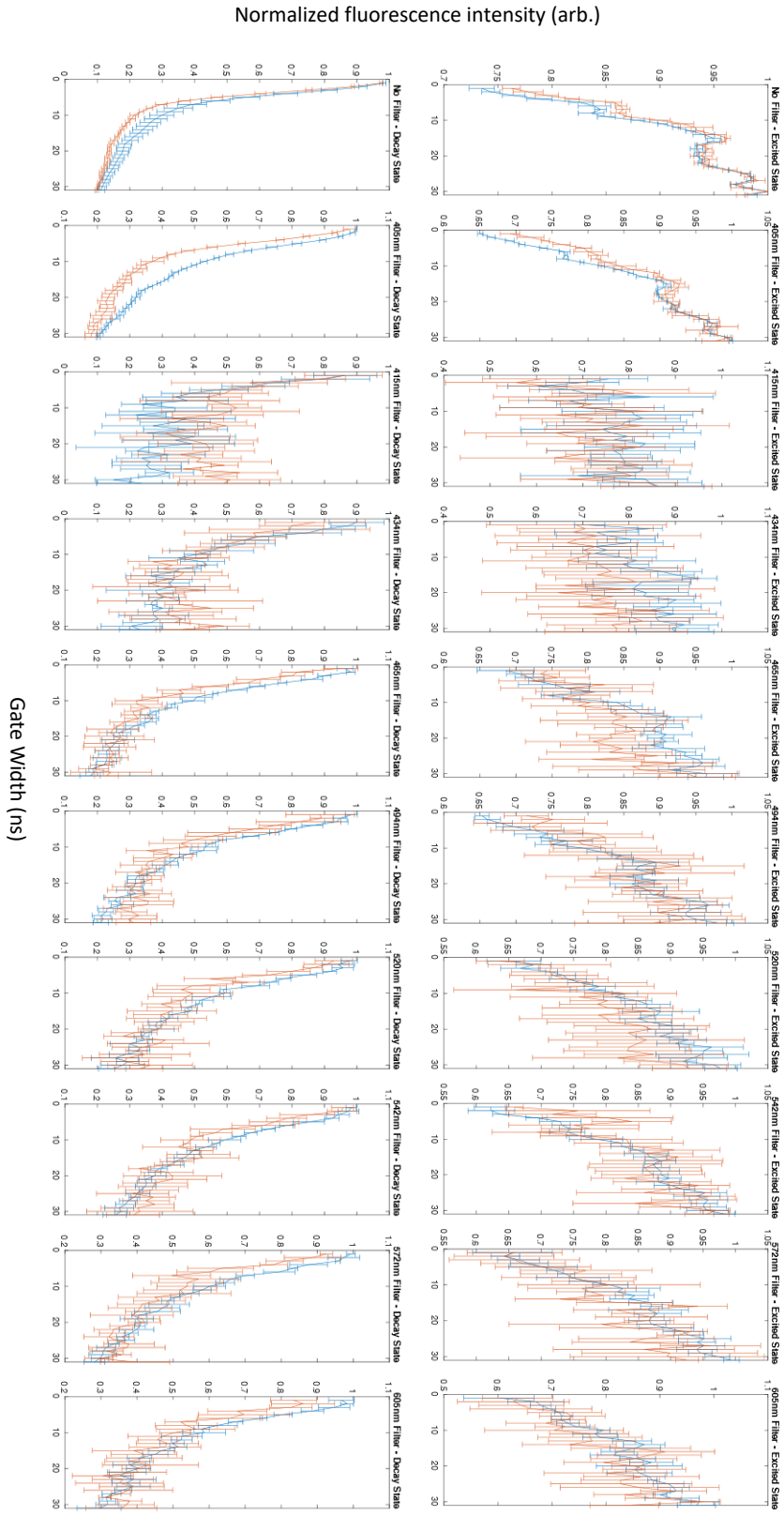

Figure 6-4: Population mean lifetime kinetics between Parathyroid adenoma and adjacent adipose tissue across ten spectral bands.

Table 12: Excited-state and decay-state endogenous tissue lifetimes are significant between parathyroid adenoma and adipose tissue.

		Parathyroid adenoma vs. adipose tissue
Rise State	No Filter	0.5403
	405LP	0.4641
	415	0.0187
	434	0.0001
	465	0.0252
	494	0.9103
	520	0.0167
	542	1
	572	0.1677
	605	0.2051
Decay State	No Filter	0.0738
	405LP	0.0291
	415	0.0001
	434	0.2154
	465	0.5264
	494	0.8108
	520	0.7675
	542	0.8327
	572	0.5172
	605	0.6934

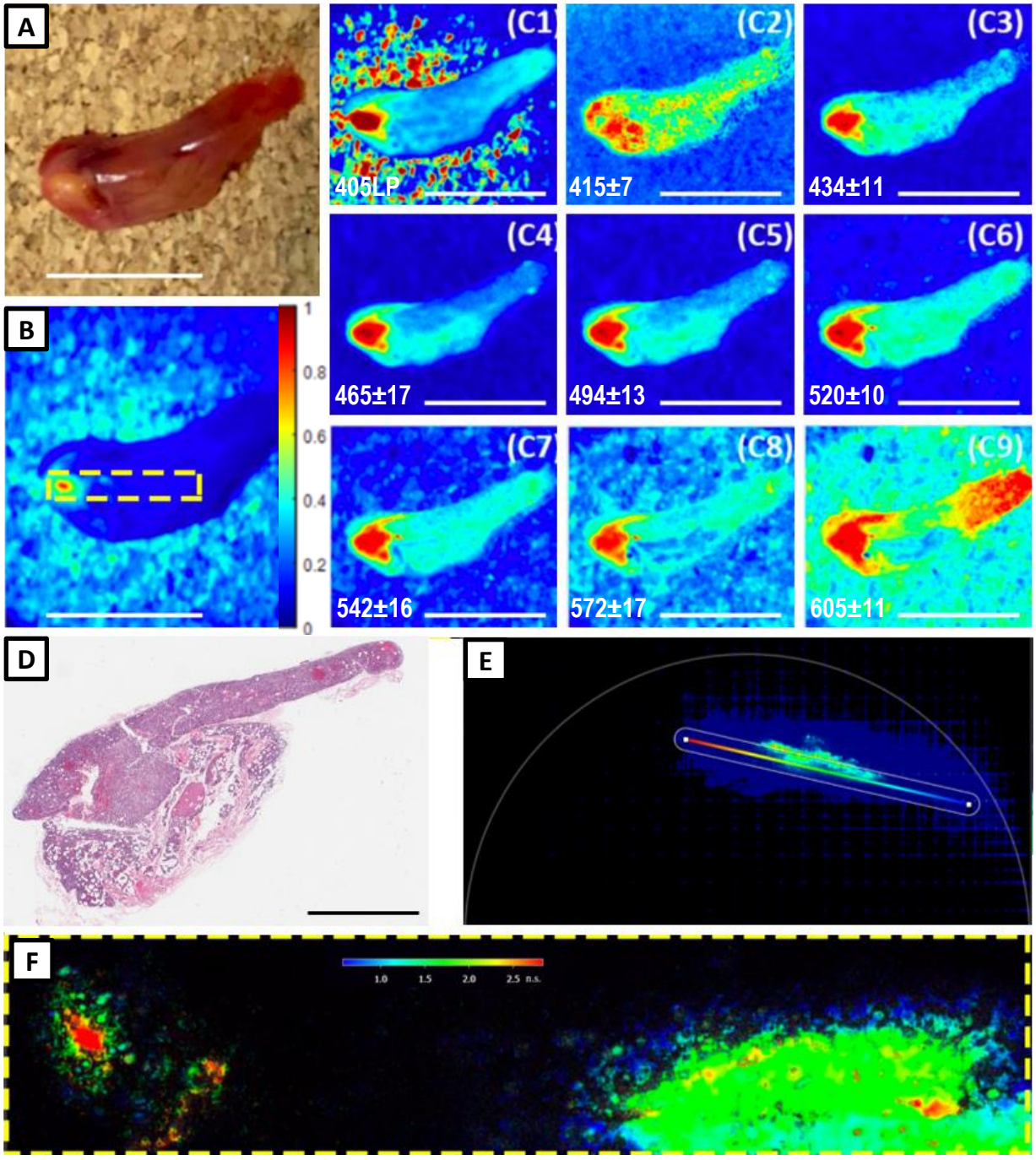

Figure 6-5: Full-field DOCI image of parathyroid adenoma and adjacent adipose tissue. Temporal resolution of DOCI system with ex vivo human parathyroid referenced against Leica SP8 MP-DIVE system. **(A)** Image of parathyroid gland and adjacent fat; **(B)** Fluorescence intensity image of parathyroid and adjacent fat (taken with video mode of DOCI system); **(C1)-(C9)** DOCI relative lifetime images of parathyroid and adjacent fat with different filters(FWHM/2), ; **(D)** H&E histology; **(E)** Phasor plot; **(F)** Fluorescence lifetime image taken with commercially available FLIM microscope, Leica Deep In Vivo Explorer SP8 DIVE. Full F-panel is 1cm.

6.4 Discussion

The goal of this work was to determine if Dynamic Optical Contrast Imaging could generate unique spectral contrast between parathyroid and adjacent fatty tissue ex vivo. Moreover, this study aimed to validate and standardize the relative measurements produced by our DOCI system. For that purpose, a sample of parathyroid and adjacent fatty tissue were both imaged using the DOCI system and a commercial two-photon microscope. Through second experiment, dye solutions were prepared in order to quantitatively verify the concordance between the relative DOCI values (i.e., between 0 and 1) and actual fluorescence lifetime measurements by two-photon microscopy on the picosecond scale.

Results from this study serve as an initial investigation into the study of relative lifetime measurements of parathyroid tissue with dynamic optical contrast imaging. Significant contrast was produced between parathyroid and adjacent fatty tissue as confirmed by rank-sum test at 405 long pass and 415nm filters during decay and even across several bands during rise in whole-field DOCI images. The lifetime difference between tissues was subsequently validated by two-photon lifetime measurements with the same specimen. Notably, in Figure 6-5, it appears possible to distinguish between normocellular and hypercellular parathyroid using DOCI yet this contrast was not otherwise visible to the unaided eye (i.e., as illustrated in the intensity image Figure 6-5(A)). Contrast was already apparent between the fatty tissue and parathyroid but after using DOCI this difference was also augmented. The adjacent fatty tissue was lost during the process of histologic processing (as is expected) but the hypercellular and normocellular parathyroid is readily apparent.

Parathyroid autofluorescence has gained increasing attention in the past decade but time-resolved fluorescent properties of the gland remain to be adequately characterized(259,260). In

addition, a limitation regarding evaluation of results is that healthy and benign parathyroid tissue are reported to have multiple lifetimes due to yet to be discovered fluorophores(259,261). In one study of just ten specimens a lifetime difference of about 0.5 nanoseconds was reported between normocellular and hypercellular parathyroid(259). In this study the results are not sufficiently powered to make conclusions regarding the lifetime properties of parathyroid tissue. However, the values generated by our novel system are plausible when related to prior reports of lifetime, and were further supported with two photon measurement. The validity of this contrast in the DOCI image was moreover supported by the results that the standardized temporal resolution of the system was under one-half nanosecond (0.21±0.2ns). Finally, these findings are also in concordance with our prior work relating to parathyroid identification with relative lifetime imaging(239,262,263). Thus, our system generated highly accurate and clinically useful images within seconds at the cost of under 50 thousand dollars. In comparison, the 1.3 million dollar Leica SP8 DIVE system required two hours of time to produce a micrometer thin cross-section of lifetime values with an order of magnitude smaller field of view.

The results from dye standardization demonstrate a clear linear correlation between single exponential dye fluorescence lifetimes and corresponding (0-1) DOCI values. This finding suggests the possibility of converting the relative lifetime measurements from the DOCI system into actual lifetime values(264). In summary, our next-generation DOCI system demonstrates clinically meaningful contrast in near real-time based on measurement of aggregate endogenous fluorescence lifetime. While the focus of this work concerns relative lifetime imaging, this is a significant finding that merits continued research.

6.5 Conclusions

Given its variable location and indistinct features no standard accepted tool currently exists for parathyroid localization. In this study, significant DOCI contrast was produced in the parathyroid at unique spectral bands. This finding may enable a reduction in filter number and thus a decrease in overall imaging time. The contrast from our novel system was verified through two-photon microscopy, and also supports further research concerning the potential use of DOCI for surgical guidance in endocrine surgery. The DOCI measurements were standardized using reference dye and a commercial two-photon system to determine that each 0.01 increment in relative lifetime value equated to 0.2127 ± 0.0206 (ns) absolute fluorescence lifetime change. The standardization of system values and the linearity of the measurements suggest this method may be used for true fluorescence lifetime measurements. These results and methods permit system calibration over time and also between different systems, which would be necessary in a future multi-site clinical trial of the system.

CHAPTER 7: NEW METHOD FOR DYNAMIC OPTICAL CONTRAST IMAGING

7.1 Background

Biomedical imaging has become an indispensable tool in comprehensive cancer surgery (265). While some aims are much closer to full realization, continuing advances in biomedical photonics may help detect pre-malignant lesions, detect cancer in less invasive stages, reduce the number of unnecessary biopsies, and also provide guidance towards the complete tumor removal with precise resection margins (8,266). Intraoperative guidance with X-ray, ultrasound, and MRI are certainly feasible, yet limitations exist in the widespread integration of these imaging modalities. For example, the principle use of such tools remains in the preoperative localization of many larger tumors (e.g., oral, liver, lung, kidney, brain). During an operation, the surgeon typically relies on white light reflectance, his or her tactile senses, and intermittent tissue biopsy with rapid frozen section pathology (266,267). Accuracy varies widely based on the experience of the surgeon, the pathologist, and the location and type of tumor (46,268). In addition, efficacy is confounded by limitations on the extent of resection due risks of damage to adjacent vital structures (168). The lack of any standard technology applied in the field of head and neck oncology to enhance intraoperative margin control clearly underscores this pressing medical need.

In order to generate functional tissue contrast via lifetime imaging our team published a novel method termed dynamic optical contrast imaging (DOCI) (238,239,269). The basis of tissue contrast in DOCI is due to biochemical, metabolic (i.e. altered concentrations of NADH and FAD), and structural changes that alter the emission properties of cancerous tissue (191,270–272). Over the course of carcinogenesis, the contribution of NADH to fluorescence substantially rises. NADH has a short lifetime (~ 0.5ns for unbound; ~1ns for bound) and results in a decrease in fluorescence lifetime in malignant tissue (174,179,191,273). These findings are consistent with

our previous results and suggest that biochemical changes in OSCC tissue gives rise to fluorophore lifetime related contrast that is sufficient to discriminate OSCC from normal tissue (238).We have recently demonstrated the use of light emitting diodes (LED) and novel DOCI based contrast generation algorithms for the detection of various types of collagens, elastin, (208,274) and the ex vivo delineation of parathyroid tissue from non- parathyroid tissue (275).

7.2 Detailed Description

Our next step was to develop our imaging system as a tool for intraoperative use. Over the course of our extensive work on developing an integrated LED driver circuit (in order to optimize the linear fall time from steady state illumination to between 1-10 nanoseconds), the LED rise time has also become sufficiently linear with a 1-10 nanosecond rise time that permits a new avenue to gather useful fluorescent contrast in various specimens (e.g., parathyroid, Figure 7-1). Previous literature and teachings discourage tissue differentiation based on fluorescent contrast during excitation and teach that only fluorophore decay from an excited state contains contrast information unique to the fluorophores of a specimen. The author's understand this common conclusion, since in nearly every application of fluorescence lifetime imaging the illumination source resembles an impulse function (e.g., via the use of a laser) or is exponential in nature. In our work, LED illumination permits a nearly linear rise, steady-state, and falling intensity with respect to time on the nanosecond order. With these specifications, fluorescence lifetime contrast is attainable when normalizing the sample fluorescence during both the rising and decaying time periods to a steady-state value. Thus, there are actually two regions of useful contrast in such a pulse sequence that may be added together in order to effectively double the signal to noise ratio without incurring a reduction in imaging speed. The authors acknowledge that with such a method, the dynamic range of signal is also increased since it is possible to generate DOCI values that are over the steady-state normalized value of 1.

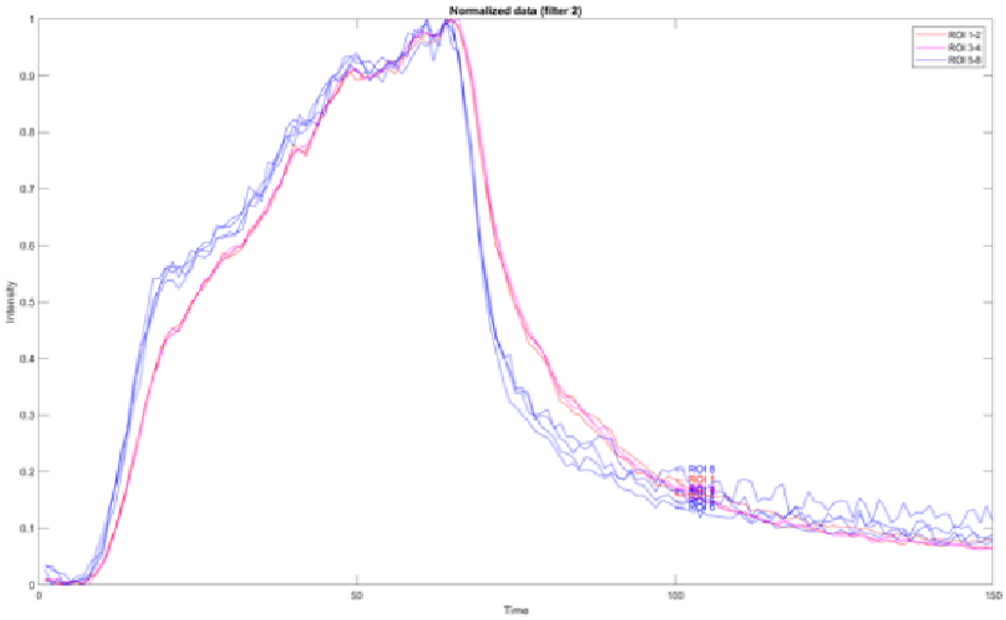

Figure 7-1: Rise, steady-state, and decay state for parathyroid versus adipose tissue.
The differences in not only the decay but also the rise of tissue fluorescence normalized to the steady-state can yield additional information to increase the overall contrast signal.

Two of the most significant roadblocks preventing widespread implementation of fluorescence lifetime imaging as a commonplace clinical imaging modality are the high system cost and the acquisition of a minimum photon count that permits calculation of fluorescence lifetime in a photon starved environment. This herein presented imaging method permits the use of inexpensive LEDs for illumination and significantly reduces the cost of a system that can generate fluorophore lifetime based contrast: without the use of any dye or exogenous contrast agent; at a surgically relevant large field of view; and with real-time feedback to the surgeon. This new method also permits simultaneous imaging during surgical resection without the need to turn off all the lights (and headlamps) in the operating room due to the increase in acquired signal. The production of such an imaging system may significantly improve outcomes for patients by minimizing the removal of normal functional tissue and assist in the complete and rapid removal of diseased

tissues. In summary, this method enables intraoperative imaging capable of rapid tissue differentiation by generating fluorescence lifetime contrast at large, surgically relevant fields of view.

7.3 Imaging Algorithm

The present method provides a doubling of the DOCI signal levels. This may permit simultaneous imaging during surgical resection without the traditional need to turn off all the lights (and headlamps) in the operating room.

The LED illumination permits a nearly linear rise, steady-state, and falling intensity (with respect to time on the nanosecond order) as shown graphically in Figure 7-2. Accordingly, fluorescence lifetime contrast is attainable when normalizing the sample fluorescence during *both* the rising and decaying time periods to a steady-state value. Thus, the present disclosure exploits two regions of useful contrast information, in that a pulse sequence may be combined in order to effectively double the signal and increase the signal to noise ratio by up to 40%, without incurring a reduction in imaging speed. According to the present disclosure, the dynamic range of signal can also be increased since it is possible to generate DOCI values that are as large as 2 compared to the original method capped at a value of 1.

Building on our prior patents(211,276–279), and referring to the imaging algorithm (Figure 7-2), the addition of a second term, namely (calibration image – excitation image) / (calibration image – background image) can be added to the first original term, (decay image – background) / (calibration image – background), in order to produce a total signal image, maximizing signal to noise and dynamic range, thus producing superior image contrast by harnessing additional signal from the targeted sample. The new complete equation is presented as Equation 10-1. The

subtraction of the background image accounts for ambient and stray light in the environment. The total signal image is a relative lifetime map of the target. Using values in the relative lifetime map, one can identify a boundary between a first group of cells or cell products having a first physiologic process and a second group of cells or cell products having a different physiologic process. The mathematical operations for each pixel that involve the sources of contrast can be provided by Equation 10-1, where x is the detector photon count (or proportional value to photon count) at each pixel.

$$\text{Signal per pixel} = \frac{\int_B^C f(x)dx - background}{\int_A^B f(x)dx - background} + \frac{\int_B^C f(x)dx - \int_A^B f(x)dx}{\int_B^C f(x) - background} \qquad \text{(Eq. 7-1)}$$

The array of generated pixel values serves as a lifetime map for the clinician and may immediately be presented in order to guide the physician in clinic or surgery. The clinician may infer physiologic and pathologic processes undergoing based on information presented by the system in order to screen patients, choose the best location for tissue biopsy, identify noncontiguous areas of pathology, incomplete resection, and faster margin analysis than that provided by conventional histopathology.

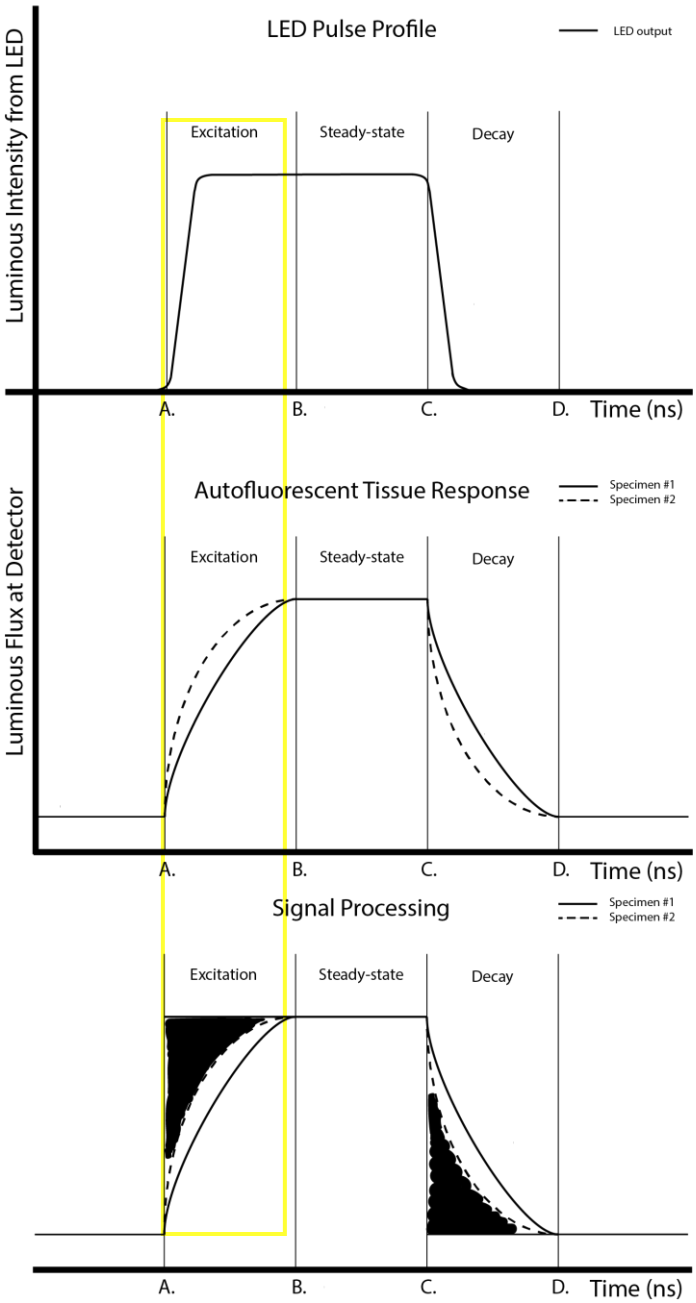

$$Conventional\ DOCI\ method: \frac{\int_C^D f(x) - background}{\int_B^C f(x) - background}$$

$$Second\ DOCI\ term: \frac{\int_B^C f(x)dx - \int_A^B f(x)dx}{\int_B^C f(x) - background}$$

x = detector photon count

Figure 7-2: Method of Electro-Optic Pulse Shaping for Increased Signal to Noise and Double the Dynamic Range.
The conventional DOCI method generates signal by integrating the area under the curve between C-D for either specimen #1 (longer fluorescence lifetime) or #2 (shorter fluorescence lifetime), respectively. The gold box highlights the new source of lifetime contrast (generated during sample excitation) that the presented method harnesses for up to a 100% increase in overall signal and ~40% increase in S/N without an increase in imaging time.

7.4 Alternate Embodiments

The principle methods for three alternate embodiments are detailed below:

First, there may be one detector used that acquires signal in two separate passes. During the first scan fluorescent intensity would be collected by a first gate in the interval A-B (Figure 7-2). The information would undergo analog-to-digital conversion and readout to the computer. A second gate would operate in the interval C-D, after which information would similarly undergo analog-to-digital conversion and readout to the computer.

Second, signal may be acquired simultaneously by two detectors operating in tandem that are properly synced via a timing pulse. This arrangement splits the two scan workload to permit simultaneous scan acquisition and circumvents a change in original image acquisition time.

Third, a field-programmable -gated-array may be used to integrate signal in real-time as it is acquired from the detector, perform mathematical operations necessary, and directly read out DOCI lifetime values that may be graphically displayed to the user. This arrangement will be limited solely by the rate of camera data readout to the computer. A benefit of this approach is integrated computation and direct readout of the final DOCI lifetime values to the computer. Thus, there would not be a need to perform simple mathematical operations on the computer and real-time lifetime imaging may become more feasible.

CHAPTER 8: SELECTIVE SPECTRAL ILLUMINATION FOR OPTICAL IMAGE GUIDED SURGERY

8.1 Background

In oncologic surgery patient prognosis depends heavily on complete tumor resection. Presently, however, surgeons often must rely on subjective assessments (e.g., palpation and visual appearance) during resection to distinguish abnormal from near normal tissues because there is no gold standard imaging technique for intraoperative image guidance(280). Among the many imaging modalities across the electromagnetic spectrum, optical fluorescence-based navigation systems are increasing in popularity because conventional imaging modalities (e.g., magnetic resonance imaging - MRI, positron emission tomography - PET , computed tomography - CT, ultrasound - US) are limited in their capacity to deliver sensitive, specific, real-time, and large field of view images to the surgeon(59,281). Illustrated in Figure 8-1, a new problem arises since these optical imaging tools utilize all or part of the visible electromagnetic spectrum (380-750nm) for either (1) tissue chromophore excitation or (2) quantification of chromophore emission during signal acquisition, while sharing this band of electromagnetic radiation with the high-energy broadband sources of illumination needed for the surgeon's vision.

Many emerging optical image guided devices may solve the unmet clinical need of intraoperative surgical guidance if they did not impede the normal clinical workflow in the operating room(262,282,283). Broadband sources of illumination in the operating room (e.g., fluorescent tube, xenon-arc lamp, incandescent light) interfere with fluorescence measurements in the visible spectrum and require significant dimming of the lights, or usually in order to increase desired signal to noise, completely turning off all lights in the operating room while the optical image based device is active. This action increases both the risk and cost of the surgery because of increased time that the patient is under anesthesia. For this reason surgeons may limit their use of these

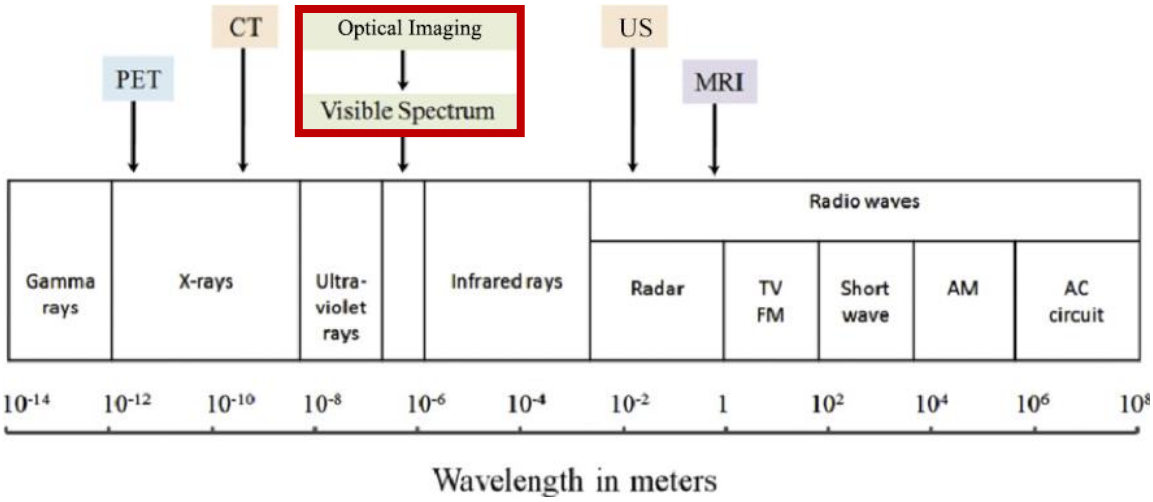

Figure 8-1: Medical imaging modalities plotted across the spectrum of electromagnetic radiation.
The red box highlights the overlap between the spectrum used by optical imaging modalities and the electromagnetic spectrum detected by the human eye (~380-750nm). MRI, magnetic resonance imaging; PET, positron emission tomography; CT, computed tomography; US, ultrasound.

optical navigation systems to just the most crucial junctions of an operation. In addition, even when the ceiling mounted operating room lights are off there is usually still a significant amount of stray light from the operating table spotlights and surgeons' individual head-mounted luminaires. During an operation there is a large cast of medical personnel (i.e., one or more surgeon's and trainees, anesthesiologists, circulating nurses, scrub nurses, and assorted medical students and observers) that are simultaneously working and prolonged complete darkness would unacceptably interfere with the ability of the team to deliver medical care.

Undoubtedly, a need exists for sharing the visible spectrum between the intraoperative lighting necessary for human vision and the overlapping spectra utilized by optical imaging devices that provide intraoperative surgical guidance. Existing solutions to this problem consist of: waiting while lights are off, placing excised specimens into a black box or transporting the specimen outside of the operating room, or using exogenous dye for contrast (e.g., Indocyanine green has

an excitation peak of 800nm) (284,285). Two notable examples of fluorescence measurement in presence of ambient light during surgery use a combination of pulsed sources of excitation with a time-gated detector for acquisition(286,287). Notably, those authors teach that in the surgical field “ambient light cannot be spectrally conditioned or controlled” (287). The surgical oncology community, therefore, still awaits an optimized optical technique that can provide relevant information about surgical markers by purely exploiting inherent differences in tissue.

8.2 Detailed Description

The solution to this problem of interference between operating room illumination with optical imaging devices during surgery is a method and system for selective spectral illumination that can create independent spectral bands of operation for optical image based tools while concurrently providing illumination for surgeons and medical personnel to continue delivering medical care. Current sources of operating room illumination operate with a broadband spectra (e.g., xenon arc lamps, fluorescent tubes, incandescent lights, halogen lights, and multi-color light emitting diodes

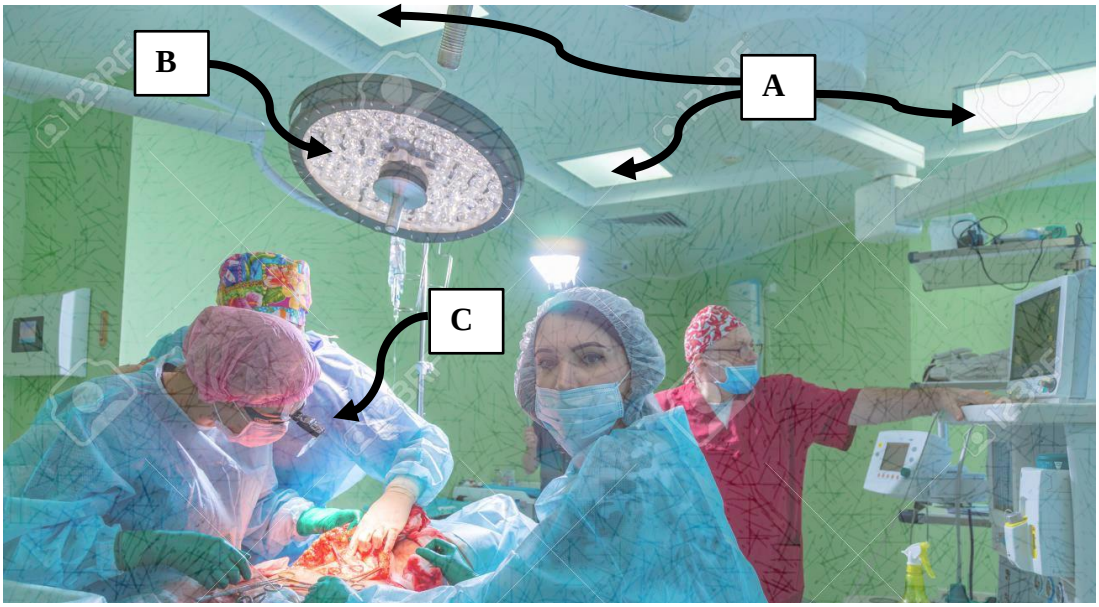

Figure 8-2: Application of selective spectral illumination in the operating room. **(A)** Ceiling mounted lights. **(B)** Movable boom mounted spotlight. **(C)** Head mounted luminaire. Image in public domain.

(LEDs). We propose a system of surgical illumination composed of multiple narrow spectrum emitting LEDs that are independently controlled and responsive to the requirements of many optical image-based devices during surgery. Preferably such a selective spectral illumination system would be installed in place of every light source in the operating room as illustrated in Figure 8-2.

Optical image based systems usually rely on exogenous or endogenous sources of contrast for image generation and usually rely on exciting/incident light and/or emitted/fluorescent light acquired in the visible spectrum. These devices or systems usually belong to sub categories of fluorescence-based imaging, intensity-based imaging, time-resolved imaging, hyperspectral imaging, optical biopsy, optical spectroscopy, image-guided surgery, or precision surgery. This system is useful during surgery for concurrent use of any imaging system wherein photometrics are influenced by conventional illumination in the operating room.

High-brightness LEDs are known to offer cost-effective, energy-efficient lighting solutions across the entire visible spectrum. Conventional methods of illumination produce a broad spectrum of light which has to be filtered out to make specific colors whereas multiple LEDs or multi-component LEDs may be modulated (usually in red, blue, green, and white) to produce different perceived colors or hues. Significantly, LEDs are also very efficient at emitting light of various narrow spectral bands. This method concerns multiple wavelength specific LEDs that are independently controlled to prevent spectral interference between visible illumination and medical devices operating in the visible spectrum. LEDs that emit at most wavelengths are commercially available but the necessary semiconductor material composition is known for production of LEDs that emit light with narrow spectra across the 380-750nm wavelength range as illustrated in Figure 8-3.

	Color	Wavelength [nm]	Semiconductor material
	Infrared	$\lambda > 760$	Gallium arsenide (GaAs) Aluminium gallium arsenide (AlGaAs)
	Red	$610 < \lambda < 760$	Aluminium gallium arsenide (AlGaAs) Gallium arsenide phosphide (GaAsP) Aluminium gallium indium phosphide (AlGaInP) Gallium(III) phosphide (GaP)
	Orange	$590 < \lambda < 610$	Gallium arsenide phosphide (GaAsP) Aluminium gallium indium phosphide (AlGaInP) Gallium(III) phosphide (GaP)
	Yellow	$570 < \lambda < 590$	Gallium arsenide phosphide (GaAsP) Aluminium gallium indium phosphide (AlGaInP) Gallium(III) phosphide (GaP)
	Green	$500 < \lambda < 570$	**Traditional green:** Gallium(III) phosphide (GaP) Aluminium gallium indium phosphide (AlGaInP) Aluminium gallium phosphide (AlGaP) **Pure green:** Indium gallium nitride (InGaN) / Gallium(III) nitride (GaN)
	Blue	$450 < \lambda < 500$	Zinc selenide (ZnSe) Indium gallium nitride (InGaN) Silicon carbide (SiC) as substrate Silicon (Si) as substrate—under development
	Violet	$400 < \lambda < 450$	Indium gallium nitride (InGaN)
	Purple	multiple types	Dual blue/red LEDs, blue with red phosphor, or white with purple plastic
	Ultraviolet	$\lambda < 400$	Diamond (235 nm) Boron nitride (215 nm) Aluminium nitride (AlN) (210 nm) Aluminium gallium nitride (AlGaN) Aluminium gallium indium nitride (AlGaInN)—down to 210 nm
	Pink	multiple types	Blue with one or two phosphor layers: yellow with red, orange or pink phosphor added afterwards, or white with pink pigment or dye.
	White	Broad spectrum	Blue/UV diode with yellow phosphor

Figure 8-3: LED semiconductor materials for unique spectral emission(288).
Recent advances in materials and methods for LED manufacture have resulted in the production of LEDs with narrow band emission ranging across the entire visible spectrum. UV LEDs are also increasing maximum output intensity, and are currently in very high demand due to the COVID-19 pandemic(289).

8.3 System and Methods

8.3.1 Suggested Components

The parts and assembly of an embodiment of the system are illustrated in Figure 8-4. In a proposed embodiment, an integrated circuit of appropriate specification is manufactured to drive multiple (at least two) suitably doped semiconductor heterostructures (Light emitting diodes – LEDs) to emit electromagnetic radiation at different wavelengths within the visible spectrum. The light emitting diodes that emit light at unique wavelengths within the visible spectrum are over 5mW power and may consist of an array of various size and number according to room and procedure requirements while still powered by the same power source and drivers. An LED driver of suitable design independently controls the current and voltage to each LED group. Multiple LEDs that emit light in the same wavelengths will be considered an LED group. A unique feature of this circuit is permits the illumination system to tailor its spectral emission to the requirements of certain medical devices that are influenced by 380-750nm light. This circuit can receive power from a standard electrical mains source or a battery of sufficient capacity and may be controlled with a switch or similar controller.

8.3.2 Method

During normal illumination the LEDs of all wavelengths are active and overall the system will emit in a fashion analogous to a broad spectrum device. When an optical imaging device is used that requires a portion of the visible spectrum for its operation, the system will dim or turn off the individual LEDs that emit light in the overlapping wavelengths required by the medical device. Thus, the wavelengths of illuminating light emitted from this light source that would overlap with the medical device will cease and a unique spectral band will be created for operation of the optical imaging device. Concurrently, light will still be emitted from the system in all of the other visible wavelengths that are not used by the medical device in order to provide illumination for the

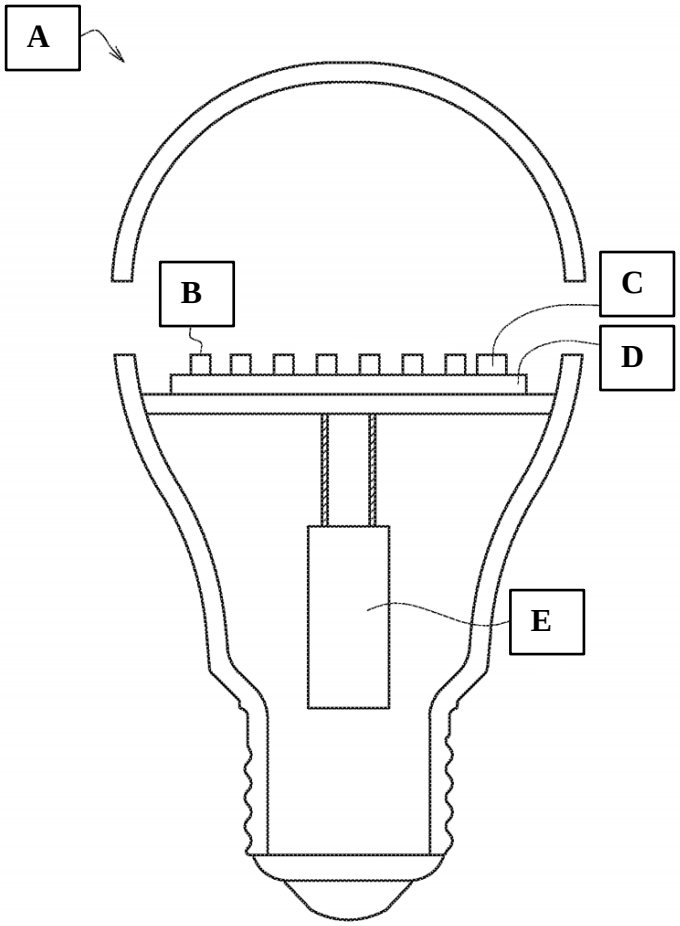

Figure 8-4: Schematic of an embodiment for the method and selective spectral illumination system.
(A) Selective spectral illumination device. **(B)** LED. **(C)** LED of different spectral emission. **(D)** LED driver. **(E)** Integrated circuit.

surgeon and medical team. When the optical imaging device is no longer used the system can resume emitting light from LEDs of all wavelengths. In a simple design the different modes of operation of the illumination system may be controlled by a switch.

8.4 Principles of Operation

In this example the method and system function are described in relation to the specific technique of dynamic optical contrast imaging (DOCI), but may be used in conjunction with any optical

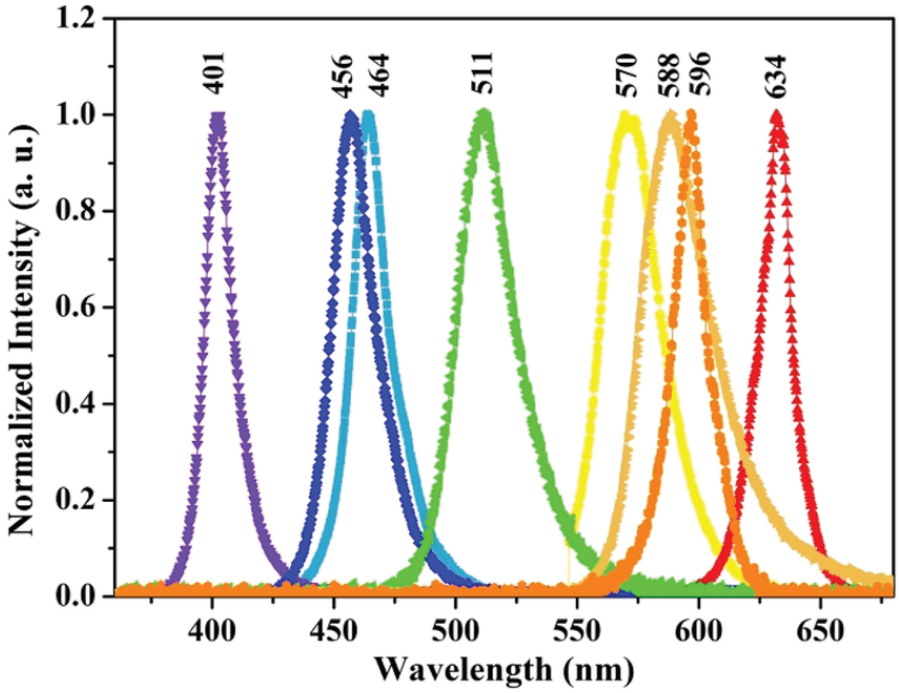

Figure 8-5: Standard emission spectrum of illumination system.
LEDs of all individual wavelengths are delivering light in an analogous fashion to a conventional broad spectrum source of illumination (Thorlabs, USA).

imaging technology. In brief, dynamic optical contrast imaging differentiates tissue types on the basis of detected fluorescence from endogenous tissue chromophores excited by 350-400nm wavelength light(212,228). During surgery when the DOCI system is not in use the presented system will provide illumination by using LEDs of every visible wavelength, as illustrated in Figure 8-5.

When the surgeon desires intraoperative visual guidance from the DOCI system they would switch the output of the presented system and only the LEDs that emit light outside of the 350-400nm wavelength range will be active in order to prevent interference, as illustrated in Figure 8-6.

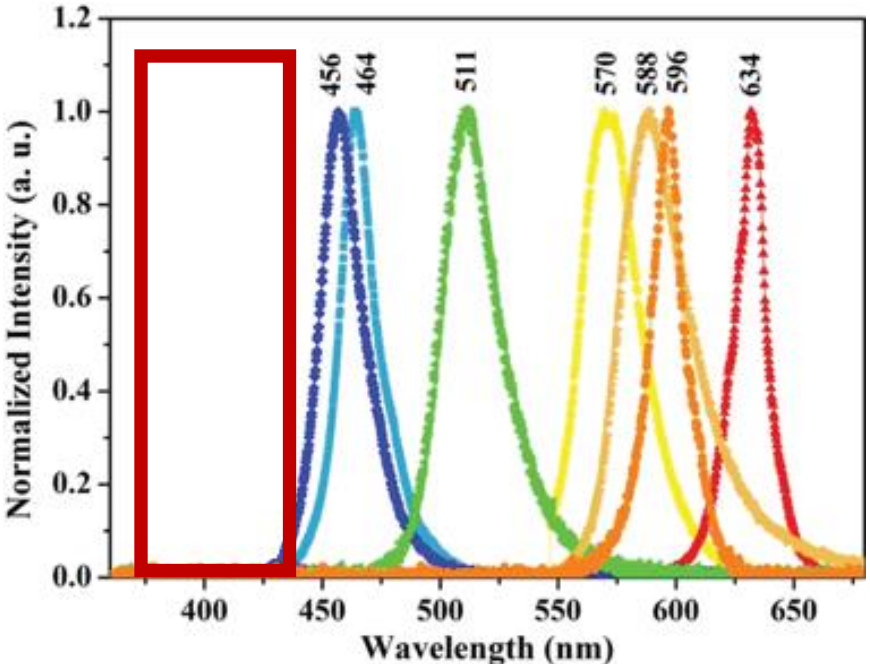

Figure 8-6: Selective spectral emission of illumination system.
The DOCI system requires exclusive use of the 350-400nm spectral band and the LEDs that illuminate the surgical field that operate in this spectral band will turn off to avoid interference with the DOCI system. All other LEDs that operate at other wavelengths of the visible spectrum will continue to provide illumination in the operating theater. The red box highlights that the 401nm LED is not producing light during DOCI system use.

8.5 Alternate Embodiments

LED Number, Type, and Arrangement

- Either single, independent LEDs or single multicomponent LEDs may be used for illumination.
- The individual types of LEDs may or may not overlap in spectral emission. The key function is that there should not be any spectral overlap between an illuminating LED or a spectral band used by a medical device.
- LEDs may be arranged in an array, where either multiple LEDs that emit light of the same wavelength are arranged together in groups or where LEDs that emit light of different wavelength are arranged together in groups.
- The LEDs or LED groups may be arranged in serial or parallel configuration.

- The number of LEDs used must be at least 2 if both LEDs emit unique wavelengths of light or 1 multicomponent LED that can emit unique wavelengths of light.
- The number of unique spectral bands and number of LEDs in each spectral band may vary according to application and parameter requirements.
- Either each LED or each group of LEDs may have various filters attached or positioned between the LED and the desired region of illumination in order to create unique spectral groups or to sharpen the spectral emission limits of individual LEDs.
- Emission filters may also be placed onto the LED to further reduce the FWHM emission range of each LED, respectively.
- For higher power LEDs or maintenance of color the LEDs may need to be cooled by a heatsink, fan, or other means of dissipation of energy to prevent heating of the LED.

Light Sources For Illumination

- Any source of illumination may be used (Laser, Laser-Diode, Diode-Laser, LED, Halogen lamp, Incandescent light, Xenon-arc lamp, Fluorescent tube, etc) if there is an appropriate filter positioned after the light source or a number of filters positioned in front of the light source that are controlled manually or via a motorized mechanism.

Different Light Source Locations

- The illuminating light source may be in or on the operating room ceiling, any boom or spotlight, surgical headlamp, or mechanical device itself (e.g., Da Vinci Machine by Intuitive Surgical Inc).

Light Mode Switching And Automation

- The switch between illumination modes may be automatic through the use of a wireless or network communication module. In such a case the spectral requirements of respective medical imaging devices may be captured by associating a unique RFID device or another electronic device that has a traceable unique identifier. Individual optical imaging devices may be assigned with a unique identifier and may communicate with the selective spectral illumination system to form a dynamic wireless network, such as a Zigbee network. A database may be provided to maintain information about individual device spectral requirements and other information. Such a database could be stored locally in memory or accessed through a network remotely.
- The mode of illumination may automatically switch specifically at the times when the imaging device requires a portion of the visible spectrum. The latency in communication between the device and the illumination system would need to be accounted for. There may also be a need for a timing device connected to the integrated circuit controlling the LED driver and LED in such a situation.
- An automatic functioning would provide ease-of-use for a complicated system. Also incorporates several complicated control schemes and paradigms. Networked digital communication and separate power and voltage control circuits that provide control to individual LEDs or LED arrays. If there are multiple systems or control systems then they must be compatible and work together.

Compensation Of Remaining Unique Spectral Bands For Selective Illumination During Optical Imaging

- The intensities of light from the remaining unique LED wavelengths emitted that do not interfere with the optical imaging device may be controlled in a way to generate the most similarly perceived color as when illuminating in a general broadband mode. The most

similar color would be determined by the closest distance in the CIELAB or CIEXYZ or sRGB or ICtCp or CIE 1931 color-space that is achievable with the remaining LEDs.

- Any possible perceived color from the utilized LEDs may be created for the respective purpose or environment.
- Memory may be used to store many of these preset color configurations.

Nonuniform Function

- The output of multiple connected illumination sources may be modulated to produce a number of unique zones or uniquely controlled zones in the operating room.
- LED brightness at different emitting wavelength is driven at appropriate power to generate uniform efficacy considering the variable luminous efficiency of the human eye.

CHAPTER 9: CONCLUSIONS AND FUTURE DIRECTIONS

9.1 Summary Of Achievements

There exists a pressing medical need for non-invasive optical tools to help surgeons intraoperatively identify tissue and determine precise tumor margins. Achievements from this work include:

1. The first clinical use of DOCI to produce relative lifetime tissue maps at an unprecedented six-by-six cm field of view.
2. Results from clinical translation and use that demonstrate the capacity to resolve statistically unique spectral features for individual states of disease before tissue biopsy. Statistically significant results from malignant, premalignant, and benign tissue suggest the system may be valuable as a screening tool for patients presenting to the clinic.
3. Through pilot study, a new clinical application of Dynamic Optical Contrast for Mohs micrographic surgery was presented. Early In vivo results suggest relative lifetime images generated can provide significant contrast between basal cell carcinomas and surrounding uninvolved skin.
4. Following assessment of clinical obstacles and system improvement, a new DOCI system was tested with ex vivo resected HNSCC specimens and validated with histology. The relative lifetime images demonstrated the capability of the system to produce useful contrast in order to significantly differentiate HNSCC from both hairy skin (keratinized stratified squamous epithelium) and oral mucosa (non-keratinized stratified squamous epithelium) in ex vivo conditions.

5. Statistically significant DOCI contrast was produced in ex vivo parathyroid at unique spectral bands. The contrast from our novel system was supported through two-photon microscopy.
6. The DOCI measurements were standardized using reference dye and a commercial two-photon system to determine that each 0.01 increment in relative lifetime value equated to 0.2127 ± 0.0206 (ns) absolute fluorescence lifetime change. The standardization of system values and the linearity of the measurements suggest this method may be used for true fluorescence lifetime measurements. These results and methods permit system calibration over time and also between different systems, which would be necessary in a future multi-site clinical trial of the system.
7. An improved method (patent pending) for Dynamic Optical Contrast Imaging incorporating useful spectral contrast during illumination rise for up to a ~40% increase in signal-to-noise and a 100% increase in system dynamic range (0-2).
8. A new method and system (patent pending) for spectrally controlling surgical illumination to permit intraoperative application of fluorescence sensing techniques in real-time, thus circumventing the need to turn off lights and cause a delay in medical care.

Our tool generates contrast through relative measurements of autofluorescence decay rates (lifetime) from tissue and thus does not require dye or injection of contrast agents. Furthermore, as opposed to intensity based approaches, our measurements depend on the intrinsic properties of tissue and thus provide a robust signal insensitive to inhomogeneous illumination and irregular tissue contours. Although currently DOCI values are only an approximation to the complex nature of heterogenous fluorescence lifetime decay, the method permits generation of meaningful contrast between neoplastic and surrounding normal tissue that may aid clinicians and lead to improved patient outcomes. Finally, the results regarding clinical performance of Dynamic Optical Contrast Imaging should be considered as preliminary and not be used for medical diagnosis or

treatment before randomized large-scale clinical trial and appropriate regulatory and medical approval.

9.2 Recommendations and Future Directions

9.2.1 Regarding Hardware

Attachment of endoscope to DOCI system:

The confines of the oral cavity require a small diameter, long length imaging lens that can reach recesses of the mouth while maintaining a reasonable standoff between patient and focal plane array. DOCI contrast generation allows for tens of nanoseconds long illumination pulses and thus tolerates pulse dispersion from endoscopic fiber coupling. Thus, development and attachment of an endoscope to our DOCI system may permit non-invasive imaging of lesions inside the oral cavity and near the base of the tongue. Simulations and prototypes have already been developed for this purpose.

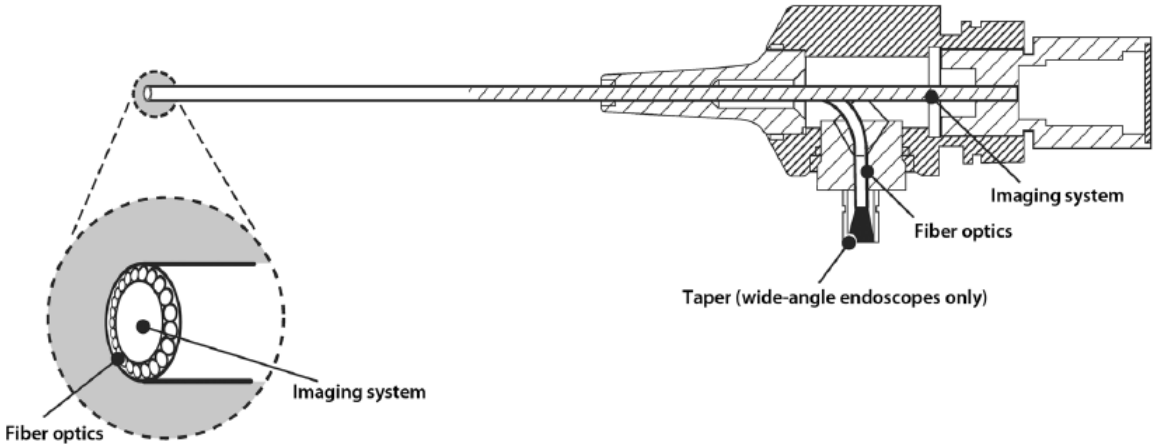

Figure 9-1: Illumination geometry of a rigid endoscope.

Endoscopes are medical devices that permit deep inspection of body cavities otherwise inaccessible. They may be rigid or flexible, and function by first illuminating a target and then relaying an image back to a detector (illustrated in Figure 9-1 (290)).

With the current approach and instrumentation, it is not feasible to clinically access and image regions in the dorsal tongue, pharynx, and larynx. Therefore, adopting DOCI methodology in telescope optics is a crucial step to enable intraoperative use of DOCI technology in deeper regions of interest. Successful preliminary models and prototypes have been constructed in order to open the possibility of applying this technology in endoscope optics (Figure 9-2). In addition, a 4 axis translational stage (Figure 9-3) has been constructed that permits flexible orientation of the system in 3D space.

Endoscopes with integrated LEDs are not yet widely available. In medicine. endoscopes usually rely on an external light source that is coupled via a fiberoptic cable.

In our prototypes, illumination modeling between the LED and the light guide using Light Tools (Synopsys) revealed a significant amount of light is lost at the interface between the LED lens and the light guide. A properly designed reflector may decrease scattering and significantly

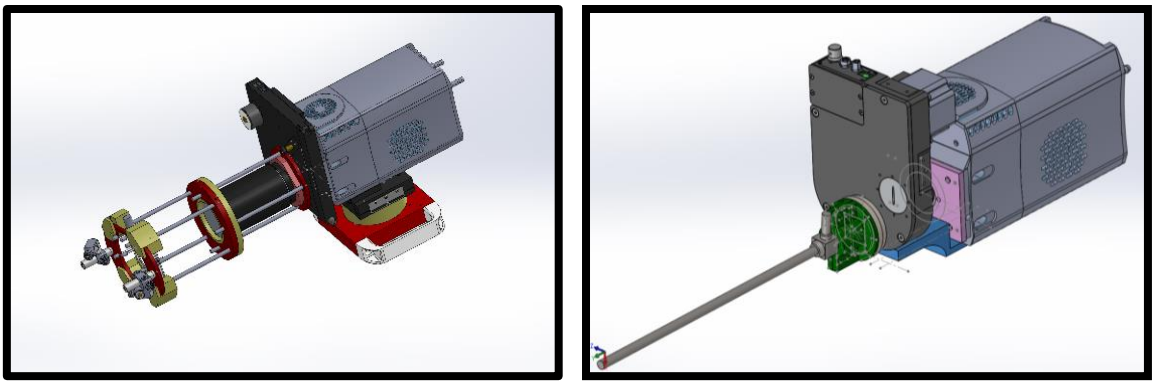

Figure 9-2: Complete system model with endoscopic attachment and new filter wheel. (Left) Original system design; (Right) New endoscope coupled prototype to with ten position filter wheel. (Adaptor in green 3D printed by Yong Hu).

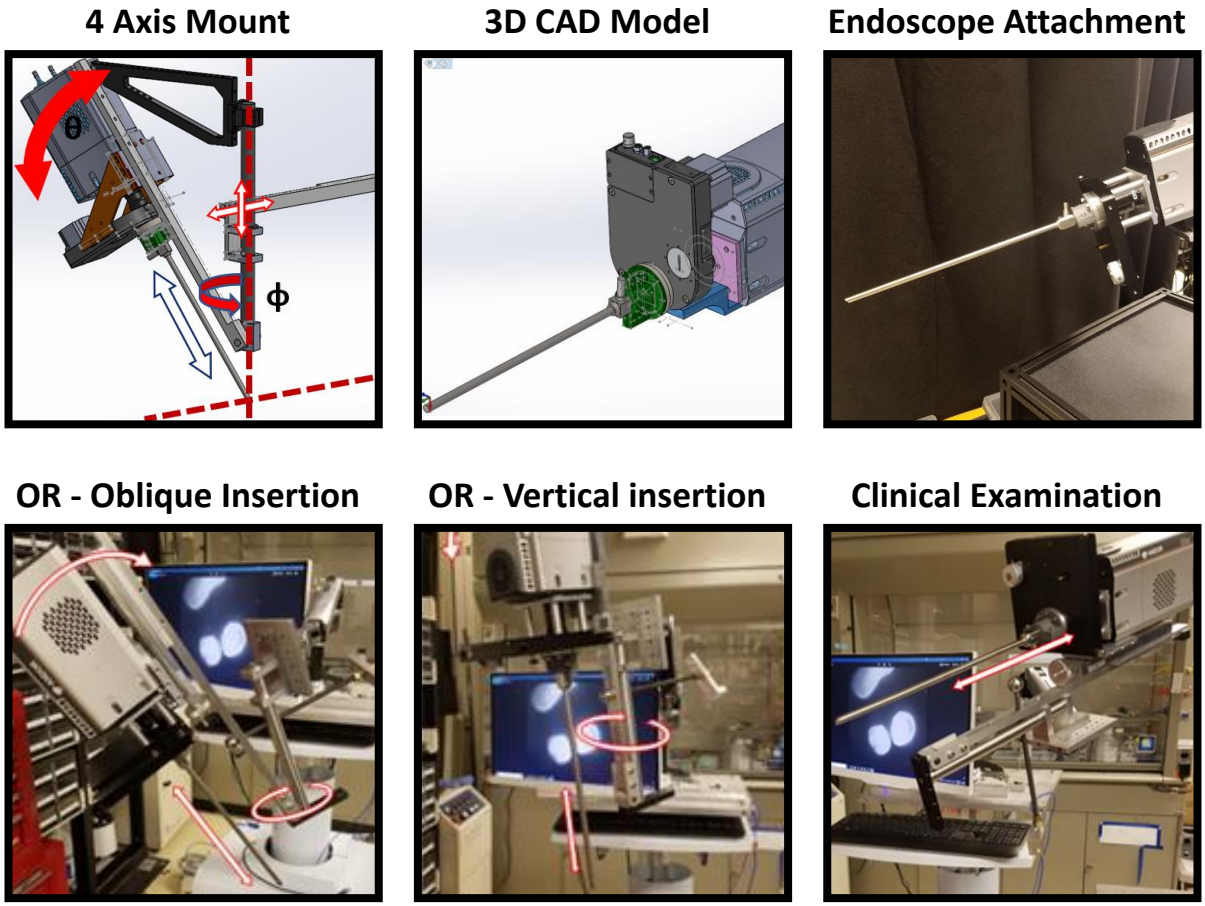

Figure 9-3: Endoscope attachment and 4 axis translational mount.
Design and construction of endoscope stage.
Coarse X and Z movement (Φ, range ± 75º) and (Θ, range 0º - 70º),

increase in light intensity from the existing LED. In literature the use of an endoscope with 15mW/cm^2 reported no adverse tissue effects (205). Given this finding there is also room to further increase the power from the LED.

9.2.2 Regarding Gender Specific Differences In Studied Patient Population

Gender specific differences in oral screening:

Additional aims for future research include investigation into gender differences present in the detectable causes, pathophysiology, and screening of oral cancer between sexes and subsequently the direct incorporation of gender specific image classifiers for patient screening. Gender differences can underlie different exposures, risk factors, pathology, and responses to treatment, yet due to the historically male predominance in oral cancer, the disease has minimally been studied in women(291–293). Although the incidence of most head and neck cancer is declining, the there has been a marked increase in oral tongue cancers in young adult females with no known risk factors. Women with OSCC are less likely to use alcohol and tobacco yet the incidence in women has been steadily increasing over the past two decades(294–297). In addition, recent investigations are beginning to uncover statistically significant differences between men and women diagnosed with OSCC for almost all investigated socio-demographic, clinical, and pathological variables(298). Existing theories concerning sex specificity include estrogen deficiency, elevated fasting glucose, and HPV status as having a gender specific role in older females, yet the causative agent to the current increase in diagnosed young-adult females remains to be investigated(299–302).

The earliest known indicators of developing premalignant and malignant pathology are oral mucosal cyto-morphological changes at the nuclear and structural tissue scale(303–305). DOCI is poised to develop the first quantitative and noninvasively screen based on measured intrinsic fluorescence lifetime as a proxy for the morphologic and metabolic state of the inspected tissue. This research poses to provide valuable insight into the spectral signatures of the immediate tumor microenvironment and enables us to construct a framework for evaluating the earliest detectable hallmarks of disease pathophysiology. Furthermore, our experiments have already begun to produce valuable data that will enable the development of unique image classifiers (as

recently validated in application to OSSC histologic analysis(306)), unique screening regimens, and possibly earlier and specialized treatments.

The introduction of a quantitative screen with prognostic markers would be clinically useful in delineating the aggressiveness of these tumors and thus in tailoring the best treatment strategy for each patient(307). Our tool is one of the first tools that could identify such prognostic markers via intrinsic tissue measurements. Future efforts may be directed towards refining this instrument to better screen men and women, and generate further leads worth investigating regarding the rising incidence of oral cancer in women.

Gender specific differences in endocrine surgery:

This tool may also be applied to study gender differences attributable to the development of primary hyperparathyroidism, and creation of gender specific image classifiers may be generated to uniquely benefit women in the treatment of their disease.

Primary hyperparathyroidism is more common in females for reasons not readily apparent(308). Differences between the sexes pervades all clinical experience in medicine, leading to different exposures, risk factors, pathology, and responses to treatment, yet the morphological auto-fluorescence lifetime spectra of in vivo parathyroid glands has yet to be investigated. Meanwhile, literature reports that high body mass index and female gender are associated with an increased risk of nodular hyperplasia of parathyroid glands(309). In addition, a notable finding underscoring hormonal gender related differences in the pathophysiology of disease is the recent publication that exogenous female hormone use is associated with nearly a twofold risk reduction in female head and neck neoplasia(310). Accordingly, we aim to investigate the effects of the hormonal milieu in our ongoing research regarding the structural presentation and detection of disease in women.

Women uniquely experience menarche, pregnancy, and menopause, and also differ in their presentation of hyperparathyroidism in comparison to males. Male patients more often present without symptoms, present with vitamin D deficiency, and have larger parathyroid glands(311). Women are affected twice as often as men; however, this ratio varies from close to equal in patients younger than 40 years to an almost 5-fold excess in patients older than 75 years(312–314). A quarter of cases of primary hyperparathyroidism occur in women during the childbearing years, yet literature regarding the disease during pregnancy is scarce(315). A strongly justified future aim may be to fill the void in existing literature concerning the spectral and morphological profiles of hyperparathyroidism during these time-periods that are unique to females.

Additional strengths of our approach are the preservation of positional information and the tumor microenvironment during imaging. Intratumoral heterogeneity is widely recognized as a critical factor in nearly all human solid tumors(316–318). Accordingly, parathyroid adenomas are comprised of distinct cellular subpopulations of variable clonal status that exhibit differing degrees of calcium responsiveness. The recent emergence of these biochemically defined subclasses of parathyroid tumors suggests a previously unappreciated degree of functional heterogeneity in PHPT(319). Distinct populations have been detected from single cell fluorescence, and we will investigate if this translates into tissue-wide detectable differences(319). Our non-invasive tool can probe the biochemical profile of the parathyroid gland and surroundings to detect differences attributable to hormone levels, fat localization, and the recognition of unique anatomic relationships to improve gland localization.

This need may be addressed by creating adequately powered female cohorts to enable statistical investigation regarding tumor heterogeneity from our acquired multidimensional spectral data in regards to differences in patient sex. The lack of live intraoperative imaging tools for real time

human tumor tissue identification remains a significant translational challenge(319). We are proceeding to implement our tool in the clinic and call attention to the value in a future database (and tool) that incorporates hormonal gender specific differences in its function from the earliest implementation in surgery.

9.3 Medical Device Development in Academia

Basic science research can elucidate the rich complexity of the physiology and pathophysiology of oral cancer. The gap between the knowledge gained from blue sky research and direct applications to improve patient care, however, is substantial. Medical device development, on the other hand, bridges basic science to advancements in treatment that streamline the transformation of abstract pathophysiology into clinically-relevant measurements and benchmarks.

Device development in academia is incredibly high-risk and much of the difficulty is in filtering out which projects to advance from the many existing options. Identifying projects that will succeed is difficult, however, a thorough concept design process can help select projects with potential. The critical path in the development of an idea to a product includes: invention and patent application, basic research, product design and development, manufacturing, pre-clinical and clinical testing, regulatory review, and commercialization.

The first step in developing a device is identifying a clinical problem and the associated unmet need. When identifying an unmet need, it is critical to clarify the stakeholder and a specific measurement of success, while maintaining a broad statement of purpose. After creating a list of unmet needs, a rigorous screening process should be performed to evaluate a primary need for feasibility, efficacy, and other relevant parameters (320). For example, an unmet need in OSCC

cancer treatment might be stated as: A safe and effective means for identifying the presence and location of abnormal tissue in an oral lesion, with the production of real-time results during screening and tumor resection.

After a primary need has been identified, concept generation is a process that should be explored in an iterative process. Brainstorming of multiple concepts should be performed, then rated according to a set of parameters and outcome measures. Once a top concept has been selected, modelling and evaluation of prototype performance should be measured against pre-defined needs and outcome measures. A selection matrix can be created to calculate the risks and benefits associated with each concept. While many concepts show promise to address a clinical problem, it is important to consider feasibility, including: cost of production, complexity of design, implementation at multiple levels of the healthcare infrastructure, and the ratio of benefit relative to the amount of time and energy invested.

Once a clinical problem has been selected, multiple iterations and stages of defining a primary need, brainstorming concepts, selection of concepts, and prototyping can be performed until a pre-clinical prototype has been developed that meets pre-determined benchmarks. The technology may then undergo a file for patent protection given that the developer's intellectual property adds the necessary value to an emerging technology that is essential for future investments of resources necessary for clinical trials. Once a preliminary stage device is constructed it must be tested in a preclinical setting (often a small animal model) to establish proof of concept. In a specific example related to imaging, this includes viable results, image generation, and validation of contrast mechanism. If the device proves efficacious in pilot studies, the product is designed (i.e., portability and spatial dimensions) with considerations of: use in the clinical setting (prior to clinical trial), improvement upon current standards of care, no substantial increase in patient harm, consistency of contrast mechanism with human results, and a clear benefit to

patients. Meeting these conditions may qualify the device for FDA clearance for potential commercialization and widespread use. The review process, however, may take upwards of several years and many devices fail to meet these criteria and provide limited or insufficient data.

Not only is it necessary to produce new healthcare products and to establish their proper use in the correct patient population, it is also necessary to create policy changes, reimbursement alterations, and shifts in healthcare paradigms before translation of the device is fully realized in clinical use. One reason that emerging imaging modalities are such an attractive avenue for device development is that the necessary challenges in policies and protocols to overcome to ensure proper use is considerably decreased when compared to invasive tests.

9.4 Center for Advanced Surgical and Interventional Technology at UCLA

Translational research for new medical devices and diagnostics encompasses aspects of basic science and clinical research, requiring a multi-disciplinary team with access to unique resources (321). Traditionally, academic laboratories value novelty over factors relevant in industry, namely: robustness of performance, feasibility of manufacturing, scalability, avenues for reimbursement, and commercial potential. An ideal laboratory integrates engineers and medical doctors to design novel technologies that are immediately available for direct use in patient care.

The Center for Advanced Surgical and Interventional Technology (CASIT) is an interdisciplinary research center in the David Geffen School of Medicine at UCLA with satellite laboratory facilities throughout the UCLA campus. CASIT was founded over two decades ago as a program to research, develop, and teach advances in medical and surgical interventional technology through collaboration between the schools of Medicine and Engineering.

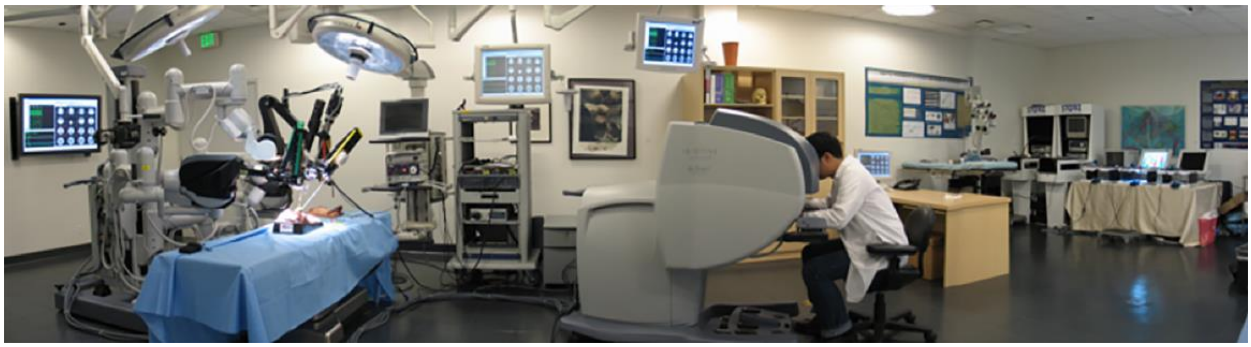

Figure 9-4: Center for Advanced Surgical and Interventional Technology dry lab at UCLA. Collaborative efforts between clinicians and engineers have led development of an integrated surgical suite with robotic surgical simulators, intraoperative ultrasonic imaging, and diagnostic MRI-ultrasound fusion devices.

The goal of CASIT is to apply these multidisciplinary resources to advance medical and surgical interventional technologies, including tele-mentoring, tele-surgery, medical simulation, robotic surgery, surgical training, and image-guided and minimally-invasive medical and surgical interventions. Over the last three decades, medicine has increasingly relied on engineering for the terrific advances that have been achieved in interventional technologies. Interdisciplinary teams are critical to the successful design of interventional systems, instrumentation, and tools. CASIT provides a unique facility (Figure 9-4) where engineers, basic scientists, and clinicians can interact and develop tools and procedures for a broad range of interventional therapies. CASIT takes advantage of the depth of engineering, basic science, and medical expertise that resides on the UCLA campus, and provides a focal point for the exchange of ideas, creation of new intellectual property, development of new instrumentation and procedures, and their transition to industry.

9.5 Commercialization

While translational science encompasses a range of modalities, including small-molecules, biologics, instruments, surgical or clinical methods, and behavioral changes (e.g., diet, exercise,

smoking cessation), this chapter focuses specifically on medical device development and imaging. Historically, the decades of innovation in the semiconductor industry (as characterized by Moore's law) have tremendously impacted scientific progress and medical care (322). Indeed, the iterative improvements in computer hardware, sensors, and detectors with advanced capabilities have resulted in the short life-cycle of these products. Furthermore, the subsequent decrease in their cost has led to a profound increase in the availability of electronic devices for medical purposes (323). Currently, there are a remarkable amount of next-generation imaging, sensing, diagnostic and measurement tools in development with the aim of providing additional information to the doctor for making decisions (324). As an example, imaging devices can augment a physician's ability to detect and treat diseased tissue. Imaging systems may be integrated into several different phases of medical treatment since the detection and differentiation of tissue pathology is important during early patient screening, surgery in the operating room, and while checking for recurrence of disease. In brief, medical device development is an exciting field because it links basic science research with improved patient outcomes.

The ultimate translation of new technology for clinical use is a meticulous and costly process that requires multiple levels of verification and validation of scientific merits, safety, and efficacy. Growing regulations by the FDA have increased the time and costs associated with achieving this goal (321). A movement of medical innovation is underway despite increased regulations because investors, biotech hubs, and private companies have expanded the available funding for translational science (325). The funding and support required for clinical translation can reduce the time from idea to implementation and is stimulating the development process.

The FDA outlined a model of the device development process in five stages: (1) medical need identification and concept design, (2) prototype development in a preclinical context, (3) safety

and efficacy evaluation in clinical trials, (4) FDA review, and (5) reimbursement assignment (326). In this model, devices are invented to fill an unmet need and improve patient care. Each stage of the development process further refines the original concept and brings the novel discovery one step closer to the clinical context in which it will be used.

APPENDIX A: SUPPLEMENTARY MATERIAL AND FIGURES

A1. Malignant Melanoma

In vivo

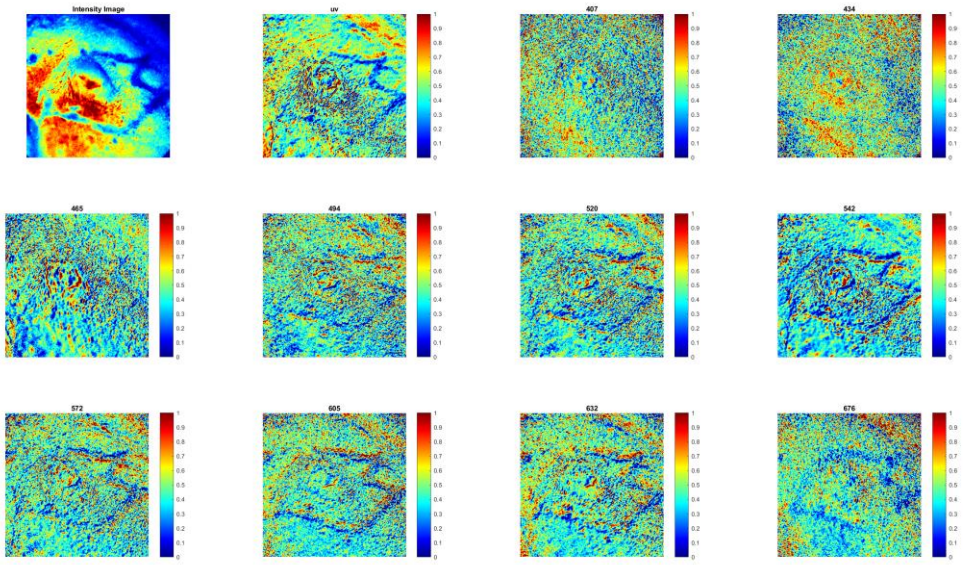

Ex vivo

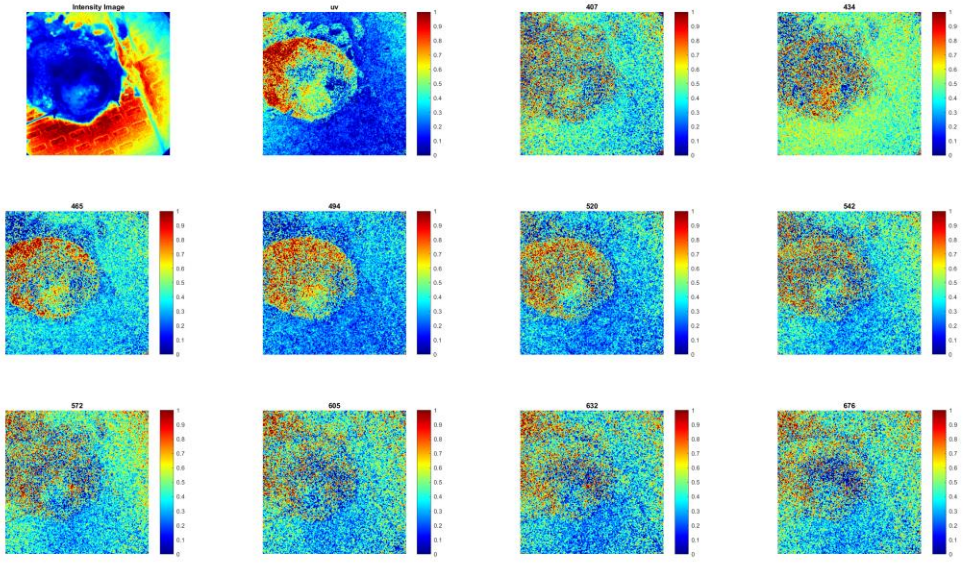

A2. Lichen Planus

In vivo

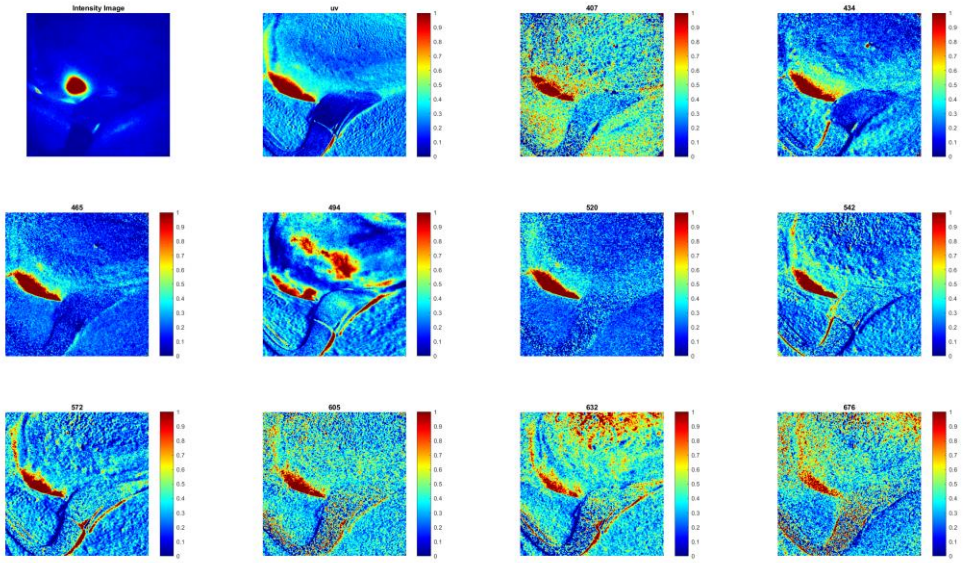

Ex vivo (external side with pathology)

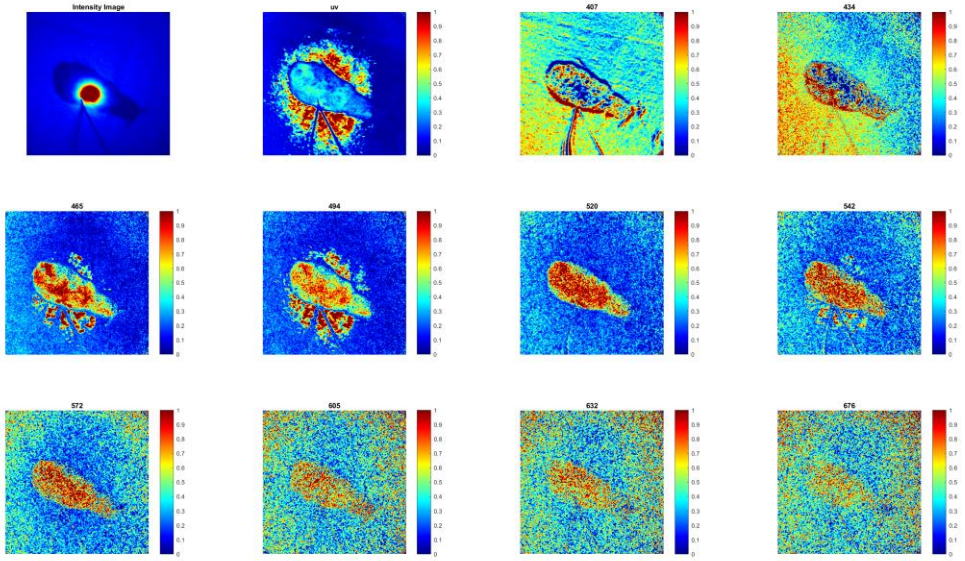

Ex vivo (medial side facing healthy tissue)

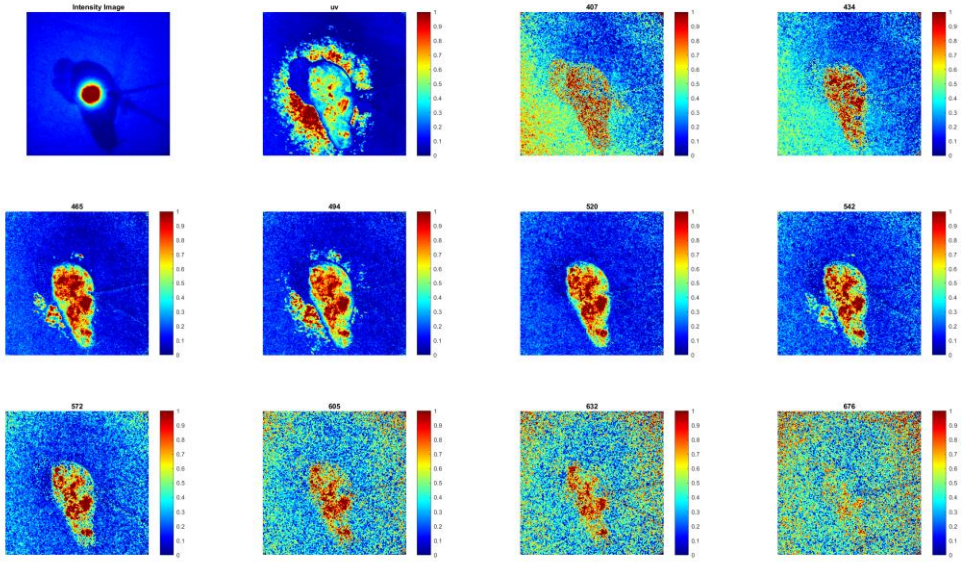

A3. Squamous Cell Carcinoma

In vivo

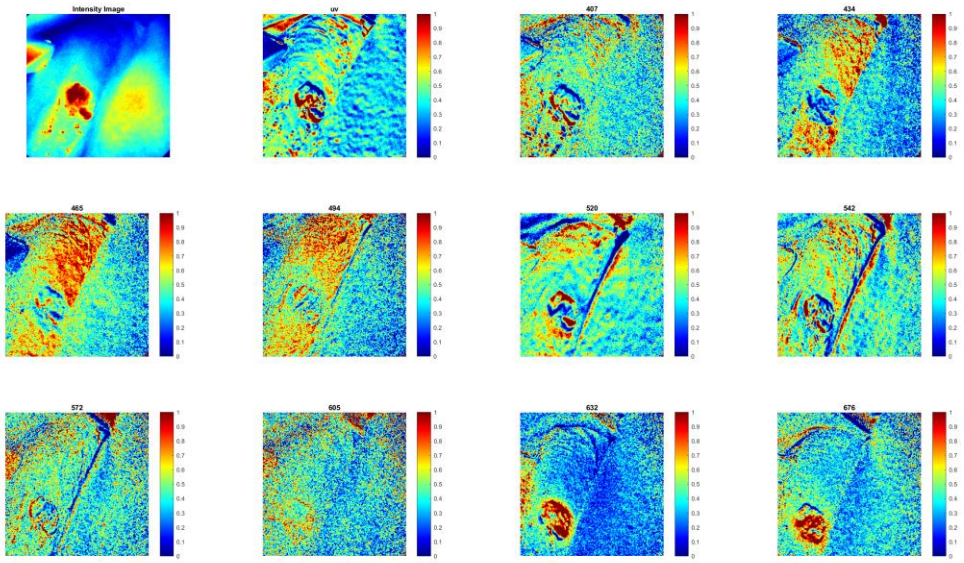

A4. Basal Cell Carcinoma During Mohs Surgery

In vivo

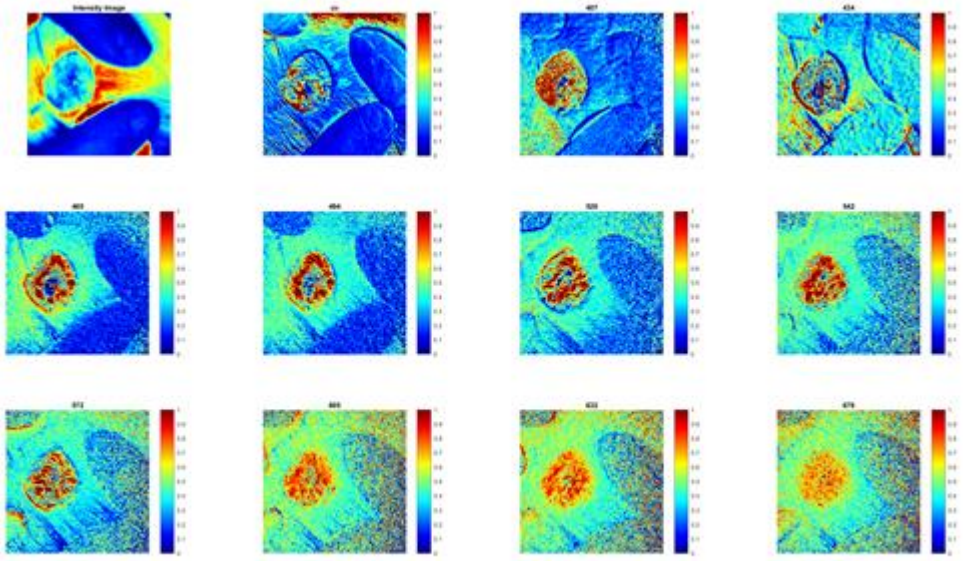

Ex vivo

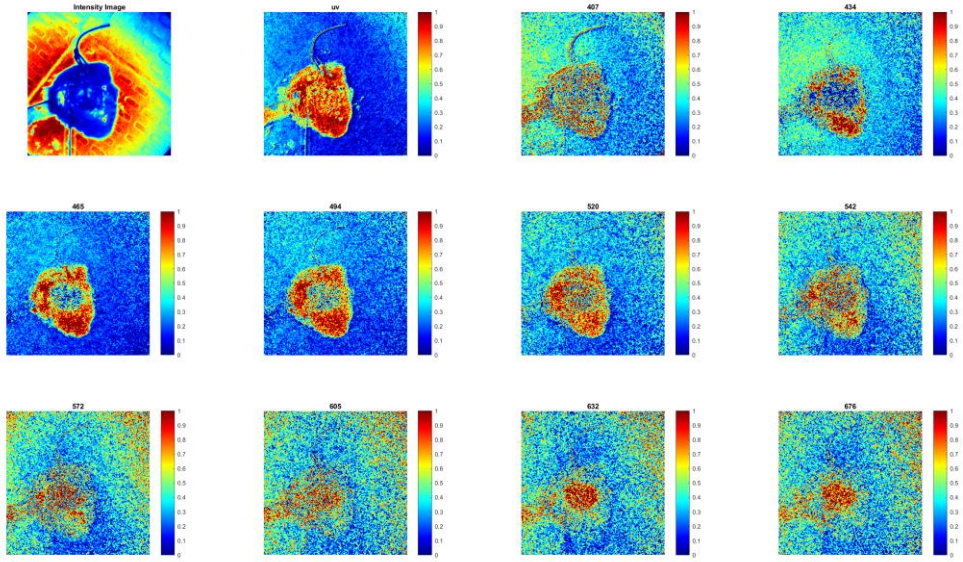

REFERENCES

1. Gibbs-Strauss SL, Rosenberg M, Clough BL, Troyan SL, Frangioni JV. First-in-human clinical trials of imaging devices: an example from optical imaging. Conf Proc IEEE Eng Med Biol Soc. 2009;2009:2001–2004.

2. Aliperti LA, Predina JD, Vachani A, Singhal S. Local and Systemic Recurrence is the Achilles Heel of Cancer Surgery. Ann Surg Oncol. 2011 Mar 16;18(3):603–7.

3. Hinni ML. Head and neck surgical reconstruction. Curr Opin Otolaryngol Head Neck Surg. 2013 Aug;21(4):303–4.

4. Ho AS, Kraus DH, Ganly I, Lee NY, Shah JP, Morris LGT. Decision making in the management of recurrent head and neck cancer. Head Neck. 2014 Jan;36(1):144–151.

5. Goodwin WJJ. Salvage surgery for patients with recurrent squamous cell carcinoma of the upper aerodigestive tract: when do the ends justify the means? The Laryngoscope. 2000;110(3 Pt 2 Suppl 93):1–18.

6. Siegel R, Ward E, Brawley O, Jemal A. Cancer Statistics , 2011 The Impact of Eliminating Socioeconomic and Racial Disparities on Premature Cancer Deaths. CA Cancer J Clin. 2011;61:212–36.

7. Harmsen S, Teraphongphom N, Tweedle MF, Basilion JP, Rosenthal EL. Optical Surgical Navigation for Precision in Tumor Resections. Mol Imaging Biol MIB Off Publ Acad Mol Imaging. 2017;19(3):357–62.

8. Rosenthal EL, Warram JM, Bland KI, Zinn KR. The Status of Contemporary Image-Guided Modalities in Oncologic Surgery. Ann Surg. 2015 Jan;261(1):46–55.

9. Mehanna C H, Paleri, V, West, CML,& Nutting. Head and neck cancer—Part 1: Epidemiology, presentation, and prevention. BMJ. 2010;341(7774):663–666.

10. Payakachat N, Ounpraseuth S, Suen JY. Late complications and long-term quality of life for survivors (>5 years) with history of head and neck cancer. Head Neck. 2013;35(6):819–825.

11. Nguyen TH, Ho DQ-D. Nonmelanoma skin cancer. Curr Treat Options Oncol. 2002 Jun;3(3):193–203.

12. Slootweg PJ, Hordijk GJ, Schade Y, van Es RJ, Koole R. Treatment failure and margin status in head and neck cancer. A critical view on the potential value of molecular pathology. Oral Oncol. 2002;38(5):500–503.

13. Gibson MK, Forastiere AA. Multidisciplinary approaches in the management of advanced head and neck tumors: state of the art. In: Current Opinion in Oncology. 2004. p. 220–224.

14. Brocklehurst P, Kujan O, O'Malley LA, Ogden G, Shepherd S, Glenny A-M. Screening programmes for the early detection and prevention of oral cancer. Cochrane Database Syst Rev. 2013 Nov;(11):CD004150.

15. Forastiere A, Koch W, Trotti A, Sidransky D. Head and neck cancer. N Engl J Med. 2001;345(26):1890–1900.

16. Kowalski LP, Carvalho AL. Influence of time delay and clinical upstaging in the prognosis of head and neck cancer. Oral Oncol. 2001 Jan;37(1):94–98.

17. Siegel RL, Miller KD, Jemal A. Cancer statistics, 2015. CA Cancer J Clin. 2015 Jan;65(1):5–29.

18. Epstein JD, Knight TK, Epstein JB, Bride MA, others. Cost of care for early-and late-stage oral and pharyngeal cancer in the California Medicaid population. Head &. 2008;

19. Funk GF, Hoffman HT, Karnell LH, Ricks JM, Zimmerman MB, Corbae DP, et al. Cost-identification analysis in oral cavity cancer management. Otolaryngol Head Neck Surg. 1998 Feb;118(2):211–220.

20. Lang K, Menzin J, Earle CC, Jacobson J, Hsu M-A. The economic cost of squamous cell cancer of the head and neck: findings from linked SEER-Medicare data. Arch Otolaryngol Neck Surg. 2004;130(11):1269–1275.

21. Lee JM, Turini M, Botteman MF, Stephens JM, Pashos CL. Economic burden of head and neck cancer. Eur J Health Econ Former HEPAC. 2004 Feb;5(1):70–80.

22. Mignogna MD, Fedele S, Lo Russo L, Ruoppo E, Lo Muzio L. Oral and pharyngeal cancer: lack of prevention and early detection by health care providers. Eur J Cancer Prev. 2001 Aug;10(4):381–383.

23. Mignogna MD, Fedele S, Lo Russo L. The World Cancer Report and the burden of oral cancer. Eur J Cancer Prev. 2004 Apr;13(2):139–142.

24. Allison P, Locker D, Feine JS. The role of diagnostic delays in the prognosis of oral cancer: a review of the literature. Oral Oncol. 1998;34(3):161–170.

25. Gillison M. Chapter 8. HPV vaccines and potential prevention of HPV-positive head and neck cancer. International Agency for Research on Cancer; 2014.

26. Herrero R, Quint W, Hildesheim A, Gonzalez P, Struijk L, Katki HA, et al. Reduced prevalence of oral human papillomavirus (HPV) 4 years after bivalent HPV vaccination in a randomized clinical trial in Costa Rica. PLoS One. 2013 Jul;8(7):e68329.

27. Joseph BK. Oral cancer: prevention and detection. Med Princ Pr. 2002;11 Suppl 1:32–35.

28. Epstein JB, Zhang L, Rosin M. Advances in the diagnosis of oral premalignant and malignant lesions. J-Can Dent Assoc. 2002;68(10):617–621.

29. Lingen MW, Kalmar JR, Karrison T, Speight PM. Critical evaluation of diagnostic aids for the detection of oral cancer. Oral Oncol. 2008 Jan;44(1):10–22.

30. Greven KM, Keyes JW, Williams DW, McGuirt WF, and W. T. Joyce. Occult primary tumors of the head and neck,. Cancer. 86(1):114–118.

31. Harréus U. Surgical errors and risks - the head and neck cancer patient. GMS Curr Top Otorhinolaryngol Head Neck Surg. 2013 Dec;12:Doc04.

32. Larson RA, Thomas H, Cleveland JC. Errors in management of head and neck tumors. CA Cancer J Clin. 1968;18(2):92–95.

33. Argiris A, Karamouzis M V., Raben D, Ferris RL. Head and neck cancer. The Lancet. 2008;371(9625):1695–1709.

34. Forastiere A, Koch W, Trotti A, Sidransky D. Head and neck cancer. N Engl J Med. 2001;345(26):1890–1900.

35. Pfister DG, Spencer S, Brizel DM, Burtness B, Busse PM, Caudell JJ, et al. Head and neck cancers, Version 2.2014. Clinical practice guidelines in oncology. J Natl Compr Canc Netw. 2014 Oct;12(10):1454–87.

36. Boysen M, Natvig K, Winther FO, Tausjö J. Value of routine follow-up in patients treated for squamous cell carcinoma of the head and neck. J Otolaryngol. 1985 Aug;14(4):211–4.

37. Ritoe SC, Krabbe PFM, Kaanders JHAM, van den Hoogen FJA, Verbeek ALM, Marres HAM. Value of routine follow-up for patients cured of laryngeal carcinoma. Cancer. 2004 Sep 15;101(6):1382–9.

38. Kraft M, Fostiropoulos K, Gürtler N, Arnoux A, Davaris N, Arens C. Value of narrow band imaging in the early diagnosis of laryngeal cancer. Head Neck. 2016 Jan;38(1):15–20.

39. Keller F, Psychogios G, Linke R, Lell M, Kuwert T, Iro H, et al. Carcinoma of unknown primary in the head and neck: comparison between positron emission tomography (PET) and PET/CT. Head Neck. 2011 Nov;33(11):1569–75.

40. Canto MT, Horowitz AM, Child WL. Views of oral cancer prevention and early detection: Maryland physicians. Oral Oncol. 2002 Jun;38(4):373–7.

41. Mashberg A, Feldman LJ. Clinical criteria for identifying early oral and oropharyngeal carcinoma: erythroplasia revisited. Am J Surg. 1988;156(4):273–275.

42. Sidransky D. Emerging molecular markers of cancer. Nat Rev Cancer. 2002 Mar;2(3):210–9.

43. Silverman S Jr. Early diagnosis of oral cancer. Cancer. 1988 Oct 15;62(8 Suppl):1796–9.

44. Keereweer S, Kerrebijn JDF, van Driel PBAA, Xie B, Kaijzel EL, Snoeks TJA, et al. Optical Image-guided Surgery—Where Do We Stand? Mol Imaging Biol. 2011 Apr;13(2):199–207.

45. Vahrmeijer AL, Hutteman M, van der Vorst JR, van de Velde CJH, Frangioni JV. Image-guided cancer surgery using near-infrared fluorescence. Nat Rev Clin Oncol. 2013;10(9):507–518.

46. De Boer E, Harlaar NJ, Taruttis A, Nagengast WB, Rosenthal EL, Ntziachristos V, et al. Optical innovations in surgery. Br J Surg. 2015;102(2):56–72.

47. DeLong JC, Hoffman RM, Bouvet M. Current status and future perspectives of fluorescence-guided surgery for cancer. Expert Rev Anticancer Ther. 2016;16(1):71–81.

48. Rosenthal EL, Warram JM, de Boer E, Basilion JP, Biel MA, Bogyo M, et al. Successful Translation of Fluorescence Navigation During Oncologic Surgery: A Consensus Report. J Nucl Med. 2016;57(1):144–150.

49. Farah CS, John K, Wu J. Contemporary Assessment and Management of Head and Neck Cancer Surgical Margins. In: Contemporary Issues in Head and Neck Cancer Management. InTech; 2015.

50. DiNardo LJ, Lin J, Karageorge LS, Powers CN. Accuracy, utility, and cost of frozen section margins in head and neck cancer surgery. Laryngoscope. 2000;110:1773–1776.

51. Woolgar JA, Triantafyllou A. A histopathological appraisal of surgical margins in oral and oropharyngeal cancer resection specimens. Oral Oncol. 2005 Nov;41(10):1034–1043.

52. Iseli TA, Lin MJ, Tsui A, Guiney A, Wiesenfeld D, Iseli CE. Are wider surgical margins needed for early oral tongue cancer? J Laryngol Otol. 2012;126(03):289–294.

53. Keereweer S, Sterenborg HJCM, Kerrebijn JDF, Van Driel PBAA, de Jong RJB, Löwik CWGM. Image-guided surgery in head and neck cancer: Current practice and future directions of optical imaging. Head Neck. 2012;34(1):120–126.

54. De Boer E, Harlaar NJ, Taruttis A, Nagengast WB, Rosenthal EL, Ntziachristos V, et al. Optical innovations in surgery. Br J Surg. 2015;102(2):102.

55. Hughes OR, Stone N, Kraft M, Arens C, Birchall MA. Optical and molecular techniques to identify tumor margins within the larynx. Head Neck Pathol. 2010;32(11):1544–1553.

56. Green B, Cobb ARM, Brennan PA, Hopper C. Optical diagnostic techniques for use in lesions of the head and neck: Review of the latest developments. Br J Oral Maxillofac Surg. 2014;52(8):675–680.

57. Rosenthal EL, Warram JM, Bland KI, Zinn KR. The status of contemporary image-guided modalities in oncologic surgery. Ann Surg. 2015 Jan;261(1):46–55.

58. Atallah I, Milet C, Coll J-L, Reyt E, Righini CA, Hurbin A. Role of near-infrared fluorescence imaging in head and neck cancer surgery: from animal models to humans. Eur Arch Otorhinolaryngol. 2014;(2015):2593–2600.

59. Iqbal H, Pan Q. Image guided surgery in the management of head and neck cancer. Oral Oncol. 2016 Jun;57:32–39.

60. Koch M, Ntziachristos V. Advancing Surgical Vision with Fluorescence Imaging. Annu Rev Med. 2016;67(1):153–164.

61. Frangioni JV. New technologies for human cancer imaging. J Clin Oncol. 2008;26(24):4012–4021.

62. Keereweer S, Van Driel PBAA, Snoeks TJA, Kerrebijn JDF, Baatenburg de Jong RJ, Vahrmeijer AL, et al. Optical image-guided cancer surgery: challenges and limitations. Clin Cancer Res. 2013;19(14):3745–3754.

63. ViziLite Specifications.

64. Vivosight Specifications [Internet]. Available from: https://vivosight.com/about-us/product/

65. Identafi Specifications [Internet]. Available from: http://www.dentalez.com/products/stardental/identafi/59-identafi-product-literature-photographs-manuals

66. Velscope Specifications [Internet]. Available from: https://www.sourceonedental.com/products/velscope-vx-enhanced-oral-cancer-screening-system

67. Awan KH, Morgan PR, Warnakulasuriya S. Evaluation of an autofluorescence based imaging system (VELscope™) in the detection of oral potentially malignant disorders and benign keratoses. Oral Oncol. 2011 Apr 1;47(4):274–7.

68. Cicciù M, Herford AS, Cervino G, Troiano G, Lauritano F, Laino L. Tissue Fluorescence Imaging (VELscope) for Quick Non-Invasive Diagnosis in Oral Pathology. J Craniofac Surg. 2017 Mar;28(2):e112–5.

69. Ganga RS, Gundre D, Bansal S, Shirsat PM, Prasad P, Desai RS. Evaluation of the diagnostic efficacy and spectrum of autofluorescence of benign, dysplastic and malignant lesions of the oral cavity using VELscope. Oral Oncol. 2017;75:67–74.

70. D. M. Laskin ESO. Efficacy of the ViziLite system in the identification of oral lesions,. J Oral Maxillofac Surg. 65(3):424–426.

71. Epstein JB, Gorsky M, Lonky S, Silverman S, Epstein JD, and M. Bride. The efficacy of oral lumenoscopyTM(ViziLite®) in visualizing oral mucosal lesions,. Spec Care Dent. 26(4):171–174.

72. Lee AMD, Cahill L, Liu K, MacAulay C, Poh C, Lane P. Wide-field in vivo oral OCT imaging. Biomed Opt Express. 2015 Jul 1;6(7):2664–74.

73. Dong L, Wijesinghe P, Dantuono JT, Sampson DD, Munro PRT, Kennedy BF, et al. Quantitative Compression Optical Coherence Elastography as an Inverse Elasticity Problem. IEEE J Sel Top Quantum Electron. 2016;22(3):277–87.

74. Larin KV, Sampson DD. Optical coherence elastography – OCT at work in tissue biomechanics [Invited]. Biomed Opt Express. 2017;8(2):1172.

75. Larson DL, Larson JD. Head and neck melanoma. Clin Plast Surg. 2010;37(1):73–77.

76. Zito PM, Scharf R. Cancer, Melanoma Of The Head And Neck. In: StatPearls [Internet]. Treasure Island (FL): StatPearls Publishing; 2019 [cited 2020 Jan 10]. Available from: http://www.ncbi.nlm.nih.gov/books/NBK513248/

77. Shashanka R, Smitha BR. Head and Neck Melanoma. ISRN Surg [Internet]. 2012 Mar 26 [cited 2020 Jan 10];2012. Available from: https://www.ncbi.nlm.nih.gov/pmc/articles/PMC3337483/

78. Koolen PGL, Matos TR, Ibrahim AMS, Sun J, Lee BT, Frankenthaler RA, et al. Recurrence Rates Over 20 Years in the Treatment of Malignant Melanoma: Immediate Versus Delayed Reconstruction. Plast Reconstr Surg Glob Open [Internet]. 2017 Jul 12 [cited 2020 Jan 7];5(7). Available from: https://www.ncbi.nlm.nih.gov/pmc/articles/PMC5548559/

79. Larson DL, Larson JD. Head and neck melanoma. Clin Plast Surg. 2010 Jan;37(1):73–7.

80. Cengiz FP, Cengiz AB, Emiroglu N, Comert E, Wellenhof RH. Dermoscopic and clinical features of head and neck melanoma. An Bras Dermatol. 2015;90(4):488–93.

81. Jose RM, Kisku W, Pradhan A, Prinsloo D. Management of complex melanomas of head and neck region. J Plast Reconstr Aesthet Surg. 2010 Apr;63(4):573–7.

82. Lachiewicz AM, Berwick M, Wiggins CL, Thomas NE. Survival differences between patients with scalp or neck melanoma and those with melanoma of other sites in the Surveillance, Epidemiology, and End Results (SEER) program. Arch Dermatol. 2008 Apr;144(4):515–21.

83. Berdahl JP, Pockaj BA, Gray RJ, Casey WJ, Woog JJ. Optimal management and challenges in treatment of upper facial melanoma. Ann Plast Surg. 2006 Dec;57(6):616–20.

84. Fincher TR, O'Brien JC, McCarty TM, Fisher TL, Preskitt JT, Lieberman ZH, et al. Patterns of drainage and recurrence following sentinel lymph node biopsy for cutaneous melanoma of the head and neck. Arch Otolaryngol Head Neck Surg. 2004 Jul;130(7):844–8.

85. Karakousis CP, Balch CM, Urist MM, Ross MM, Smith TJ, Bartolucci AA. Local recurrence in malignant melanoma: long-term results of the multiinstitutional randomized surgical trial. Ann Surg Oncol. 1996 Sep;3(5):446–52.

86. Leong SPL, Accortt NA, Essner R, Ross M, Gershenwald JE, Pockaj B, et al. Impact of sentinel node status and other risk factors on the clinical outcome of head and neck melanoma patients. Arch Otolaryngol Head Neck Surg. 2006 Apr;132(4):370–3.

87. O'Brien CJ, Coates AS, Petersen-Schaefer K, Shannon K, Thompson JF, Milton GW, et al. Experience with 998 cutaneous melanomas of the head and neck over 30 years. Am J Surg. 1991 Oct;162(4):310–4.

88. Cohen DK, Goldberg DJ. Mohs Micrographic Surgery: Past, Present, and Future. Dermatol Surg Off Publ Am Soc Dermatol Surg Al. 2019;45(3):329–39.

89. Perkins W. Who should have Mohs micrographic surgery? Curr Opin Otolaryngol Head Neck Surg. 2010 Aug;18(4):283–9.

90. Prickett KA, Ramsey ML. Mohs Micrographic Surgery. In: StatPearls [Internet]. Treasure Island (FL): StatPearls Publishing; 2020 [cited 2020 Apr 22]. Available from: http://www.ncbi.nlm.nih.gov/books/NBK441833/

91. Tas F, Erturk K. Recurrence behavior in early-stage cutaneous melanoma: pattern, timing, survival, and influencing factors. Melanoma Res. 2017;27(2):134–9.

92. Lee AY, Droppelmann N, Panageas KS, Zhou Q, Ariyan CE, Brady MS, et al. Patterns and Timing of Initial Relapse in Pathologic Stage II Melanoma Patients. Ann Surg Oncol. 2017 Apr;24(4):939–46.

93. Romano E, Scordo M, Dusza SW, Coit DG, Chapman PB. Site and timing of first relapse in stage III melanoma patients: implications for follow-up guidelines. J Clin Oncol Off J Am Soc Clin Oncol. 2010 Jun 20;28(18):3042–7.

94. Fornage BD, Lorigan JG. Sonographic detection and fine-needle aspiration biopsy of nonpalpable recurrent or metastatic melanoma in subcutaneous tissues. J Ultrasound Med. 1989;8(8):421–4.

95. Freeman M, Laks S. Surveillance imaging for metastasis in high-risk melanoma: importance in individualized patient care and survivorship. Melanoma Manag. 2019 Mar 1;6(1):MMT12.

96. Coit DG, Thompson JA, Albertini MR, Barker C, Carson WE, Contreras C, et al. Cutaneous Melanoma, Version 2.2019, NCCN Clinical Practice Guidelines in Oncology. J Natl Compr Cancer Netw JNCCN. 2019 Apr 1;17(4):367–402.

97. Häffner AC, Garbe C, Burg G, Büttner P, Orfanos CE, Rassner G. The prognosis of primary and metastasising melanoma. An evaluation of the TNM classification in 2,495 patients. Br J Cancer. 1992 Nov;66(5):856–61.

98. Mohr P, Eggermont AMM, Hauschild A, Buzaid A. Staging of cutaneous melanoma. Ann Oncol. 2009 Aug 1;20(suppl_6):vi14–21.

99. Kelly JW, Sagebiel RW, Calderon W, Murillo L, Dakin RL, Blois MS. The frequency of local recurrence and microsatellites as a guide to reexcision margins for cutaneous malignant melanoma. Ann Surg. 1984 Dec;200(6):759–63.

100. Ferrante di Ruffano L, Dinnes J, Deeks JJ, Chuchu N, Bayliss SE, Davenport C, et al. Optical coherence tomography for diagnosing skin cancer in adults. Cochrane Database Syst Rev. 2018 04;12:CD013189.

101. Wang J, Xu Y, Boppart SA. Review of optical coherence tomography in oncology. J Biomed Opt. 2017 Dec 22;22(12):1.

102. Rigel DS, Russak J, Friedman R. The evolution of melanoma diagnosis: 25 years beyond the ABCDs. CA Cancer J Clin. 2010 Oct;60(5):301–16.

103. Sattler E, Kästle R, Welzel J. Optical coherence tomography in dermatology. J Biomed Opt. 2013 Jun;18(6):061224.

104. Gambichler T, Jaedicke V, Terras S. Optical coherence tomography in dermatology: technical and clinical aspects. Arch Dermatol Res. 2011 Sep;303(7):457–73.

105. Gambichler T, Regeniter P, Bechara FG, Orlikov A, Vasa R, Moussa G, et al. Characterization of benign and malignant melanocytic skin lesions using optical coherence tomography in vivo. J Am Acad Dermatol. 2007 Oct;57(4):629–37.

106. Dinnes J, Bamber J, Chuchu N, Bayliss SE, Takwoingi Y, Davenport C, et al. High-frequency ultrasound for diagnosing skin cancer in adults. Cochrane Database Syst Rev [Internet]. 2018 [cited 2020 Jan 9];(12). Available from: https://www.cochranelibrary.com/cdsr/doi/10.1002/14651858.CD013188/abstract

107. A P, K T, E L-M, P H, T P, Jp L, et al. Use of high-definition optical coherent tomography (HD-OCT) for imaging of melanoma. Br J Dermatol. 2013 Oct 1;169(4):950–2.

108. Boone M a. LM, Suppa M, Dhaenens F, Miyamoto M, Marneffe A, Jemec GBE, et al. In vivo assessment of optical properties of melanocytic skin lesions and differentiation of melanoma from non-malignant lesions by high-definition optical coherence tomography. Arch Dermatol Res. 2016 Jan;308(1):7–20.

109. Gambichler T, Plura I, Schmid-Wendtner M, Valavanis K, Kulichova D, Stücker M, et al. High-definition optical coherence tomography of melanocytic skin lesions. J Biophotonics. 2015 Aug;8(8):681–6.

110. Goodson AG, Grossman D. Strategies for early melanoma detection: Approaches to the patient with nevi. J Am Acad Dermatol. 2009 May;60(5):719–35; quiz 736–8.

111. Gambichler T, Schmid-Wendtner MH, Plura I, Kampilafkos P, Stücker M, Berking C, et al. A multicentre pilot study investigating high-definition optical coherence tomography in the differentiation of cutaneous melanoma and melanocytic naevi. J Eur Acad Dermatol Venereol JEADV. 2015 Mar;29(3):537–41.

112. Vitkin IA, Woolsey J, Wilson BC, Anderson RR. Optical and thermal characterization of natural (Sepia officinalis) melanin. Photochem Photobiol. 1994 Apr;59(4):455–62.

113. Youssef S. High Resolution Imaging and Digital Characterization of Skin Pathology By Scanning Acoustic Microscopy. 2018.

114. Solivetti FM, Di Luca Sidozzi A, Pirozzi G, Coscarella G, Brigida R, Eibenshutz L. Sonographic evaluation of clinically occult in-transit and satellite metastases from cutaneous malignant melanoma. Radiol Med (Torino). 2006 Aug;111(5):702–8.

115. Czarnecka A, Czarnecki R, Witkiewicz W, Hryncewicz-Gwóźdź A. Importance of sonography of the skin and subcutaneous tissue in the early diagnosis of melanoma in-transit metastasis with the presentation of two cases. Adv Dermatol Allergol Dermatol Alergol. 2018 Apr;35(2):204–7.

116. Machet L, Nemeth-Normand F, Giraudeau B, Perrinaud A, Tiguemounine J, Ayoub J, et al. Is ultrasound lymph node examination superior to clinical examination in melanoma follow-up? A monocentre cohort study of 373 patients. Br J Dermatol. 2005 Jan;152(1):66–70.

117. Garbe C, Amaral T, Peris K, Hauschild A, Arenberger P, Bastholt L, et al. European consensus-based interdisciplinary guideline for melanoma. Part 1: Diagnostics - Update 2019. Eur J Cancer Oxf Engl 1990. 2020 Jan 9;

118. Bafounta M-L, Beauchet A, Chagnon S, Saiag P. Ultrasonography or palpation for detection of melanoma nodal invasion: a meta-analysis. Lancet Oncol. 2004 Nov;5(11):673–80.

119. Mehta N, Sharma R, Madhok R, Agrawal T, Sharma V. A clinical, radiological, and histopathological correlation of neck nodes in patients undergoing neck dissection. Int J Appl Basic Med Res. 2018 Jan 1;8(1):9.

120. Zhou Y, Yao J, Wang LV. Tutorial on photoacoustic tomography. J Biomed Opt. 2016 Jun;21(6):61007.

121. Weber J, Beard PC, Bohndiek SE. Contrast agents for molecular photoacoustic imaging. Nat Methods. 2016 Aug;13(8):639–50.

122. Hai P, Zhou Y, Zhang R, Ma J, Li Y, Shao J-Y, et al. Label-free high-throughput detection and quantification of circulating melanoma tumor cell clusters by linear-array-based photoacoustic tomography. J Biomed Opt [Internet]. 2017 Apr [cited 2020 Jan 16];22(4). Available from: https://www.ncbi.nlm.nih.gov/pmc/articles/PMC5995136/

123. Catalano O, Roldán FA, Varelli C, Bard R, Corvino A, Wortsman X. Skin cancer: findings and role of high-resolution ultrasound. J Ultrasound. 2019 Dec;22(4):423–31.

124. Lee Y-J, Jeong E-J, Song H-W, Ahn C-G, Noh HW, Sim JY, et al. Photoacoustic imaging probe for detecting lymph nodes and spreading of cancer at various depths. J Biomed Opt. 2017 Apr;22(9):091513.

125. Kim H, Chang JH. Multimodal photoacoustic imaging as a tool for sentinel lymph node identification and biopsy guidance. Biomed Eng Lett. 2018 May;8(2):183–91.

126. Stoffels I, Morscher S, Helfrich I, Hillen U, Leyh J, Burton NC, et al. Metastatic status of sentinel lymph nodes in melanoma determined noninvasively with multispectral optoacoustic imaging. Sci Transl Med. 2015 Dec 9;7(317):317ra199-317ra199.

127. McCormack D, Al-Shaer M, Goldschmidt BS, Dale PS, Henry C, Papageorgio C, et al. Photoacoustic detection of melanoma micrometastasis in sentinel lymph nodes. J Biomech Eng. 2009 Jul;131(7):074519.

128. Zhou Y, Tripathi SV, Rosman I, Ma J, Hai P, Linette GP, et al. Noninvasive Determination of Melanoma Depth using a Handheld Photoacoustic Probe. J Invest Dermatol. 2017 Jun 1;137(6):1370–2.

129. Neuschmelting V, Lockau H, Ntziachristos V, Grimm J, Kircher MF. Lymph Node Micrometastases and In-Transit Metastases from Melanoma: In Vivo Detection with Multispectral Optoacoustic Imaging in a Mouse Model. Radiology. 2016 Jul;280(1):137–50.

130. Steinberg I, Huland DM, Vermesh O, Frostig HE, Tummers WS, Gambhir SS. Photoacoustic clinical imaging. Photoacoustics. 2019 Jun 8;14:77–98.

131. Cao T, Tey HL. Hochauflösende optische Kohärenztomografie – ein Hilfsmittel in klinischer Praxis und dermatologischer Forschung. JDDG J Dtsch Dermatol Ges. 2015;13(9):886–90.

132. Halani S, Foster FS, Breslavets M, Shear NH. Ultrasound and Infrared-Based Imaging Modalities for Diagnosis and Management of Cutaneous Diseases. Front Med [Internet]. 2018 [cited 2020 Jan 11];5. Available from: https://www.frontiersin.org/articles/10.3389/fmed.2018.00115/full

133. Schuetzenberger K, Pfister M, Messner A, Froehlich V, Garhoefer G, Hohenadl C, et al. Comparison of optical coherence tomography and high frequency ultrasound imaging in mice for the assessment of skin morphology and intradermal volumes. Sci Rep. 2019 Sep 20;9(1):1–7.

134. Zhou Y, Xing W, Maslov KI, Cornelius LA, Wang LV. Handheld photoacoustic microscopy to detect melanoma depth in vivo. Opt Lett. 2014 Aug 15;39(16):4731–4.

135. Wang L, Maslov K, Xing W, Garcia-Uribe A, Wang LV. Video-rate functional photoacoustic microscopy at depths. J Biomed Opt [Internet]. 2012 Oct [cited 2020 Jan 12];17(10). Available from: https://www.ncbi.nlm.nih.gov/pmc/articles/PMC3461058/

136. Yu Q, Huang S, Wu Z, Zheng J, Chen X, Nie L. Label-free Visualization of Early Cancer Hepatic Micrometastasis and Intraoperative Image-guided Surgery by Photoacoustic Imaging. J Nucl Med Off Publ Soc Nucl Med. 2019 Dec 5;

137. Esteva A, Kuprel B, Novoa RA, Ko J, Swetter SM, Blau HM, et al. Dermatologist-level classification of skin cancer with deep neural networks. Nature. 2017 Feb;542(7639):115–8.

138. Gerami P, Yao Z, Polsky D, Jansen B, Busam K, Ho J, et al. Development and validation of a noninvasive 2-gene molecular assay for cutaneous melanoma. J Am Acad Dermatol. 2017 Jan;76(1):114-120.e2.

139. Andrėkutė K, Linkevičiūtė G, Raišutis R, Valiukevičienė S, Makštienė J. Automatic Differential Diagnosis of Melanocytic Skin Tumors Using Ultrasound Data. Ultrasound Med Biol. 2016 Dec 1;42(12):2834–43.

140. Stuckensen T, Kovács AF, Adams S, Baum RP. Staging of the neck in patients with oral cavity squamous cell carcinomas: a prospective comparison of PET, ultrasound, CT and MRI. J Cranio-Maxillo-fac Surg Off Publ Eur Assoc Cranio-Maxillo-fac Surg. 2000 Dec;28(6):319–24.

141. Liu M, Drexler W. Optical coherence tomography angiography and photoacoustic imaging in dermatology. Photochem Photobiol Sci. 2019;18(5):945–62.

142. Hawkins WG, Busam KJ, Ben-Porat L, Panageas KS, Coit DG, Gyorki DE, et al. Desmoplastic melanoma: a pathologically and clinically distinct form of cutaneous melanoma. Ann Surg Oncol. 2005 Mar;12(3):207–13.

143. Swetter SM, Tsao H, Bichakjian CK, Curiel-Lewandrowski C, Elder DE, Gershenwald JE, et al. Guidelines of care for the management of primary cutaneous melanoma. J Am Acad Dermatol. 2019 Jan;80(1):208–50.

144. Moyer JS, Rudy S, Boonstra PS, Kraft C, Chinn SB, Baker SR, et al. Efficacy of Staged Excision With Permanent Section Margin Control for Cutaneous Head and Neck Melanoma. JAMA Dermatol. 2017 01;153(3):282–8.

145. Wagnières GA, Star WM, Wilson BC. In vivo fluorescence spectroscopy and imaging for oncological applications. Photochem Photobiol. 1998;68(5):603–632.

146. van Driel PB LCW van der Vorst JR, Verbeek FP, Oliveira S, Snoeks TJ, Keereweer S, Frangioni JV, van Bergen En Henegouwen PM, Vahrmeijer AL. Inoperative fluorescence delineation of head and neck cancer with a fluorescent anti-epidermal growth factor receptor nanobody. Int J Cancer. 2013;134:1–35.

147. Bredell MG. Sentinel lymph node mapping by indocyanin green fluorescence imaging in oropharyngeal cancer - Preliminary experience. Head Neck Oncol. 2010;2(1):31.

148. Yokoyama J, Fujimaki M, Shinichi Ohba, Takashi Anzai, Ryota Yoshii, Shin Ito, et al. A feasibility study of NIR fluorescent image-guided surgery in head and neck cancer based on the assessment of optimum surgical time as revealed through dynamic imaging. Onco Targets Ther. 2013 Apr;6 SRC-G:325.

149. Oliveira S, Dongen GAMSV, Walsum MS, Roovers RC, Stam JC, Diest PJV, et al. Rapid Visualization of Human Tumor Xenografts through Optical Imaging with a Near-infrared Fluorescent Anti – Epidermal Growth Factor Receptor Nanobody. Mol Imaging. 2011;0(0):1–14.

150. Huang H, Bai Y-L, Yang K, Tang H, Wang Y-W. Optical imaging of head and neck squamous cell carcinoma in vivo using arginine-glycine-aspartic acid peptide conjugated near-infrared quantum dots. Onco Targets Ther. 2013;6:1779–1787.

151. Gioux S, Coutard J-G, Berger M, Grateau H, Josserand V, Keramidas M, et al. FluoSTIC: miniaturized fluorescence image-guided surgery system. Vol. 17. 2012. 106014 p.

152. Frangioni JV. Translating in vivo diagnostics into clinical reality. Nat Biotechnol. 2006;24(8):909–913.

153. Moore LS, Rosenthal EL, Chung TK, de Boer E, Patel N, Prince AC, et al. Characterizing the Utility and Limitations of Repurposing an Open-Field Optical Imaging Device for Fluorescence-Guided Surgery in Head and Neck Cancer Patients. J Nucl Med. 2017;58(2):246–251.

154. Orosco RK, Tsien RY, Nguyen QT. Fluorescence imaging in surgery. IEEE Rev Biomed Eng. 2013;6:178–187.

155. Poh CF, Zhang L, Anderson DW, Durham JS, Williams PM, Priddy RW, et al. Fluorescence visualization detection of field alterations in tumor margins of oral cancer patients. Clin Cancer Res. 2006;12(22):6716–6722.

156. Fresko D, Lazarus SS. Oral carcinoma in situ. Its progression to squamous, basosquamous, and basal-cell carcinoma. Arch Pathol Lab Med. 1981 Jan;105(1):15–19.

157. Gillenwater A, Jacob R, Ganeshappa R, Kemp B, El-Naggar AK, Palmer JL, et al. Noninvasive diagnosis of oral neoplasia based on fluorescence spectroscopy and native tissue autofluorescence. Arch Otolaryngol Head Neck Surg. 1998 Nov;124(11):1251–8.

158. Drezek R, Brookner C, Pavlova I, Boiko I, Malpica A, Lotan R, et al. Autofluorescence Microscopy of Fresh Cervical-Tissue Sections Reveals Alterations in Tissue Biochemistry with Dysplasia. Photochem Photobiol. 2001;73(6):636–641.

159. Garnis C, Coe BP, Ishkanian A, Zhang L, Rosin MP, Lam WL. Novel Regions of Amplification on 8q Distinct from the MYC Locus and Frequently Altered in Oral Dysplasia and Cancer. Genes Chromosomes Cancer. 2004;39(1):93–98.

160. Hayward JR, Regezi JA. Oral dysplasia and in situ carcinoma: clinicopathologic correlations of eight patients. J Oral Surg. 1977;35(9):756–762.

161. Heppner KJ, Matrisian LM, Jensen RA, Rodgers WH. Expression of most matrix metalloproteinase family members in breast cancer represents a tumor-induced host response. Am J Pathol. 1996;149(1):273–282.

162. Hittelman WN, Kim HJ, Lee JS, Shin DM, Lippman SM, Kim J, et al. Detection of chromosome instability of tissue fields at risk: In situ hybridization. J Cell Biochem. 1996;63(SUPPL. 25):57–62.

163. Goldenberg D, Harden S, Masayesva BG, Ha P, Benoit N, Westra WH, et al. Intraoperative molecular margin analysis in head and neck cancer. Arch Otolaryngol Head Neck Surg. 2004;130(1):39–44.

164. Elson D, Requejo-Isidro J, Munro I, Reavell F, Siegel J, Suhling K, et al. Time-domain fluorescence lifetime imaging applied to biological tissue. Photochem Photobiol Sci. 2004;3(8):795–801.

165. Galletly NP, McGinty J, Dunsby C, Teixeira F, Requejo-Isidro J, Munro I, et al. Fluorescence lifetime imaging distinguishes basal cell carcinoma from surrounding uninvolved skin. Br J Dermatol. 2008;159(1):152–161.

166. Holash J. Vessel Cooption, Regression, and Growth in Tumors Mediated by Angiopoietins and VEGF. Science. 1999;284(5422):1994–1998.

167. Themelis G, Yoo JS, Soh K-S, Schulz R, Ntziachristos V. Real-time intraoperative fluorescence imaging system using light-absorption correction. Vol. 14. 2009. 064012 p.

168. Miles BA. How Close Are We to Real Time Optical Margin Control in Head and Neck Oncologic Surgery? Cancer Cell Microenviron. 2016;1–12.

169. Andersson-Engels S, Berg R, Persson A, Svanberg S. Multispectral tissue characterization with time-resolved detection of diffusely scattered white light. Opt Lett. 1993 Oct;18(20):1697–1699.

170. Cubeddu R, Comelli D, D'Andrea C, Taroni P, Valentini G. Time-resolved fluorescence imaging in biology and medicine. J Phys Appl Phys. 2002;35(9):R61.

171. Cubeddu R, Taroni P, Valentini G, Canti G. Use of time-gated fluorescence imaging for diagnosis in biomedicine. J Photochem Photobiol B. 1992;12(1):109–113.

172. Siegel J, Elson DS, Webb SED, Lee KCB, Vlandas A, Gambaruto GL, et al. Studying biological tissue with fluorescence lifetime imaging: microscopy, endoscopy, and complex decay profiles. Appl Opt. 2003 Jun;42(16):2995–3004.

173. Papaioannou T, Preyer NW, Fang Q, Brightwell A, Carnohan M, Cottone G, et al. Effects of fiber-optic probe design and probe-to-target distance on diffuse reflectance measurements of turbid media: an experimental and computational study at 337 nm. Appl Opt. 2004 May;43(14):2846–2860.

174. Meier JD, Xie H, Sun Y, Sun Y, Hatami N, Poirier B, et al. Time-resolved laser-induced fluorescence spectroscopy as a diagnostic instrument in head and neck carcinoma. Otolaryngol Head Neck Surg. 2010;142(6):838–44.

175. Wagnieres GA, Star WM, Wilson BC. In Vivo Fluorescence Spectroscopy and Imaging for Oncological Applications. Photochem Photobiol. 1998;68(5):603–32.

176. Marcu L. Fluorescence Lifetime Techniques in Medical Applications. Ann Biomed Eng. 2012 Feb 25;40(2):304–31.

177. De Veld DCG, Witjes MJH, Sterenborg HJCM, Roodenburg JLN. The status of in vivo autofluorescence spectroscopy and imaging for oral oncology. Oral Oncol. 2005;41(2):117–31.

178. Skala MC, Riching KM, Gendron-Fitzpatrick A, Eickhoff J, Eliceiri KW, White JG, et al. In vivo multiphoton microscopy of NADH and FAD redox states, fluorescence lifetimes, and cellular morphology in precancerous epithelia. Proc Natl Acad Sci U A. 2007 Dec;104(49):19494–19499.

179. Schwarz RA, Gao W, Weber CR, Kurachi C, Lee JJ, El-Naggar AK, et al. Noninvasive evaluation of oral lesions using depth-sensitive optical spectroscopy. Cancer. 2009;115(8):1669–79.

180. Sun Y, Phipps JE, Meier J, Hatami N, Poirier B, Elson DS, et al. Endoscopic Fluorescence Lifetime Imaging for In Vivo Intraoperative Diagnosis of Oral Carcinoma. Microsc Microanal. 2013;19(04):791–8.

181. Lakowicz JR. Principles of Fluorescence Spectroscopy. Lakowicz JR, editor. Vol. 13. Boston, MA: Springer US; 2006. 362 p.

182. Berezin MY, Achilefu S. Fluorescence lifetime measurements and biological imaging. Chem Rev. 2010 May;110(5):2641–2684.

183. Boreham A, Brodwolf R, Walker K, Haag R, Alexiev U. Time-Resolved Fluorescence Spectroscopy and Fluorescence Lifetime Imaging Microscopy for Characterization of Dendritic Polymer Nanoparticles and Applications in Nanomedicine. Molecules. 2016 Dec;22(1):17.

184. Liu L, Yang Q, Zhang M, Wu Z, Xue P. Fluorescence lifetime imaging microscopy and its applications in skin cancer diagnosis. J Innov Opt Health Sci. 2019 Sep;12(05):1930004.

185. Pradhan A, Das BB, Yoo KM, Cleary J, Prudente R, Celmer E, et al. Time-resolved UV photoexcited fluorescence kinetics from malignant and non-malignant human breast tissues. In: Lasers in the Life Sciences. 1992. p. 225–234.

186. Jain B, Majumder SK, Gupta PK. Time resolved and steady state autofluorescence spectroscopy of normal and malignant human breast tissue. In: Lasers in the Life Sciences. 1998. p. 163–173.

187. Mycek MA, Schomacker KT, Nishioka NS. Colonic polyp differentiation using time-resolved autofluorescence spectroscopy. Gastrointest Endosc. 1998;48(4):390–394.

188. Glanzmann T, Ballini J-P, Van Den Bergh H, Wagnieres G. Time-resolved spectrofluorometer for clinical tissue characterization during endoscopy. Rev Sci Instrum. 1999;70(10):4067–4077.

189. Dacosta RS, Wilson BC, Marcon NE. New optical technologies for earlier endoscopic diagnosis of premalignant gastrointestinal lesions. J Gastroenterol Hepatol. 2002;17(SUPPL. 1):85–104.

190. Pfefer TJ, Paithankar DY, Poneros JM, Schomacker KT, Nishioka NS. Temporally and spectrally resolved fluorescence spectroscopy for the detection of high grade dysplasia in Barrett's esophagus. In: Lasers in Surgery and Medicine. 2003. p. 10–16.

191. Fang Q, Papaioannou T, Jo JA, Vaitha R, Shastry K, Marcu L. Time-domain laser-induced fluorescence spectroscopy apparatus for clinical diagnostics. Vol. 75, Review of Scientific Instruments. 2004. p. 151–62.

192. Butte PV, Pikul BK, Hever A, Yong WH, Black KL, Marcu L. Diagnosis of meningioma by time-resolved fluorescence spectroscopy. J Biomed Opt. 2005;10(6):064026.

193. Chen HM, Chiang CP, You C, Hsiao TC, Wang CY. Time-resolved autofluorescence spectroscopy for classifying normal and premalignant oral tissues. In: Lasers in Surgery and Medicine. 2005. p. 37–45.

194. Leppert B, Krajewski J, Kantelhardt SR, Schlaffer S, Petkus N, Reusche E, et al. Multiphoton Excitation of Autoflurescence for Microscopy of Glioma Tissue • Residual glioma tissue is a problem tumor removal. Neurosurgery. 58:759–767.

195. Valeur B. Effect of Polarity on Fluorescence Emission. Polarity Probes. Vol. 8. 2001. 200–225 p.

196. Becker W. Advanced Time-Correlated Single Photon Counting Techniques. Castleman AW, Toennies JP, Zinth W, editors. Berlin, Heidelberg: Springer Berlin Heidelberg; 2005. (Springer Series in Chemical Physics; vol. 81).

197. Becker W. The bh TCSPC Handbook. 3rd ed. Becker & Hickl GmbH; 2010. 1–566 p.

198. Periasamy A, Clegg RM. FLIM microscopy in biology and medicine. CRC Press; 2009. 1–474 p.

199. Valeur B, Brochon J-C. New trends in fluorescence spectroscopy: applications to chemical and life sciences. Vol. 1. Springer Science & Business Media; 2012.

200. Meier JD, Xie H, Sun Y, Sun Y, Hatami N, Poirier B, et al. Time-resolved laser-induced fluorescence spectroscopy as a diagnostic instrument in head and neck carcinoma. J Otolaryngol Head Neck Surg. 2010;142(6):838–844.

201. Meyer T, Guntinas-Lichius O, von Eggeling F, Ernst G, Akimov D, Schmitt M, et al. Multimodal nonlinear microscopic investigations on head and neck squamous cell carcinoma: Toward intraoperative imaging. Chen A, editor. Head Neck. 2013 Sep;35(9):E280–E287.

202. Sun Y, Phipps JE, Meier J, Hatami N, Poirier B, Elson DS, et al. Endoscopic Fluorescence Lifetime Imaging for In Vivo Intraoperative Diagnosis of Oral Carcinoma. Microsc Microanal Off J Microsc Soc Am Microbeam Anal Soc Microsc Soc Can. 2013 Aug;19(4):791–8.

203. Sun Y, Meier J, Hatami N, Phipps J, Schrot RJ, Poirier B, et al. Fluorescence Lifetime Imaging Microscopy (FLIM) for Intraoperative Tumor Delineation: A Study in Patients. In: Optics in the Life Sciences [Internet]. Monterey, California: OSA; 2011 [cited 2019 Mar 7]. p. BWC6. Available from: https://www.osapublishing.org/abstract.cfm?URI=BODA-2011-BWC6

204. Liu X, Lin D, Becker W, Niu J, Yu B, Liu L, et al. Fast fluorescence lifetime imaging techniques: A review on challenge and development. J Innov Opt Health Sci. 2019 Sep;12(05):1930003.

205. Munro I, McGinty J, Galletly N, Requejo-Isidro J, Lanigan PMP, Elson DS, et al. Toward the clinical application of time-domain fluorescence lifetime imaging. J Biomed Opt. 2005;10(5):051403.

206. Silva SF, Domingues JP, Morgado AM. Can we use rapid lifetime determination for fast, fluorescence lifetime based, metabolic imaging? Precision and accuracy of double-exponential decay measurements with low total counts. PloS One. 2019;14(5):e0216894.

207. Grundfest WS, Stafsudd OM, Jiang PC, Papour A, and Z. D. Taylor. Time-resolved fluorescence imaging without lifetime fitting and illumination pulsed shaping for fluorescence lifetime imaging microscopy (film) enhancement,. US Pat Gaz. 61(605,844).

208. Sherman AJ, Papour A, Bhargava S, St. John MAR, Yong WH, Taylor Z, et al. Normalized fluorescence lifetime imaging for tumor identification and margin delineation. In: SPIE BiOS. San Francisco: SPIE; 2013. p. 85721H.

209. Papour A, Taylor Z, Sherman A, Sanchez D, Lucey G, Liau L, et al. Optical imaging for brain tissue characterization using relative fluorescence lifetime imaging. J Biomed Opt. 2013 Jun;18(6):60504.

210. Cheng H. Translational Research for Biophotonics Image-Guided Surgery [Internet]. UCLA; 2018 [cited 2020 Apr 13]. Available from: https://escholarship.org/uc/item/06h07815

211. Papour A. Fast biomedical imaging using fluorescence lifetime and unique Raman signatures [Internet]. UCLA; 2015 [cited 2020 Apr 26]. Available from: https://escholarship.org/uc/item/5ts6v6p9

212. Cheng H, Xie Y, Pellionisz P, Pearigen A, Rangwalla K, Stafsudd O, et al. Dynamic optical contrast imaging (DOCI): system theory for rapid, wide-field, multispectral optical imaging using fluorescence lifetime contrast mechanism. In: Medical Imaging 2019: Image-Guided Procedures, Robotic Interventions, and Modeling [Internet]. International Society for Optics and Photonics; 2019 [cited 2019 Apr 5]. p. 109512T. Available from: https://www.spiedigitallibrary.org/conference-proceedings-of-spie/10951/109512T/Dynamic-optical-contrast-imaging-DOCI--system-theory-for-rapid/10.1117/12.2513823.short

213. Papour A, Taylor Z, Stafsudd O, Tsui I, Grundfest W. Imaging autofluorescence temporal signatures of the human ocular fundus *in vivo*. J Biomed Opt. 2015 Nov 23;20(11):110505.

214. Considine PS. Effects of Coherence on Imaging Systems*. J Opt Soc Am. 1966;56(8):1001.

215. Cubeddu R, Canti G, Pifferi A, Taroni P, Valentini G. Fluorescence lifetime imaging of experimental tumors in hematoporphyrin derivative-sensitized mice. Photochem Photobiol. 1997;66(2):229–236.

216. Provenzano PP, Eliceiri KW, Keely PJ. Multiphoton microscopy and fluorescence lifetime imaging microscopy (FLIM) to monitor metastasis and the tumor microenvironment. Clin Exp Metastasis. 2009 Apr 3;26(4):357–70.

217. Tanaka T, Ishigamori R. Understanding carcinogenesis for fighting oral cancer. J Oncol. 2011 May;2011:603740.

218. A. L. Carvalho LPK. Influence of time delay and clinical upstaging in the prognosis of head and neck cancer,. Oral Oncol. 37(1):94–98.

219. McGurk M, Chan C, Jones J, O'regan E, and M. Sherriff. Delay in diagnosis and its effect on outcome in head and neck cancer,. Br J Oral Maxillofac Surg. 43(4):281–284.

220. Lee JM, Turini M, Botteman MF, Stephens JM, Pashos CL. Economic burden of head and neck cancer. Eur J Health Econ Former HEPAC. 2004;5(1):70–80.

221. Mignogna MD, Fedele S, and L. L. Russo. The World Cancer Report and the burden of oral cancer,. Eur J Cancer Prev. 13(2):139–142.

222. Society AC. Cancer facts and figures 2013. American Cancer Society Atlanta; 2013.

223. Mignogna MD, Fedele S, Russo LL, Ruoppo E, and L. L. Muzio. Oral and pharyngeal cancer: lack of prevention and early detection by health care providers,. Eur J Cancer Prev. 10(4):381–383.

224. Ho AS, Kraus DH, Ganly I, Lee NY, Shah JP, Morris LGT. Decision making in the management of recurrent head and neck cancer. Head Neck. 2014;36(1):144–51.

225. Tajudeen BA, Taylor ZD, Garritano J, Cheng H, Pearigen A, Sherman AJ, et al. Dynamic optical contrast imaging as a novel modality for rapidly distinguishing head and neck squamous cell carcinoma from surrounding normal tissue. Cancer. 2017;123(5):879–886.

226. Collingridge DR, Young WK, Vojnovic B, Wardman P, Lynch EM, Hill S a, et al. Measurement of tumor oxygenation: a comparison between polarographic needle electrodes and a time-resolved luminescence-based optical sensor. Radiat Res. 1997;147(3):329–334.

227. Gonzalez RC, Woods RE. Digital image processing. New York, NY: Pearson; 2018. 1168 p.

228. Pellionisz PA, Badran KW, Grundfest WS, St John MA. Detection of surgical margins in oral cavity cancer: the role of dynamic optical contrast imaging. Curr Opin Otolaryngol Head Neck Surg. 2018 Apr;26(2):102–107.

229. Cicchi R, Pavone FS. Non-linear fluorescence lifetime imaging of biological tissues. Anal Bioanal Chem. 2011 Jul;400(9):2687–97.

230. Seiwert TY, Cohen EEW. State-of-the-art management of locally advanced head and neck cancer. Br J Cancer. 2005;92(8):1341–1348.

231. Upile T, Jerjes W, Betz CS, El Maaytah M, Wright A, Hopper C. Optical diagnostic techniques in the head and neck. Dent Update. 2007;34(7):410–2, 415–6, 419–20 passim.

232. Cho JY, Hong SJ. Autofluorescence imaging: as a new method for predicting metachronous gastric cancer. J Gastroenterol Hepatol. 2010;25(12):1814–1815.

233. Mallia RJ, Subhash N, Mathews A, Kumar R, Thomas SS, Sebastian P, et al. Clinical grading of oral mucosa by curve-fitting of corrected autofluorescence using diffuse reflectance spectra. Head Neck Pathol. 2010;32(6):763–779.

234. Chen W, Gao X, Tian Q, Chen L. A comparison of autofluorescence bronchoscopy and white light bronchoscopy in detection of lung cancer and preneoplastic lesions: A meta-analysis. Lung Cancer. 2011;73(2):183–188.

235. Takeuchi Y, Hanaoka N, Hanafusa M, Ishihara R, Higashino K, Iishi H, et al. Autofluorescence imaging of early colorectal cancer. J Biophotonics. 2011;4:1853–1854.

236. Rana M, Zapf A, Kuehle M, Gellrich N-C, Eckardt AM. Clinical evaluation of an autofluorescence diagnostic device for oral cancer detection. Eur J Cancer Prev. 2012;21(5):460–466.

237. Meyer T, Vogler N, Dietzek B, Akimov D, Inhestern J, Guntinas-Lichius O, et al. Non-invasive label-free investigation and typing of head and neck cancers by multimodal nonlinear microscopy. In: Biophotonics: Photonic Solutions for Better Health Care III [Internet]. International Society for Optics and Photonics; 2012 [cited 2019 Oct 15]. p. 84270Z. Available from: https://www.spiedigitallibrary.org/conference-proceedings-of-spie/8427/84270Z/Non-invasive-label-free-investigation-and-typing-of-head-and/10.1117/12.921631.short

238. Tajudeen BA, Taylor ZD, Garritano J, Cheng H, Pearigen A, Sherman AJ, et al. Dynamic optical contrast imaging as a novel modality for rapidly distinguishing head and neck squamous cell carcinoma from surrounding normal tissue. Cancer. 2016;

239. Kim IA, Taylor ZD, Cheng H, Sebastian C, Maccabi A, Garritano J, et al. Dynamic Optical Contrast Imaging: A Technique to Differentiate Parathyroid Tissue from Surrounding Tissues. Otolaryngol-Head Neck Surg. 2017;156(3):480–3.

240. Patel CN, Salahudeen HM, Lansdown M, and A. F. Scarsbrook. Clinical utility of ultrasound and 99mTc sestamibi SPECT/CT for preoperative localization of parathyroid adenoma in patients with primary hyperparathyroidism,. Clin Radiol. 65:278–87.

241. Suh YJ, Choi JY, Kim S, Chun IK, Yun TJ, Lee KE, et al. Comparison of 4D CT, Ultrasonography, and 99m Tc Sestamibi SPECT/CT in Localizing Single-Gland Primary Hyperparathyroidism. Otolaryngol-Head Neck Surg. 2015 Mar 17;152(3):438–43.

242. F. Cetani CM. Clinical practice. Primary hyperparathyroidism,. N Engl J Med. 365:2389–97.

243. McWade MA, Paras C, White LM, Phay JE, Solórzano CC, Broome JT, et al. Label-free intraoperative parathyroid localization with near-infrared autofluorescence imaging. J Clin Endocrinol Metab. 2014;99(12):4574–80.

244. Paras C, Keller M, White L, Phay J, Mahadevan-Jansen A. Near-infrared autofluorescence for the detection of parathyroid glands. J Biomed Opt. 2011;16(6):067012.

245. Arici C, Cheah WK, Ituarte PH, Morita E, Lynch TC, Siperstein AE, et al. Can localization studies be used to direct focused parathyroid operations?,. Surgery. 129:720–9.

246. McWade MA, Paras C, White LM, Phay JE, Mahadevan-Jansen A, and J. T. Broome. A novel optical approach to intraoperative detection of parathyroid glands,. Surgery. 154:1371–1377.

247. Suh YJ, Choi JY, Kim SJ, Chun IK, Yun TJ, Lee KE, et al. Comparison of 4D CT, ultrasonography, and 99mTc sestamibi SPECT/CT in localizing single-gland primary hyperparathyroidism,. Otolaryngol Head Neck Surg. 152:438–43.

248. James BC, Nagar S, Tracy M, Kaplan EL, Angelos P, Scherberg NH, et al. A novel, ultrarapid parathyroid hormone assay to distinguish parathyroid from nonparathyroid tissue,. Surgery. 156:1638–43.

249. Abbott DE, Cantor SB, Grubbs EG, Santora R, Gomez HF, Evans DB, et al. Outcomes and economic analysis of routine preoperative 4-dimensional ct for surgical intervention in de novo primary hyperparathyroidism: Does clinical benefit justify the cost? J Am Coll Surg. 2012 Apr;214(4):629–37.

250. Purz S, Kluge R, Barthel H, Steinert F, Stumpp P, Kahn T, et al. Visualization of Ectopic Parathyroid Adenomas,. N Engl J Med. 369:2067–2069.

251. Cheung K, Wang TS, Farrokhyar F, Roman SA, and J. A. Sosa. A meta-analysis of preoperative localization techniques for patients with primary hyperparathyroidism,. Ann Surg Oncol. 19:577–83.

252. Patel CN, Salahudeen HM, Lansdown M, Scarsbrook AF. Clinical utility of ultrasound and 99m Tc sestamibi SPECT / CT for preoperative localization of parathyroid adenoma in patients with primary hyperparathyroidism. Clin Radiol. 2010;65(4):278–87.

253. Dowling K, Hyde SCW, Dainty JC, French PMW, Hares JD. 2-D fluorescence lifetime imaging using a time-gated image intensifier. Opt Commun. 1997;135(February):27–31.

254. Ntziachristos V, Chance B. Probing physiology and molecular function using optical imaging: applications to breast cancer. Breast Cancer Res BCR. 2001;3(1):41–6.

255. Bastiaens P. Fluorescence lifetime imaging microscopy: spatial resolution of biochemical processes in the cell. Trends Cell Biol. 1999;9(2):48–52.

256. Tadrous PJ. Methods for imaging the structure and function of living tissues and cells: 2. Fluorescence lifetime imaging. J Pathol. 2000;191(3):229–34.

257. Berezin MY, Achilefu S. Fluorescence Lifetime Measurements and Biological Imaging. Chem Rev. 2010 May 12;110(5):2641–84.

258. McWade MA, Paras C, White LM, Phay JE, Mahadevan-Jansen A, and J. T. Broome. A novel optical approach to intraoperative detection of parathyroid glands,. Surgery. 154:1371–1377.

259. Brandao MP, Iwakura R, Honorato-Sobrinho AA, Haleplian K, Ito AS, de Freitas LCC, et al. Optical Characterization of Parathyroid Tissues. Appl Spectrosc. 2016 01;70(10):1709–16.

260. Sridharan S, Huang EC, Campbell MJ, Marcu L. Fluorescence Lifetime Imaging for Intra-Operative Guidance during Thyroid Surgery. In: Optics in the Life Sciences Congress. Optical Society of America; 2017. p. OmM3D.2.

261. McWade M, Pence IJ, Paras C, and A. Mahadevan-Jansen. Imaging system design for surgical guidance with near-infrared autofluorescence,. 931303–931303 p.

262. Pellionisz PA, Hu Y, Moon A, Rangwalla K, Pensa J, John MAS. Ratiometric autofluorescence lifetime imaging system standardization and application for head and neck cancer. In: Optics in Health Care and Biomedical Optics IX [Internet]. International Society for Optics and Photonics; 2019 [cited 2019 Dec 10]. p. 1119006. Available from: https://www.spiedigitallibrary.org/conference-proceedings-of-spie/11190/1119006/Ratiometric-autofluorescence-lifetime-imaging-system-standardization-and-application-for-head/10.1117/12.2537631.short

263. Pellionisz PA, Cheng H, Pantoja JL, Grundfest W, John MAS. Development of Relative Lifetime Imaging System for Intraoperative Parathyroid Identification. Opt Life Sci. 2019;2.

264. Hu Y, Moon AS, Pellionisz P, Huang S, Stafsudd O, John MS. Design and validation of an intraoperative autofluorescence lifetime imaging device. In: Imaging, Therapeutics, and Advanced Technology in Head and Neck Surgery and Otolaryngology 2020 [Internet]. International Society for Optics and Photonics; 2020 [cited 2020 Apr 29]. p. 1121309. Available from: https://www.spiedigitallibrary.org/conference-proceedings-of-spie/11213/1121309/Design-and-validation-of-an-intraoperative-autofluorescence-lifetime-imaging-device/10.1117/12.2560000.short

265. Fass L. Imaging and cancer: A review. Mol Oncol. 2008;2(2):115–152.

266. Parrish-Novak J, Holland EC, Olson JM. Image-Guided Tumor Resection. Cancer J Sudbury Mass. 2015;21(3):206–12.

267. Tringale KR, Pang J, Nguyen QT. Image-guided surgery in cancer: A strategy to reduce incidence of positive surgical margins. Wiley Interdiscip Rev Syst Biol Med. 2018;(November 2017):1–18.

268. Visgauss JD, Eward WC, Brigman BE. Innovations in Intraoperative Tumor Visualization. Orthop Clin North Am. 2016;47(1):253–64.

269. Papour A, Taylor Z, Sherman A, Sanchez D, Lucey G, Liau L, et al. Optical imaging for brain tissue characterization using relative fluorescence lifetime imaging. J Biomed Opt. 2013;18(6):60504.

270. Pavlova I, Sokolov K, Drezek R, Malpica A, Follen M, Richards-Kortum R. Microanatomical and biochemical origins of normal and precancerous cervical autofluorescence using laser-scanning fluorescence confocal microscopy. Photochem Photobiol. 2003;77(5):550–555.

271. Pavlova I, Williams M, El-Naggar A, Richards-Kortum R, Gillenwater A. Understanding the biological basis of autofluorescence imaging for oral cancer detection: high-resolution fluorescence microscopy in viable tissue. Clin Cancer Res. 2008;14(8):2396–2404.

272. Schantz SP, Kolli V, Savage HE, Yu G, Shah JP, Harris DE, et al. In vivo native cellular fluorescence and histological characteristics of head and neck cancer. Clin Cancer Res. 1998;4(5):1177–1182.

273. Skala MC, Riching KM, Gendron-Fitzpatrick A, Eickhoff J, Eliceiri KW, White JG, et al. In vivo multiphoton microscopy of NADH and FAD redox states, fluorescence lifetimes, and cellular morphology in precancerous epithelia. Proc Natl Acad Sci. 2007 Dec 4;104(49):19494–9.

274. Sherman AJ, Papour A, Bhargava S, St. John MAR, Yong WH, Taylor Z, et al. Normalized fluorescence lifetime imaging for tumor identification and margin delineation. Biomed Clin Diagn San Franc SPIE SIEGEL R WARD E BRAWLEY O JEMAL Cancer Stat CA J Clin. 2013;61 SRC-:85721H.

275. Kim IA, Taylor ZD, Cheng H, Sebastian C, Maccabi A, Garritano J, et al. Dynamic Optical Contrast Imaging: A Technique to Differentiate Parathyroid Tissue from Surrounding Tissues. Otolaryngol-Head Neck Surg. 2017;156(3):480–3.

276. John MS, SADDIK G, Taylor Z, Grundfest W. Imaging method and system for intraoperative surgical margin assessment [Internet]. WO2019089998A1, 2019 [cited 2020 May 2]. Available from: https://patents.google.com/patent/WO2019089998A1/en?inventor=maie+St.+John&oq=maie+St.+John

277. Grundfest WS, Stafsudd OM, Jiang P-C, Papour A, Taylor ZD. System and method for time-resolved fluorescence imaging and pulse shaping [Internet]. US20150053871A1, 2015 [cited 2020 May 2]. Available from: https://patents.google.com/patent/US20150053871/en?oq=grundfest+warren

278. Grundfest WS, Stafsudd OM, JIANG P-C, PAPOUR A, TAYLOR ZD. System and method for time-resolved fluorescence imaging and pulse shaping [Internet]. CA2865948A1, 2013 [cited 2020 May 2]. Available from: https://patents.google.com/patent/CA2865948A1/en?oq=grundfest+warren

279. Jo JA, Marcu L, Fang Q, Papaioannou T. Method for fluorescence lifetime imaging microscopy and spectroscopy [Internet]. EP1659944A2, 2006 [cited 2020 May 2]. Available from: https://patents.google.com/patent/EP1659944A2/en?oq=grundfest+warren

280. Garcia-Allende PB, Ntziachristos V. Optical Image-Guidance to Bridge the Gap Between Preoperative Planning and Postoperative Control. In: Fong Y, Giulianotti PC, Lewis J, Groot Koerkamp B, Reiner T, editors. Imaging and Visualization in The Modern Operating Room [Internet]. New York, NY: Springer New York; 2015 [cited 2019 Dec 10]. p. 17–27. Available from: http://link.springer.com/10.1007/978-1-4939-2326-7_2

281. Tringale KR, Pang J, Nguyen QT. Image-guided surgery in cancer: A strategy to reduce incidence of positive surgical margins. Wiley Interdiscip Rev Syst Biol Med. 2018;10(3):e1412.

282. Wilke LG, Brown JQ, Bydlon TM, Kennedy SA, Richards LM, Junker MK, et al. Rapid noninvasive optical imaging of tissue composition in breast tumor margins. Am J Surg. 2009 Oct;198(4):566–74.

283. Yao R, Ochoa M, Yan P, Intes X. Net-FLICS: fast quantitative wide-field fluorescence lifetime imaging with compressed sensing – a deep learning approach. Light Sci Appl. 2019 Mar 6;8(1):26.

284. van der Vorst JR, Schaafsma BE, Verbeek FPR, Keereweer S, Jansen JC, van der Velden L-A, et al. Near-infrared fluorescence sentinel lymph node mapping of the oral cavity in head and neck cancer patients. Oral Oncol. 2013 Jan;49(1):15–9.

285. Nishio N, van den Berg NS, van Keulen S, Martin BA, Fakurnejad S, Zhou Q, et al. Optimal Dosing Strategy for Fluorescence-Guided Surgery with Panitumumab-IRDye800CW in Head and Neck Cancer. Mol Imaging Biol. 2019 May 3;

286. Sexton K, Davis SC, McClatchy D, Valdes PA, Kanick SC, Paulsen KD, et al. Pulsed-light imaging for fluorescence guided surgery under normal room lighting. Opt Lett. 2013 Sep 1;38(17):3249–52.

287. Zhu B, Rasmussen JC, Sevick-Muraca EM. Non-invasive fluorescence imaging under ambient light conditions using a modulated ICCD and laser diode. Biomed Opt Express. 2014 Jan 24;5(2):562–72.

288. Kasap SO. Optoelectronics and photonics: principles and practices. 2nd ed. Boston: Pearson; 2013. 528 p.

289. Hamzavi IH, Lyons AB, Kohli I, Narla S, Parks-Miller A, Gelfand JM, et al. Ultraviolet germicidal irradiation: possible method for respirator disinfection to facilitate reuse during COVID-19 pandemic. J Am Acad Dermatol. 2020 Apr 1;

290. Laikin M. Lens design. Fourth edition. Boca Raton,Fla: CRC Press; 2007. 478 p. (Optical science and engineering).

291. Federman DD. The biology of human sex differences. N Engl J Med. 2006;354(14):1507–14.

292. D'Souza G, Wentz A, Kluz N, Zhang Y, Sugar E, Youngfellow RM, et al. Sex Differences in Risk Factors and Natural History of Oral Human Papillomavirus Infection. J Infect Dis. 2016;213(12):1893–6.

293. Petti S. Lifestyle risk factors for oral cancer. Oral Oncol. 2009;45(4–5):340–50.

294. Muscat JE, Richie JP, Thompson S, Wynder EL. Gender differences in smoking and risk for oral cancer. Cancer Res. 1996;56(22):5192–7.

295. Llewellyn CD, Johnson NW, Warnakulasuriya KAAS. Risk factors for oral cancer in newly diagnosed patients aged 45 years and younger: a case-control study in Southern England. J Oral Pathol Med Off Publ Int Assoc Oral Pathol Am Acad Oral Pathol. 2004;33(9):525–32.

296. Toporcov TN, Znaor A, Zhang Z-F, Yu G-P, Winn DM, Wei Q, et al. Risk factors for head and neck cancer in young adults: a pooled analysis in the INHANCE consortium. Int J Epidemiol. 2015;44(1):169–85.

297. Patel SC, Carpenter WR, Tyree S, Couch ME, Weissler M, Hackman T, et al. Increasing incidence of oral tongue squamous cell carcinoma in young white women, age 18 to 44 years. J Clin Oncol. 2011;29(11):1488–94.

298. Honorato J, Rebelo MS, Dias FL, Camisasca DR, Faria PA, E Silva GA, et al. Gender differences in prognostic factors for oral cancer. Int J Oral Maxillofac Surg. 2015;44(10):1205–11.

299. D'Souza G, Westra WH, Wang SJ, Van Zante A, Wentz A, Kluz N, et al. Differences in the prevalence of human papillomavirus (HPV) in head and neck squamous cell cancers by sex, race, anatomic tumor site, and HPV detection method. JAMA Oncol. 2017;3(2):169–77.

300. Suba Z. Gender-related hormonal risk factors for oral cancer. Pathol Oncol Res. 2007;13(3):195–202.

301. Gupta N, Gupta R, Acharya AK, Patthi B, Goud V, Reddy S, et al. Changing Trends in oral cancer - a global scenario. Nepal J Epidemiol. 2016;6(4):613–9.

302. Fakhry C, Westra WH, Wang SJ, van Zante A, Zhang Y, Rettig E, et al. The prognostic role of sex, race, and human papillomavirus in oropharyngeal and nonoropharyngeal head and neck squamous cell cancer. Cancer. 2017 May 1;123(9):1566–75.

303. Khot K, Deshmane S, Bagri-Manjarekar K, Warke D, Kotak K. A cytomorphometric analysis of oral mucosal changes in tobacco users. J Nat Sci Biol Med. 2015;6(3):22.

304. Syamala B, Chitturi R, Chandrasekhar P, Prakash Chandra Kl, Kumar Kk, Ramana Reddy B. Cytomorphometric analysis of exfoliated buccal cells to evaluate the malignant changes in individuals with tobacco smoking and chewing habits. J Dr NTR Univ Health Sci. 2017;6(3):143.

305. Sharma D, Sandhu S V, Bansal H, Gupta S. Distinct perturbations of oral squamous cell carcinoma patients: A quantitative cytomorphometric analysis. Int J Health Sci. 2015;9(3):283–91.

306. Lu C, Lewis JS, Dupont WD, Plummer WD, Janowczyk A, Madabhushi A. An oral cavity squamous cell carcinoma quantitative histomorphometric-based image classifier of nuclear morphology can risk stratify patients for disease-specific survival. Mod Pathol. 2017;30(12):1655–65.

307. Gupta B, Johnson NW, Kumar N. Global Epidemiology of Head and Neck Cancers: A Continuing Challenge. Oncology. 2016;91(1):13–23.

308. Babey M, Wang Y, Kubota T, Fong C, Menendez A, Elalieh HZ, et al. Gender-specific differences in the skeletal response to continuous PTH in mice lacking the IGF1 receptor in mature osteoblasts. J Bone Miner Res. 2015;30(6):1064–76.

309. Basile C, Lomonte C, Vernaglione L, Casucci F, Chimienti D, Bruno A, et al. A high body mass index and female gender are associated with an increased risk of nodular hyperplasia of parathyroid glands in chronic uraemia. Nephrol Dial Transplant. 2006;21(4):968–74.

310. Hashim D, Sartori S, Vecchia C La, Serraino D, Maso LD, Negri E, et al. Hormone factors play a favorable role in female head and neck cancer risk. Cancer Med. 2017;

311. Mazeh H, Sippel RS, Chen H. The role of gender in primary hyperparathyroidism: Same disease, different presentation. Ann Surg Oncol. 2012;19(9):2958–62.

312. Fraser WD. Hyperparathyroidism. The Lancet. 2009;374(9684):145–58.

313. Miller BS, Dimick J, Wainess R, Burney RE. Age- and sex-related incidence of surgically treated primary hyperparathyroidism. World J Surg. 2008;32(5):795–9.

314. Yeh MW, Ituarte PHG, Zhou HC, Nishimoto S, Amy Liu I-L, Harari A, et al. Incidence and Prevalence of Primary Hyperparathyroidism in a Racially Mixed Population. J Clin Endocrinol Metab. 2013;98(3):1122–9.

315. Kokrdova Z. Pregnancy and primary hyperparathyroidism. J Obstet Gynaecol. 2010;30(1):57–9.

316. Charles JP, Fuchs J, Hefter M, Vischedyk JB, Kleint M, Vogiatzi F, et al. Monitoring the dynamics of clonal tumour evolution in vivo using secreted luciferases. Nat Commun. 2014;5.

317. McGranahan N, Swanton C. Biological and therapeutic impact of intratumor heterogeneity in cancer evolution. Cancer Cell. 2015;27(1):15–26.

318. Meacham CE, Morrison SJ. Tumour heterogeneity and cancer cell plasticity. Nature. 2013;501(7467):328–37.

319. Koh J, Hogue JA, Wang Y, Disalvo M, Allbritton NL, Shi Y, et al. Single-cell functional analysis of parathyroid adenomas reveals distinct classes of calcium sensing behaviour in primary hyperparathyroidism. J Cell Mol Med. 2016;20(2):351–9.

320. Yock PG, editor. Biodesign: the process of innovating medical technologies. Second edition. Cambridge ; New York: Cambridge University Press; 2015. 839 p.

321. Schwartz J, Macomber C. So, You Think You Have an Idea: A Practical Risk Reduction-Conceptual Model for Academic Translational Research. Bioeng Basel. 2017 Apr;4(2).

322. Herr GL. Biodesign: the process of innovating medical technologies. Biomed Instrum Technol. 2010 Sep;44(5):388.

323. Brynjolfsson E, McAfee A. Winning the race with ever-smarter machines. MIT Sloan Manag Rev. 2012;53(2):53.

324. Doi K. Diagnostic imaging over the last 50 years: research and development in medical imaging science and technology. Phys Med Biol. 2006 Jul;51(13):R5–27.

325. Ackerly DC, Valverde AM, Diener LW, Dossary KL, Schulman KA. Fueling innovation in medical devices (and beyond): venture capital in health care. Health Aff. 2009 Jan;28(1):w68–75.

326. Kleinbeck K, Anderson E, Ogle M, Burmania J, Kao WJ. The new (challenging) role of academia in biomaterial translational research and medical device development. Biointerphases. 2012 Dec;7(1–4):12.